THE EFFECTS OF ANATOMIC RESOLUTION, RESPIRATORY VARIATIONS AND DOSE CALCULATION METHODS ON LUNG DOSIMETRY

A Thesis Submitted to the
College of Graduate Studies and Research
in Partial Fulfillment of the Requirements
for the degree of Doctor of Philosophy
in the Department of Physics and Engineering Physics
University of Saskatchewan
Saskatoon

By
Kerry Kent Ronald Babcock

PERMISSION TO USE

In presenting this thesis in partial fulfillment of the requirements for a Postgraduate degree from the University of Saskatchewan, I agree that the Libraries of this University may make it freely available for inspection. I further agree that permission for copying of this thesis in any manner, in whole or in part, for scholarly purposes may be granted by the professor or professors who supervised my thesis work or, in their absence, by the Head of the Department or the Dean of the College in which my thesis work was done. It is understood that any copying or publication or use of this thesis or parts thereof for financial gain shall not be allowed without my written permission. It is also understood that due recognition shall be given to me and to the University of Saskatchewan in any scholarly use which may be made of any material in my thesis.

DISCLAIMER

Reference in this thesis/dissertation to any specific commercial products, process, or service by trade name, trademark, manufacturer, or otherwise, does not constitute or imply its endorsement, recommendation, or favoring by the University of Saskatchewan. The views and opinions of the author expressed herein do not state or reflect those of the University of Saskatchewan, and shall not be used for advertising or product endorsement purposes.

Requests for permission to copy or to make other use of material in this thesis in whole or part should be addressed to:

Head of the Department of Physics and Engineering Physics
University of Saskatchewan
Saskatoon, Saskatchewan S7N 5A9

ABSTRACT

The goal of this thesis was to explore the effects of dose resolution, respiratory variation and dose calculation method on dose accuracy. To achieve this, two models of lung were created. The first model, called TISSUE, approximated the connective alveolar tissues of the lung. The second model, called BRANCH, approximated the lungs bronchial, arterial and venous branching networks. Both models were varied to represent the full inhalation, full exhalation and midbreath phases of the respiration cycle.

To explore the effects of dose resolution and respiratory variation on dose accuracy, each model was converted into a CT dataset and imported into a Monte Carlo simulation. The resulting dose distributions were compared and contrasted against dose distributions from Monte Carlo simulations which included the explicit model geometries. It was concluded that, regardless of respiratory phase, the exclusion of the connective tissue structures in the CT representation did not significantly effect the accuracy of dose calculations. However, the exclusion of the BRANCH structures resulted in dose underestimations as high as 14% local to the branching structures. As lung density decreased, the overall dose accuracy marginally decreased.

To explore the effects of dose calculation method on dose accuracy, CT representations of the lung models were imported into the Pinnacle^3 treatment planning system. Dose distributions were calculated using the collapsed cone convolution method and compared to those derived using the Monte Carlo method. For both lung models, it was concluded that the accuracy of the collapsed cone algorithm decreased with decreasing density. At full inhalation lung density, the collapsed cone algorithm underestimated dose by as much as 15%. Also, the accuracy of the CCC method decreased with decreasing field size. Further work is needed to determine the source of the discrepancy.

ACKNOWLEDGEMENTS

I would like to acknowledge my supervisor Dr. Narinder Sidhu for all his guidance and patience during my time at the Saskatoon Cancer Centre. I would also like to acknowledge Gavin Cranmer-Sargison for helping me proof read my thesis and for being an excellent sounding board for my ideas. I'd like to acknowledge the staff at the Saskatoon Cancer Centre for all the help they provided me. I'd like to thank the Saskatchewan Cancer Agency for generously supplying funding for this project. I'd like to thank the Department of Physics and Engineering at the University of Saskatchewan for giving me the opportunity to persue this degree. I'd like to acknowledge my parents for giving me support during tough times. Lastly, I'd like to acknowledge my wife Patti who gives me the strength to persevere.

CONTENTS

LIST OF TABLES

LIST OF FIGURES

List of Abbreviations

AAPM	The American Association of Physicists in Medicine
ATS	American Thoracic Society
3D-CRT	Three Dimensional Conformal Radiation Therapy
CCC	Collapsed Cone Convolution
CH	Condensed History
CP	Crossplane
CPE	Charged Particle Equilibrium
CT	Computed Tomography
CDSA	Continuous Slowing Down Approximation
DSAR	Differential Scatter Air Ratio
DTI	Distance To Intercept
DTNI	Distance To Next Interaction
DVOL	Delta Volume
ECF	Electron Contamination Factor
EGSnrc	Electron Gamma Shower Monte Carlo developed at the National Research Council of Canada
ERS	European Respirology Society
ERV	Expiratory Reserve Volume
ETAR	Equivalent Tissue Air Ratio
FIBH	Full Inhalation Breath Hold
FRC	Functional Residual Capacity
HU	Hounsfield Unit
IC	Inspiratory Capacity
ICRU	International Commission on Radiation Units and Measurements
IP	Inplane
IRV	Inspiratory Reserve Volume
KERMA	Kinetic Energy Released per unit MAss
MC	Monte Carlo
MC-CT	Monte Carlo simulations using a CT representation of lung anatomy
MC-M	Monte Carlo simulations using an explicit representation of lung anatomy
MRI	Magnetic Resonance Imaging
RTAR	Ratio of Tissue Air Ratios
RV	Reserve Volume
S/C	Superposition/Convolution
SBS	Selective Bremsstrahlung Splitting
SSD	Source to Surface Distance

TCPE	Transient Charged Particle Equilibrium
TERMA	Total Energy Released per unit MAss
TLC	Total Lung Capacity
TPS	Treatment Planning System
TRM	Textbook of Respiratory Medicine
TRU	Terminal Respiratory Unit
TV	Tidal Volume
VC	Vital Capacity
VHP	Visible Human Project
VMC++	Voxel Monte Carlo written in C++

CHAPTER 1

INTRODUCTION

The management of patients with lung cancer often requires the use of radiation therapy as part of the treatment process. Beams of x-rays are projected into the malignant cells causing damage, which hinders their ability to replicate and subsist. Unfortunately, normal cells are also susceptible to this damage which can lead to acute complications during treatment. To avoid unwanted destruction of healthy tissues, it is desirable to minimise dose outside the target tumour volume. To achieve this, radiation beam(s) are shaped to the contour of the three dimensional tumour volume. This approach, referred to as three-dimensional conformal radiation therapy (3D-CRT) (Giraud et al., 2001; Armstrong, 1998; Wilson, 2003), is the standard clinical practice.

3D-CRT treatment is a multi-step process (see Fig.1.1) with the overall accuracy dependent on the correctness of each step. A typical treatment may be outlined as follows:

1. **Diagnosis and 3D Imaging**: When a patient is diagnosed with a malignancy, their physician will assess whether radiation therapy treatment is appropriate for their illness. If radiation therapy is prescribed, the patient is imaged with computed tomography (CT) technology. The CT scan is processed into a three dimensional mapping of x-ray attenuation within the body.

2. **Target Volume and Organ Localization**: An oncologist takes the image and isolates the region of interest (often a tumour) by manually defining a contour in the CT map. The same is done for any organ or region that is to be spared.

3. **Beam Selection**: Based on the type of malignancy, the parameters of the beam (energy, spectrum, radiation type, and number of beams) are selected.

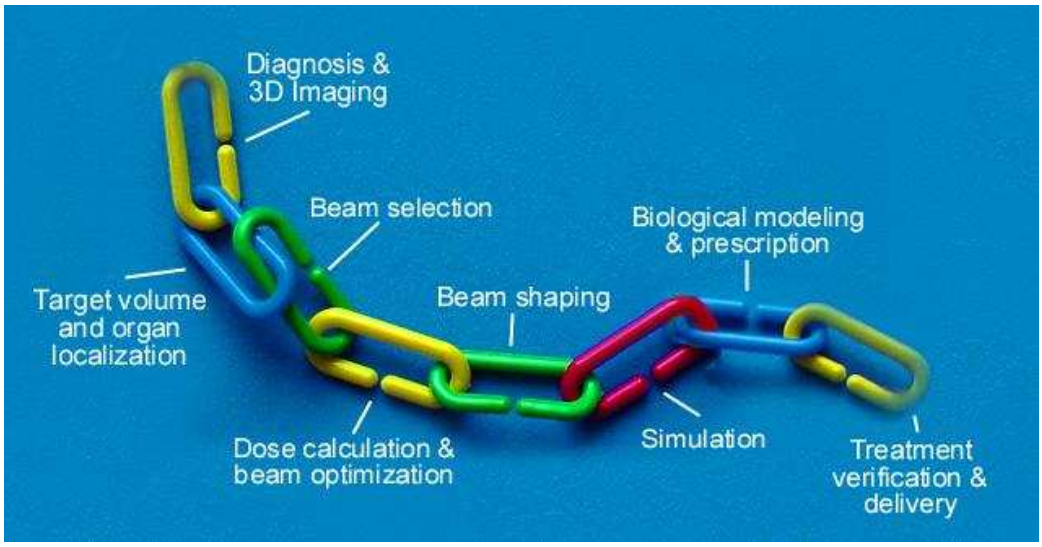

Figure 1.1: The chain of events that occurs during a typical radiation therapy treatment. The overall accuracy of the treatment is limited by the weakest link in the chain.

4. **Beam Shaping**: The physical beam is collimated.

5. **Dose Calculation & Optimization**: The beam characteristics, and CT data are entered into treatment planning software which predicts the resulting energy distribution within the CT data set. The beam orientation, and profile are modified to minimise dose to healthy tissues and sensitive structures while applying a prescribed dose to the treatment volume.

6. **Biological Modeling & Prescription**: A treatment schedule (number and frequency of treatments) for administering the dose is then formulated based on biological considerations.

7. **Treatment Verification and Delivery**: The treatment plan is verified by a medical physicist and administered to the patient.

The most difficult step to verify in the 3D-CRT process is dose calculation and optimization. This is partially due to the inability to verify the dose prediction with direct measurement in vivo. Ultimately, the validity of a dose prediction algorithm is predicated on

its ability to predict the energy spread of the incident radiation beam. It has been shown (Boyer & Schultheiss, 1988) that dose predictions errors as small as 5% can result in a 10-20% decrease in tumour control and a 20-30% increase in normal tissue complications. Also, a 7% increase in dose can result in a clinically observable increase in patient side effects (Dutreix, 1984). When you factor in the uncertainty of other steps in the treatment process, the overall uncertainty becomes even larger. Therefore, it is paramount to achieve dose predictions with the greatest accuracy possible to minimise its contribution to the overall uncertainty.

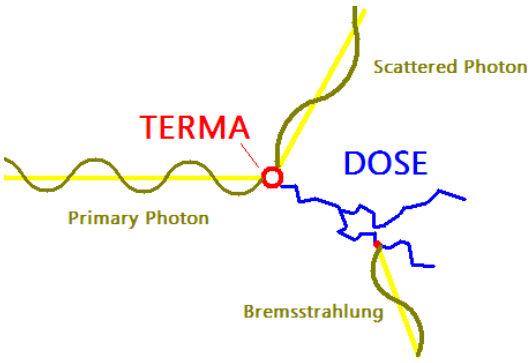

Figure 1.2: The energy deposition process: (1) The TERMA step. An incident photon imparts its energy to the medium via an interaction. The resulting energy is carried away by resulting electrons and photons. (2) The DOSE step. Electrons undergo large number of collisions depositing energy locally along their paths. Bremsstrahlung x-rays are also generated which carry energy away to other interaction sites.

The prediction of spatial dose requires an understanding of the energy deposition process. Energy deposition occurs in two steps (see Fig.1.2):

1. **The TERMA Step** - In the TERMA (Total Energy Released per unit MAss) step, the incident photon energy is given to the medium via the photoelectric, Compton and pair production interactions. The combined effect of these three interactions is characterized by a mass attenuation coefficient ($\frac{\mu}{\rho}$) which represents the probability of a photon being attenuated per unit mass thickness. When this coefficient is multiplied by the photon energy fluence (the amount of energy crossing a unit area) (Ψ)

at a given point one is left with the TERMA.

$$TERMA = \frac{\mu}{\rho} \cdot \Psi \tag{1.1}$$

A subset of the TERMA is the KERMA which represents the kinetic energy transferred to charged particles. In a similar manner to the TERMA, the KERMA can be related to the energy fluence by the mass energy transfer ($\frac{\mu_{tr}}{\rho}$) coefficient.

2. **The DOSE Step** - Once energy is transferred to the medium, the liberated charged particles continue to travel and interact within the medium. This is called the DOSE step. Through multiple Coulomb interactions, the charged particles give energy back to the medium. Most of this energy is deposited locally, with a small fraction being carried away by x-ray photons created in bremsstrahlung events. The amount of energy deposited along the particle path is dictated by the mass collisional stopping power ($\frac{S_{col}}{\rho}$) which represents the energy loss per unit pathlength (in g/cm^2).

In the DOSE step, a charged particle may undergo as many as one million discrete interaction events before coming to rest in the medium. However, the distance between coinciding interactions is so small that the particle can be treated as if it continually loses energy along its entire pathlength. This assumption is called the continuous slowing down approximation (CSDA). From this, the electrons range can then be calculated from its incident energy and the collisional stopping power:

$$R_{CSDA} = \int_0^E \left(\frac{S_{col}}{\rho}\right)^{-1} \cdot dE \tag{1.2}$$

When the electron range is small relative to that of the scoring volume one can relate the DOSE and TERMA steps by assuming that any energy released in the TERMA step stays local to the interaction site. This is the case for a ^{60}Co beam (1.25 MeV) incident on a simple medium, such as water. To relate DOSE and TERMA for higher energies, one must rely on a phenomenon called charged particle equilibrium.

Charged particle equilibrium (CPE) refers to a state where the number of secondary electrons entering a volume element is balanced by the same number of electrons leaving. When CPE conditions occur, the final dose at a point is equal to the collision KERMA

at that point. In reality, charged particle equilibrium is never fully achieved due to beam attenuation and divergence. However, if the spread of the beam is large enough to create a near equilibrium state in directions perpendicular to the axis of the beam, the attenuation simply causes an exponential shift in the dose at depth as a function of KERMA. Thus, the dose along the axis of the beam at depth x can be represented as:

$$Dose(x) = e^{-\frac{\mu}{\rho}\bar{x}} \cdot KERMA(x) \tag{1.3}$$

where $\bar{x}$ is the mean distance that secondary charged particles carry their kinetic energy in the direction of the primary beam. This condition is known as transient charged particle equilibrium (TCPE).

The preceeding treatment assumes that transport occurs in a single medium of uniform density. If the medium contains variations in density, as is the case for tissues in the body, one can still relate DOSE and TERMA by applying two theorems:

1. **Fano's Theorem** - If an infinite medium of varying density and like atomic composition is irradiated by a uniform photon fluence, the resulting electron fluence will also be uniform and independent of density. This theorem holds provided that primary photon attenuation, the stopping power density effect and the release of secondary photons is neglected.

2. **O'Conner's Theorem** - If two separate media have the same atomic composition but different mass densities, the ratio of scattered to primary fluence will be the same for both provided that all physical dimensions are scaled by the inverse of the mass density. This allows one to take dose distributions within one density and scale them to predict the dose distributions in another density.

These theorems rely heavily on the assumption of minimal photon attenuation and that the media contains a uniform atomic composition. Typical radiation therapy treatments do not meet these criteria and require additional corrections for predicting dose deposition. One of the best examples is lung tissue.

It is well documented (Cranmer-Sargison, Beckham, & Popescu, 2004; Ekstrand & Barnes, 1990; Mackie et al., 1985; Hunt, Desobry, Fowble, & Coia, 1997; El-Khatib &

Battista, 1986; Saithoh, Fujisaki, Saskai, & Kunieda, 2002) that the low density heterogeneous structure of the lung provides a challenge in calculating spatial dose deposition. In the lung, TCPE conditions are never realized due to an increased range of secondary electrons in the low-density environment. This results in a spread of deposited energy away from the initial photon interactions of the TERMA step. If the beam energy is high, or the field size small (which is common for treatments of localized tumours), electrons can escape outside the treatment field. This increased spread of energy tends to be improperly predicted by dose algorithms that do not directly account for electron transport (Mackie et al., 1985; Arnfield, Siantar, Siebers, & Garmon, 2000; Mayer et al., 1997). Particularly, dose is miscalculated along the central beam axis (Mackie et al., 1985), beam profiles are wider, and have a modified penumbra and lose their flatness (Ekstrand & Barnes, 1990). The lung volume also contains several different media (cartilage, air, tissues, etc...) which do not share a common atomic composition. As a result, one should not apply the Fano or O'Conner theorems to predict spatial dose. One must make explicit corrections for the secondary electron energy spread.

A variety of methods have been devised to correct spatial dose deposition in regions of heterogeneity/low density. Each method can be classified in one of two categories:

1. **No Electron Transport**: Methods in this category attempt to correct for heterogeneities by applying a multiplicative factor to dose at a point in water to give the dose in the heterogeneity. These methods, which are presented here as a historical overview, require several assumptions that make them inadequate for predictions in the lung. The first assumption is that a state of TCPE is achieved. The second assumption is that the beam width is small relative to the boundaries of the heterogeneity (i.e. approximate heterogeneities as semi-infinite slabs). The last, and most important assumption is that all energy deposited by the beam is deposited local to the interaction site. Most methods in this category do not account for the scatter component of the beam (Linear attenuation, ratio of tissue ratios (RTAR), Batho Power Law), while some include additional corrections to estimate the scattered photon dose from other points in the geometry (equivalent tissue air ratio (ETAR), differential scatter air ratio (DSAR), delta volume (DVOL), 3D Subtraction Method). By

accounting for photon scatter, the later methods lessen the restriction that the media be approximated as semi-infinite.

2. **Explicit Electron Transport**: Methods of this type remove the assumption that all photon energy is deposited at the interaction site. The energy carried away from an interaction site, be it photon or electron energy, is accounted for in the dose calculation. There are two distinct approaches that fall into this category: (a) Superposition/Convolution (S/C) and (b) Monte Carlo methods.

   (a) **Superposition/Convolution**

   In the S/C method, the TERMA at each point in the phantom is modified by a kernel, or spread function via a convolution integral.

   $$D(\vec{r}) = \int TERMA(\vec{r}') \cdot K(\vec{r},\vec{r}')d^3\vec{r}' \tag{1.4}$$

   In this integral, the vector $\vec{r}$ represents the point of interest where the dose is to be calculated. The vector $\vec{r}'$ represents all other points external to the point of interest. The kernel ($K(\vec{r},\vec{r}')$) acts as a spread function on the point energy TERMA. The kernel spreads out the TERMA energy from $\vec{r}'$ to give its contribution of scattered photon and electron energy at $\vec{r}$. When the integral is performed, the contribution of dose to a point from all other points in the phantom is calculated. The accuracy of the S/C method hinges on the derivation of the kernel. The kernel must be derived external to the calculation, usually requiring Monte Carlo modeling. Often, a kernel is created for each competing type of interaction and the convolution integral for each kernel superimposed on one another, hence the name superposition/convolution.

   The most clinically used algorithms in predicting spatial dose within the lung are the S/C methods. Algorithms of this type consider electron transport on a macroscopic level only (electrons travel in straight lines) (Arnfield et al., 2000) and require empirical measurements or Monte Carlo data of electron energy spread that may not apply to all treatment conditions. The universal application of convolution/superposition methods under heterogeneous conditions

requires further investigation as dose discrepancies are reported (Cranmer-Sargison et al., 2004). It is difficult to verify S/C methods as it is not possible to make in vivo measurements during a treatment. It is important to verify the use of S/C techniques under conditions that closely mimic an actual treatment to ensure that the desired accuracy is being achieved.

(b) **Monte Carlo**

Monte Carlo methods are unique in that they do not correct dose within a heterogeneity but simulate energy deposition directly. This is achieved by sampling experimental/theoretical probability distributions of the various physical processes. Through the use of a random number generator, particle histories are generated on an event by event basis. The sum of many interactions converge to model the energy spread. Monte Carlo methods have repeatedly been shown to perform well in heterogeneous media where there are multiple interfaces. Historically, Monte Carlo techniques have not been used for clinical radiation therapy treatment planning due to long computational times. However with the advent of fast Monte Carlo codes such as VMC++ (Kawrakow & Fippel, 2000) and innovations such as the application of neural networks to Monte Carlo calculations (Mathieu et al., 2005), clinical Monte Carlo planning is being developed.

The lung is a porous, structured, low density medium containing a large number of air/tissue, air/cartilage and tissue/cartilage interfaces. Due to its complex structure, the lung is characterized by a spatial variation in mass and electron density which ultimately dictates energy distribution. During a typical radiation therapy treatment of the lung, a CT scan is used to capture a three dimensional map of x-ray attenuation. Although much of the lung anatomy is captured in the CT imaging process, there is a limit to the amount of detail that can be resolved or used. Most modern CT scanners are capable of capturing anatomic detail well below a resolution of 1 mm. However due to limitations in physical memory and a typically large image field of view, the practical resolution of a dose/CT voxel is reduced to 1 mm x 1 mm x 1 mm. Although this resolution may seem high, much

of the lungs structures, such as the smallest bronchial, arterial and venous branches as well as alveolar tissues remain unresolved.

A CT dataset contains a three dimensional array of voxels or volume elements. Each voxel is assigned a Hounsfield unit which is proportional to the x-ray attenuation of the voxel. For voxels containing structures below the CT/dose grid resolution, an average x-ray attenuation is assigned. In clinical practice, it is assumed that this assignment does not significantly effect the macroscopic dose distribution. Although this may be a fair approximation when the electron range is small, it is less certain for the larger electron ranges seen in the lungs constituent materials (mainly air). An averaging of x-ray attenuation may lead to inaccuracies in electron step size which in turn may lead to deviations in macroscopic dose. This difference could compromise the predictive ability of a treatment plan. In addition, when an averaged x-ray attenuation is assigned to a voxel, it is assumed that the attenuation of x-rays by that voxel is the same along all particle paths. As a simple example where this is not true, consider a single voxel of unit dimension (1 unit x 1 unit x 1 unit). Divide that voxel and assign one half the composition and density of water. For simplicity, make the other half vacuum. If a beam is placed incident on the voxel along an axis perpendicular to the dividing plane, the attenuation will be:

$$\frac{N}{N_0} = e^{-\frac{\mu_w}{\rho}/2} \tag{1.5}$$

where N/N_0 is the fraction of the incident beam which is attenuated, μ_w/ρ is the attenuation probability of water. The voxel is "seen" by the particle as a slab with a cross sectional area of one and a thickness of one half. If the beam is rotated 90° so that the beam is parallel to the dividing plane, the attenuation takes on a different value:

$$\frac{N}{N_0} = \frac{1}{2} e^{-\frac{\mu_w}{\rho}}. \tag{1.6}$$

Here the voxel is "seen" by the particle as having a cross sectional area of one half and a thickness of one. The preceeding arguments lead to the first objective of this thesis:

To determine whether the exclusion of lung anatomy below conventional CT imaging resolution results in deviations in calculated dose distributions

- Two anatomic lung models will be built: (1) a branching model that includes the bronchial, arterial and venous pathways of the lung and (2) a tissue model that emulates the alveolar connective tissues that make up much of the lung volume. Each model will include structure below the typical CT/dose resolution. The models will be coded into a Monte Carlo dose calculation. A computed tomography representation of the models will be created with a single atomic composition and mass density assigned to each voxel. The dose deposition for both the explicitly structured models and computed tomography datasets will be calculated in Monte Carlo. Dose distributions between the two representations will be compared and contrasted. Any significant disagreement between the dose distributions will be quantified.

The lung is a dynamic organ that varies in density and volume over the respiration cycle. This change in density and volume is due to structural changes in the lung anatomy. As a consequence of these structural changes, the scale of the lung anatomy below the CT/dose resolution also varies relative to the voxel dimension. For CT representations of lung anatomy, it is not known whether the phase at which a patient is imaged will have an effect on the accuracy of the CT representation. A decreased accuracy in the CT representation will ultimately lead to a decreased accuracy in the dose deposition calculations. This leads to the second objective of this thesis:

To determine whether dose calculation accuracy in the lung is influenced by structural variation due to respiratory motion

- The anatomic models from the first thesis objective will be expanded to represent

three different phases of the respiration cycle: (1) full exhale, (2) midbreath and (3) full inhale. Monte Carlo simulations of the three anatomic models will be performed. A CT representation of each model will then be created. Monte Carlo simulations using the CT representation will be run. The dose distributions from simulations of the two representations will be compared and contrasted.

Although Monte Carlo is established as the most accurate method for calculating dose in the lung, it is seldom used in clinical practice. The S/C algorithms are commonly chosen due to their treatment of secondary energy spread. At the Saskatoon Cancer Center, the most commonly used S/C algorithm is the Pinnacle^3 Treatment Planning System (Philips Radiation Oncology Systems, Andover, MA, USA) implementation of the Collapsed Cone Convolution (CCC). It is important to verify the accuracy of the CCC algorithm under a wide variety of treatment conditions. This includes different phases of respiration. In the literature, the CCC algorithm tends to be benchmarked for lung densities greater than 0.26 g/cm^3 (Arnfield et al., 2000; Bedford et al., 2003; Francescon, Cavedon, Reccanello, & Cora, 2000; Butson, 2000; Chow, 2003). It is often overlooked that lung density varies from 0.1-0.3 g/cm^3 over the respiration cycle. This leads to the third objective of this thesis:

To determine whether the Pinnacle^3 Collapsed Cone Convolution algorithm for dose calculations in the lung at different phases of the respiration cycle is accurate compared to Monte Carlo.

- The Monte Carlo simulations of the first two objectives will be recalculated using the CCC method. The CCC dose calculations will be compared and contrasted against dose distributions from the CT model Monte Carlo simulations. Any discrepancies between Monte Carlo and CCC dose calculations will be explored.

This thesis is laid out as follows. In Chapter 2, the reader will be introduced to the two dose calculation methods used in this thesis: the EGSnrc Monte Carlo and the Pinnacle^3

Collapsed Cone Convolution. Chapter 3 will describe the creation of the clinical beam models that were used with each dose calculation method. In Chapter 4, a brief overview of both the anatomy/physiology of the lung is given. This is followed by Chapter 5 which describes the creation and implementation of the Monte Carlo lung model codes. This chapter also gives a general description of the experimental setup used to address the objectives of this thesis. Chapter 6 presents the results of the project. Chapter 7 includes a discussion of the results and suggestions for future work. Finally, Chapter 8 summarizes summarizes the conclusions of the project as well as addresses the potential for future work.

CHAPTER 2

THE CALCULATION OF DOSE

2.1 Introduction

The following chapter describes, in detail, the two methods used in this thesis for calculating the dose distributions within a three dimensional, heterogeneous volume: (1) The EGSnrc Monte Carlo method and (2) the Collapsed Cone convolution/superposition method.

2.2 The EGSnrc Monte Carlo

The EGSnrc (Electron-Gamma-Shower) Monte Carlo (Kawrakow, Mainegra-Hing, Rogers, Tessier, & Walters, 2009; Kawrakow, 2000a; Kawrakow & Rogers, 2000), developed at the National Research Council in Ottawa, is a dedicated simulation of the physical photon and electron(positron) processes that occur in matter over the energy range of a few keV to several GeV. Written in MORTRAN, a structured, macro based language [1], EGSnrc provides the user a tool to reproduce particle transport and energy deposition in situations where experimental measurement may be impractical or impossible. EGSnrc relies on random number generation to create unique particle histories on an event by event basis. Specifically, interaction cross sections are sampled to produce particle kinematics consistent with physical observation. Individual events are of little practical interest but the combined effect of many events will yield an energy distribution that mimics nature and can be reproduced within a defined uncertainty. Monte Carlo can be employed under a

[1] Macro - A single programming statement that, when called, expands to a predefined series of statements

wide variety of geometric and material environments. The drawback to Monte Carlo is the large computational time required to achieve reasonable statistical uncertainties. However, with computers becoming increasingly cost effective and computational speeds increasing, Monte Carlo is slowly becoming a viable alternative to the currently utilized model based approaches that are limited by assumptions specific to the setup.

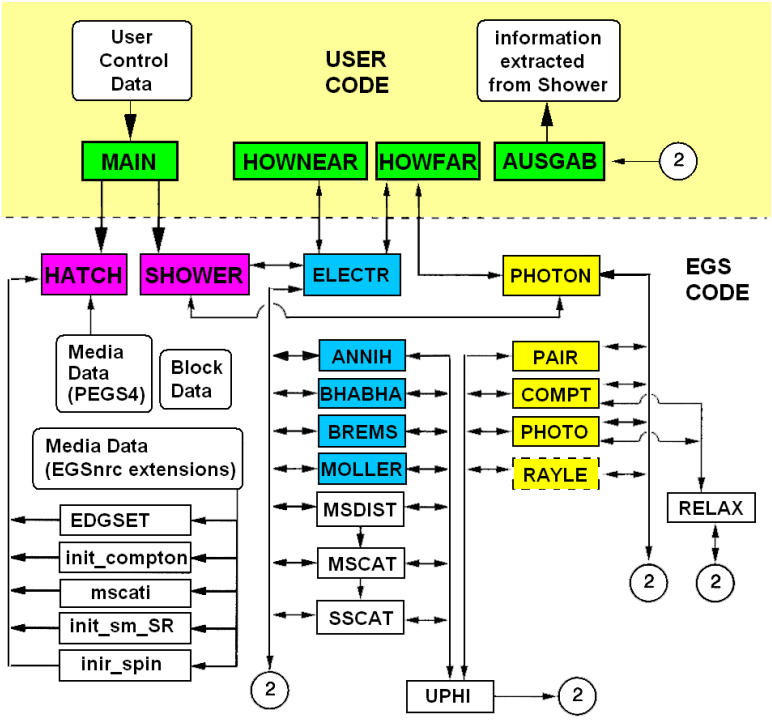

Figure 2.1: Flowchart of the EGSnrc Monte Carlo (taken from the EGSnrc Users Manual, Reference (B. R. B. Walters, Kawrakow, & Rogers, 2007)).

The EGS code is broken up into two parts as is seen in Fig.2.1: (1) The USER code, where user specific parameters (geometry, output variables) are set and (2) the EGS code, which handles the simulation of the physical processes that are independent of the user setup. Through the subroutines HATCH and SHOWER, these parts communicate with one another to make up a simulation. The programs, subroutines, and input files accessible to the user are defined as follows:

User Defined Code

- MAIN – initializes the various parameters of the simulation and interfaces with the EGSnrc code through the HATCH and SHOWER subroutines. This is where the user can define custom macros, common blocks and variables.

- HOWFAR – is where the geometry of the simulation is defined. HOWFAR calculates the distance-to-intercept (DTI) of a particle to a geometric surface along a given trajectory. If the DTI is closer than the distance to the next particle interaction site (DTNI) or the distance to the end of an electron step, HOWFAR returns the distance to the boundary and updates the region index to that of the adjacent medium.

- HOWNEAR – aids in electron transport and boundary crossing. This routine calculates a particle's distance to the nearest boundary.

- AUSGAB – is where the desired simulation output is formulated and stored.

User input file

- EGSINP file – defines the specifics of the simulation, i.e. particle transport settings, variance reduction techniques, number of histories and source parameters.

EGS/User Interface

- HATCH – reads in and sets up the necessary material data for the simulation. HATCH relies on pre-generated data from a separate program called PEGS4 (Preprocessor for EGS4). PEGS4 generates energy dependent photon attenuation coefficients and electron stopping powers based on experimental data and theoretical cross section calculations. By specifying elemental composition, density and energy range, data tables are generated for use in the EGS simulation.

- SHOWER – passes individual particle kinematic information into the EGS code and initiates the simulation.

The following sections give a general description of the physical processes modelled in the EGSnrc code. For a more complete description, please refer to the EGSnrc manual(Kawrakow, Mainegra-Hing, Rogers, Tessier, & Walters, 2009).

2.2.1 Photon transport and interactions

There are four photon processes simulated in the EGSnrc code: (1) the photoelectric effect, (2) Compton (coherent) scattering, (3) Rayleigh (incoherent) scattering, and (4) pair production. For a given material, the probability of these interactions occurring is related to their individual interaction cross sections designated $\Sigma_{\text{Photoelec}}$, Σ_{Compton}, Σ_{Rayleigh}, and Σ_{Pair} with the total probability of a photon interaction being their sum:

$$\Sigma_{\text{tot}} = \Sigma_{\text{Photoelec}} + \Sigma_{\text{Compton}} + \Sigma_{\text{Rayleigh}} + \Sigma_{\text{Pair}} \tag{2.1}$$

Using this information, EGSnrc transports a photon in the following manner. First, the distance from the current particle position to an interaction site is sampled from the relation:

$$s = \frac{-lnr_1}{\Sigma_{\text{tot}}} \tag{2.2}$$

where s is the path length and r_1 is a random number between 0 and 1. If the particle trajectory reaches a geometric boundary before the event (determined by HOWFAR), it is simply transported out of the current region and the process is repeated. Otherwise, the particle is transported to the point of interaction. Once at the site, the type of interaction is selected based on a second random number, r_2, and the following rules:

- Rayleigh Event if $r_2 < \Sigma_{\text{Rayleigh}}/\Sigma_{tot}$ (only if Rayleigh interactions are requested)
- Pair Production Event if $r_2 < \Sigma_{\text{Pair}}/\Sigma_{tot}$ and $E_\gamma > 2m_e$
- Compton Event if $r_2 < (\Sigma_{\text{Pair}} + \Sigma_{\text{Compton}})/\Sigma_{\text{tot}}$
- Photoelectric Event otherwise

Rayleigh is separated in this process as it is an optional interaction under EGSnrc. From here, differential cross section distributions are used to assign consistent kinematical information to all particles that result from the interaction. New particles are then transported

in the same manner until they either lose all their energy or leave the relevant geometry. A single particle history is finished when the transport of the first particle and all its secondaries is complete.

2.2.2 Atomic relaxations

An atomic relaxation is the transition of an atom from a higher to lower energy state. The relaxation process is mediated through the emission of either photons or electrons. The EGSnrc code is set up to explicitly handle transitions from shells with energies above 1 keV (mainly K and L shell transitions) while applying a more general method of averages for M shell transitions. Multiple relaxations are also explicitly sampled in the EGS code. Transitions are mediated by the emission of characteristic X-rays, or Auger/Coster-Kronig electrons.

2.2.3 Electron and positron interactions

2.2.3.1 Electron transport

Unlike photons, which deposit their energy at discrete points along their path, electrons lose their energy in a near continuous set of interactions. In fact, an electron may undergo upwards of a million interactions before coming to rest in the medium. It is not practical to simulate these interactions in Monte Carlo due to the large computational times required. To overcome this constraint, EGSnrc uses the class II condensed history (CH) technique formulated by Berger (Berger, 1963). In the CH scheme, electron interactions that release energy above a certain threshold receive explicit simulation and transport. Below this threshold, several interactions are condensed into a single step and the energy deposited at the end of the condensed history step. A condensed history must provide: (1) a step length; (2) the direction change after the step; (3) the position change after the step; and (4) the inelastic scatter energy loss. The specifics of the condensed history technique are too involved to discuss in the context of this thesis, but can basically be described as follows:

1. Start with the electron fluence transport equation defined as:

$$\frac{d\Phi(\vec{x},\vec{\Omega},E,t)}{dt} = SO(\vec{x},\vec{\Omega},E,t) + vI[\Phi] \tag{2.3}$$

   where

   - Φ is the electron fluence
   - $SO(\vec{x},\vec{\Omega},E,t)$ is the electron source; i.e. the number of electrons created at position $\vec{x}$ with velocity $\vec{v} = (v,\vec{\Omega})$ and energy E per unit volume, energy, and solid angle per unit time by an external force or photon interaction with the medium at time t.
   - $I[\Phi]$ is the cross section dependent collision term and represents changes in particle fluence due to atomic collisions.

2. Pick an electron of initial energy E_0, direction $\vec{\Omega}_0$ and position $\vec{x_0}$ off of the particle stack

3. Sample the energy at which the next explicitly simulated interaction will occur

4. Solve the transport equation for final position, direction and energy

5. Sample the type of interaction (bremsstrahlung, elastic scatter, inelastic scatter or positron annihilation) and assign kinematics to the final state electron based on the interaction differential cross sections

The transport equation shown above is the simplest presentable form. When expanded and approximated in Monte Carlo, the solution of the transport equation is a function of restricted stopping powers, total and differential cross sections (bremsstrahlung, inelastic and elastic collisions), and various parameters that define the initial electron state. To approximately solve the transport equation, multiple scattering theory is applied to predict the final position and direction of the electron. The path length (s) of the particle is contained within the unrestricted stopping power (S) and is defined as:

$$s = \int_0^{E_0} \frac{dE'}{S(E)} \tag{2.4}$$

as is the energy loss

$$\Delta E = \int_0^s ds' S(s'). \tag{2.5}$$

The distance to the next discrete event is sampled from

$$\int_0^s ds' \sigma^{tot}(s') = -ln\, r \tag{2.6}$$

where r is a random number between 0 and 1. The three integrals above must be solved numerically and the procedure is quite involved. The approximated solution to the transport Eq.2.3 along with Eq.2.4 is known as the continuous slowing down approximation (CSDA).

The solution to the electron path length equation (Eq.2.4) assumes that the particle is in an infinite homogeneous medium. To include geometries of several media and finite boundaries, EGSnrc requires a boundary crossing algorithm. This is necessary when performing a condensed history step of an electron to avoid inaccurate calculations due to electrons wandering back and forth across an interface. As a simulated electron travels, EGSnrc regularly checks to see if the particle is close to a boundary. When the particle reaches the distance of closest allowable approach (set by the user), condensed history is turned off and the electron is allowed to cross the boundary in single scatter mode.

2.3 The Pinnacle^3 radiation therapy planning system

The Philips Pinnacle^3 Radiation Therapy Planning System (Philips Radiation Oncology Systems, Andover MA, USA) is a clinical tool used to formulate three dimensional dose distributions within CT datasets from external photon beams. Pinnacle uses one of the most accurate dose calculation algorithm available - the Collapsed Cone Convolution (Ahnesjö, 1989; Papanikolaou, Mackie, Meger-Wells, & Gehring, 1993; "Pinnacle^3 Physics Guide : External Beam and Brachytherapy", 2001; Carlsson & Ahnesjö, 2000; Metcalfe, Kron, & Hoban, 1997; Hasenbalg, Neuenschwander, Mini, & Born, 2007) (CCC). The CCC algorithm produces accurate dose predictions due to its explicit handling of both primary and secondary radiation spread within heterogeneous tissues. As its name suggests, the collapsed cone convolution method relies on a convolution integral to predict dose.

2.3.1 The convolution method

A convolution integral is defined as any integral that represents the overlap or "spread" of one function as it is shifted over another:

$$f * g = \int_{-\infty}^{\infty} f(\vec{\tau}) g(\vec{t} - \vec{\tau}) d^3\tau. \tag{2.7}$$

In Eq.2.7, f represents a three dimensional function in τ space that is spread to a point t by the convolving function g. In the CCC algorithm, the TERMA (total energy released due to primary interactions) is convolved by a kernel which defines the spread of energy from the TERMA due to secondary electrons and photons. The TERMA due to a monoenergetic beam from a point source (T_E) as defined by Ahnesjö (Ahnesjö, 1989) is written as:

$$T_E(\vec{r}) = \left(\frac{r}{r_0}\right)^2 \cdot \frac{\mu(E,\vec{r})}{\rho(\vec{r})} \cdot \Psi_E(\vec{r}_0) \cdot exp\left(-\int_{r_0}^{r} \mu(E,l) dl\right) \tag{2.8}$$

where

- $\vec{r}_0$ - position of a point on a reference plane (relative to the source)
- $\vec{r}$ - position of a point on a plane at depth (relative to the source)
- $\Psi_E(\vec{r}_0)$ - the energy fluence (energy per unit area) at $\vec{r}_0$
- $\mu(E,\vec{r})$ - linear attenuation coefficient of medium for photon at point $\vec{r}$
- $\rho(\vec{r})$ - mass density at point $\vec{r}$

To calculate the distribution of dose due to energy spread away from the initial TERMA site, the TERMA is convolved by a kernel which takes the point energy of the TERMA and spreads it over three dimensional space. The resulting dose is written as:

$$D(\vec{r}) = \frac{1}{\rho(\vec{r})} \int_E \int_V T_E(\vec{s}) \cdot \rho(\vec{s}) \cdot E, \vec{s}, \vec{r}) d^3 s dE \tag{2.9}$$

where $K(E,\vec{s},\vec{r})$ represents the energy deposition kernel. The above equation gives the contribution of secondary particle energy from all points $\vec{s}$ to point $\vec{r}$ over the spectrum of energies in the beam. Due to long calculation times, it is not practical to solve this integral

directly. Therefore, Eq.2.9 is redefined to remove the integration over energy. To that end, a polyenergetic kernel is defined as a sum of weighted monoenergetic kernels:

$$K(\vec{s},\vec{r}) = \frac{1}{\Psi(\vec{r_0})}\sum_i \Psi_i K(E_i,\vec{s},\vec{r}) \tag{2.10}$$

where Ψ_i is the energy fluence corresponding to the i^{th} energy bin and is defined as:

$$\Psi_i = \int_{\Delta E_i} \Psi_E(\vec{r_0})dE. \tag{2.11}$$

In a similar manner, the mean energy independent linear attenuation coefficient is defined as:

$$\bar{\mu}(\vec{r}) = \frac{1}{\Psi(\vec{r_0})}\sum_i \Psi_i \mu(E,\vec{r}). \tag{2.12}$$

With the preceeding approximations, the TERMA over all beam energies can be approximately written as:

$$T(r) = \left(\frac{r}{r_0}\right)^2 \cdot \frac{\bar{\mu}(\vec{r})}{\rho(\vec{r})} \cdot \Psi(\vec{r}) exp\left(-\int_{r_0}^{r} \bar{\mu}(l)dl\right). \tag{2.13}$$

Using the energy independent point spread function and TERMA of Eq's 2.10 and 2.13, Eq.2.9 is reduced to the spatial integral:

$$D(\vec{r}) = f(\vec{r})\frac{1}{\rho(\vec{r})}\int_V T(\vec{s})\cdot\rho(\vec{s})\cdot K(\vec{s},\vec{r})d^3s \tag{2.14}$$

where the first term of the preceeding equation, $f(\vec{r})$ is a correction factor to account for beam hardening [2] effects.

2.3.2 The collapsed cone convolution/superposition method

It is not practical to exactly solve the integral in Eq.2.14 over the entire volume of interest. The collapsed cone convolution algorithm utilizes several numerical methods and approximations to estimate the convolution integral. The collapsed cone convolution algorithm may be outlined as follows:

[2] beam hardening - a shift in a poly-energetic spectrum to a higher mean energy due to a relatively higher attenuation of low energy photons

1. Discretize the dose volume: It is not practical to calculate the TERMA to all points in space. To simplify the calculation, the dose volume is discretized into an array of three-dimensional voxels.

2. Raytrace the TERMA: A discrete set of rays are projected through the phantom to represent the incident x-ray source. The TERMA contribution to each intercepted voxel is calculated according to Eq.2.13.

3. Define a set of kernels: To create monoenergetic kernels, Mackie et al. (Mackie, Bielajew, Rogers, & Battista, 1988) developed an EGS4 Monte Carlo code called `SCASPH` . In the code, monoenergetic photons were forced to interact at a point. The space around the interaction site was voxelated within a spherical geometry (see Fig.2.2). Energy deposition due to secondary electrons and photons was scored

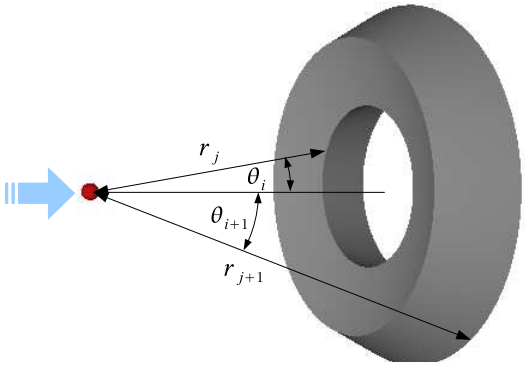

Figure 2.2: Calculating the kernel: Photons are forced to interact at a point. Using spherical coordinates, the space around the interaction site is divided into regions or voxels. A voxel is defined within the bounds: $r_j \rightarrow r_{j+1}$ and $\theta_i \rightarrow \theta_{i+1}$ where r is the radial distance from the interaction site and θ is the polar angle off of the axis of the incident photon.

within the voxel grid. In Mackie et al's work, the angular bin width was 3.75° for a total of 48 concentric cones. The outer radial boundary was 60 cm from the interaction site and contained 24 radial bins. Radial bin width varied with depth from 0.05 cm near the origin to 10 cm at the outer boundary. The higher resolution near the origin was needed to capture the high energy gradient in the vicinity of the interaction site. Kernel calculations were performed for energies ranging from

0.1-50 MeV. The resulting monoenergetic kernels were used to create polyenergetic kernels using the relation in Eq.2.10. Ahnesjö (Ahnesjö, 1989) observed that the polyenergetic kernels data could be reduced to a functional relationship of the form:

$$K(r,\theta) = \frac{A_\theta e^{-a_\theta r} + B_\theta e^{-b_\theta r}}{r^2} \tag{2.15}$$

where A_θ, B_θ, a_θ and b_θ are functions in the polar angle.

4. Discretize the direction of energy spread: a lattice of lines is created through the dose volume (see Fig.2.3). The lattice is defined such that the lattice lines intercept a voxel center as it is traced through a voxel volume. Energy spread is carried away from an interaction along these lines of energy spread.

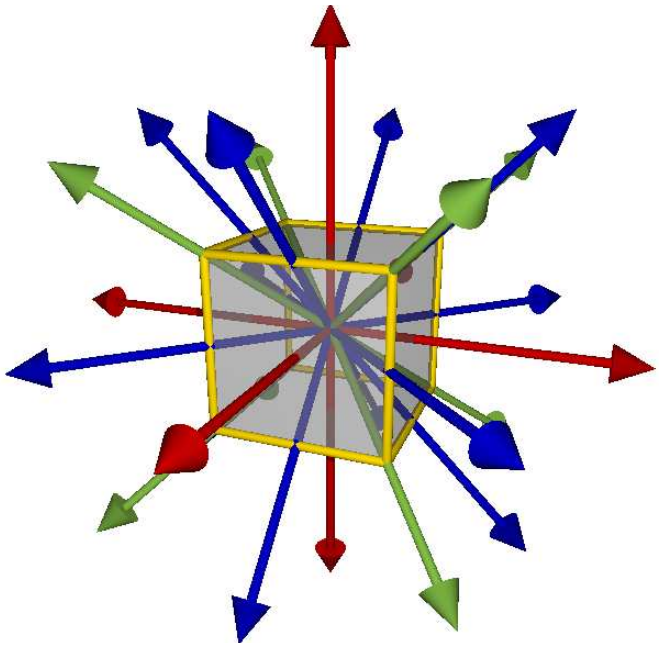

Figure 2.3: The collapsed cone approximation: Each voxel in the dose grid is subtended through it's center by 13 separate axes. The TERMA energy of the voxel is translated to adjacent voxels along these lines.

5. Discretize the kernel: The kernel defines the spread of energy as a function of radial distance and polar angle. The volume around the voxel is disretized into conical voxels. The axes of these cones align with the lines of interaction.

6. Account for density heterogeneity: To account for density heterogeneity, the kernel is scaled by the mean density between the TERMA source point and the point receiving the kernel contribution.

7. Perform the collapsed cone superposition: Each conical voxel has an associated energy spread relative to the energy of the initial source. Although this energy spread is associated with the conical volume, the collapsed cone method collapses the energy in a conical voxel onto the voxel axis (and line of interaction). For each voxel, the CCC algorithm superimposes the TERMA of the voxel with the kernel contribution of the surrounding voxels.

CHAPTER 3

MODELING A LINAC X-RAY BEAM

3.1 Introduction

The following chapter discusses the creation and verification of simulated clinical beams for both the EGSnrc Monte Carlo (Electron-Gamma Shower code as developed by the National Research Council of Canada) and the Philips Pinnacle^3 Radiation Therapy Planning System (Philips Radiation Oncology Systems, Andover MA, USA). Each beam model was made to reproduce the 6 MV x-ray particle fluence of the Varian Medical Systems model iX high energy linac (Varian Medical Systems, Palo Alto, CA, USA) illustrated in Fig.3.1. In the Varian clinical linac, a klystron generates RF energy which is carried by a waveguide to the gantry. The RF energy is fed into a second wave guide which accelerates electrons fired from an electron gun at the waveguide's end. The accelerated electrons are re-directed by a 270 degree bending magnet into the treatment head. The electrons create bremsstrahlung x-rays when set incident on a target. Within the treatment head, a collimator shapes the x-ray beam. A flattening filter shapes the beam profile to create uniform energy at depths below the isocenter. Jaws further shape the beam to create a rectangular field at a surface intersecting the isocenter. Although the construction of BEAMnrc and Pinnacle^3 beam models was very different, the benchmarking process was essentially the same. Within a watertank, percentage depth dose curves (dose as a function of depth along the z-axis in Fig.3.1) and crossplane/inplane dose profiles (dose along x and y axes of Fig.3.1 respectively) were measured. The parameters of each model were then adjusted to best match these measurements. At the Saskatoon Cancer Centre, measurements were taken in a 60 cm x 64 cm x 48 cm 3-D water scanner (WP700 Scanditronix-Wellhofer GmbH, Germany) using a cylindrical ion chamber (IC-15 Scanditronix-Wellhofer GmbH,

Germany) with an active volume of 0.13 cm^3 and diameter of 6 mm. The scanning tank (shown in Fig.3.2) was equipped with a remotely controlled positioning system. The ion chamber was attached to the positioning system in a vertical orientation and calibrated so that the origin was at a source-to-surface-distance (SSD) of 100 cm (i.e. the top of the water is 100 cm from top of the target in the treatment head) along the central beam axis. The ion chamber was then scanned across the beam to produce depth dose curves and crossplane/inplane profiles. Percentage depth dose curves were measured for fields ranging from 3x3 to 40x40 cm^2. For each of these fields, inplane and crossplane profiles were measured at depths of 1.5, 5.0, 10.0, 20.0 and 30.0 cm). This measured dataset was used to construct the beam models.

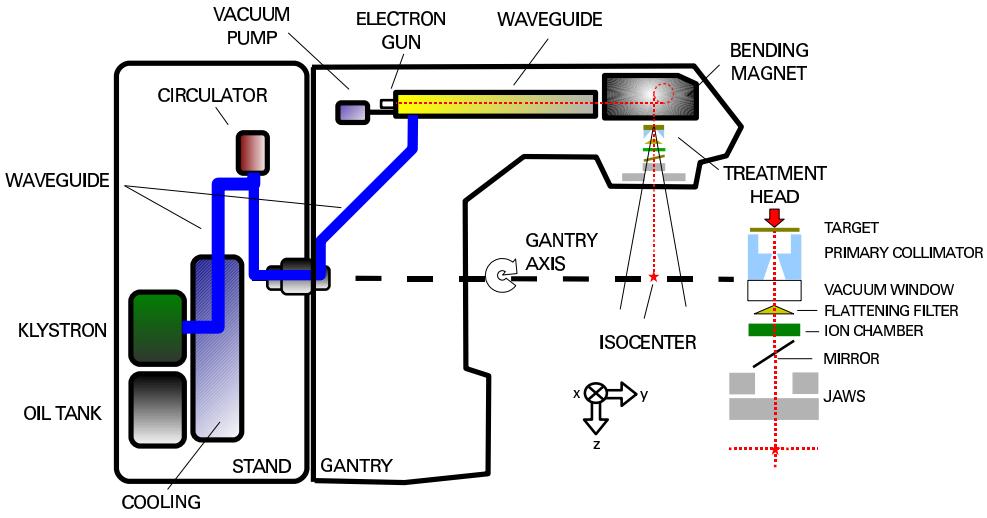

Figure 3.1: Schematic of the Varian high energy linac.

3.2 The EGSnrc/BEAMnrc Monte Carlo linac model

The BEAMnrc Monte Carlo (Rogers, Walters, & Kawrakow, 2009) is an EGSnrc user code which facilitates the modeling of clinical radiation therapy linacs. All components of a linac treatment head are coded as independent component modules. Each module is defined by a series of geometric rules for transporting across the boundaries of the

Figure 3.2: The Welhoffer water scanner.

module geometry. Within an input file, the user defines the dimensions and materials of each module to match their linac. The modules are then stacked together to produce a complete linac model. A BEAM simulation produces a phase-space file that scores the position, direction, charge, and energy at a user specified plane within the model. Once the model has been benchmarked against measured data, the phase-space file may be used as a particle source in subsequent simulations.

The Varian Medical Systems model iX linac treatment head including its target, primary collimator, flattening filter, ion chamber, mirror and jaws, was geometrically modelled using the BEAM code (see Fig.3.3). A 6 MeV electron beam was used as an initial particle source. The planar fluence distribution of the source was modelled by a 2-D Gaussian with a full-width-half-maximum (FWHM) of 0.125 cm. The source was placed incident on the front surface of the first component module which was a tungsten target. Within the target, the incident beam generated a cascade of bremsstrahlung x-rays and scattered electrons. Particles created in the target were transported through the treatment head geometry. A phase space scoring plane was defined just below the jaws. The kinematics of each particle crossing the plane was written to a phase space file. This process was repeated three times to produce three separate phase space files corresponding to a 4x4, 10x10 and 40x40 cm^2 field size. Ideally, it would have been useful to benchmark

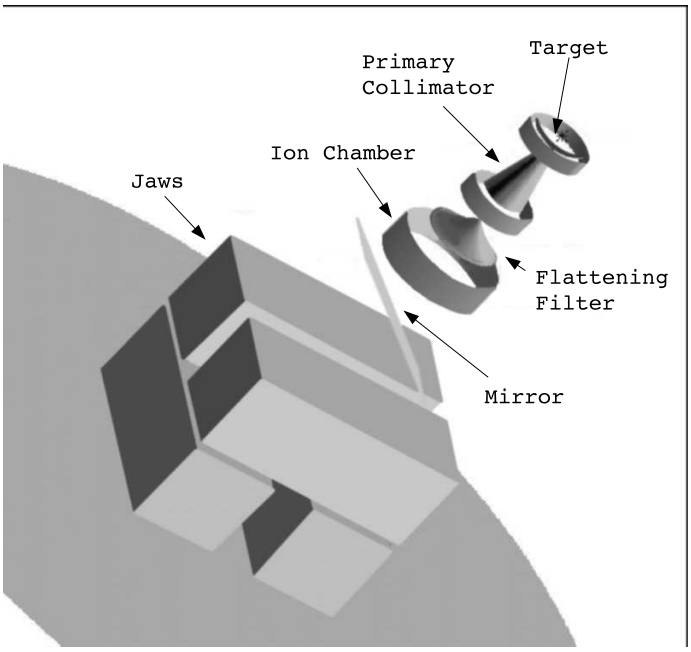

Figure 3.3: The linac treatment head as modelled in BEAMnrc (generated using the EGS_WINDOWS utility).

the smallest field (1x1 cm^2) used in this thesis. Unfortunately at the time of this work, an appropriate measuring device for smaller fields was not available.

BEAMnrc simulations were run using the PRESTA-II condensed history electron transport which produces the most accurate electron transport (Kawrakow, 2000a, 2000b). The PRESTA I boundary crossing algorithm was also used. As is common in the literature, the ECUT and PCUT parameters were set to 0.7 and 0.01 MeV respectively. All MC transport parameters were left at their recommended (default) values. Range rejection was turned on with a cutoff energy of 2.0 MeV. The only other variance reduction technique used was selective bremsstrahlung splitting (SBS). SBS is used to artificially increase the number of bremsstrahlung photons created by electron interactions (specifically in the target). When a bremsstrahlung photon is created, a probability distribution is calculated based on the energy and direction of the incident electron. This probability distribution reflects the number of bremsstrahlung photons which would exit the linac for a specified field size. SBS then splits the initial bremsstrahlung photon into several photons representative of the number of photons that would exit the linac. The weights of each split photon is equal to the inverse of the number of split photons created. By using SBS, the user can increase the

particle fluence out of the target thereby increasing simulation speed. The SBS technique was chosen over the more efficient directional bremsstrahlung splitting (DBS) technique as DBS was new at the time of this work. Also other published works on beam modeling successfully used the SBS technique.

To model the watertank in Monte Carlo, DOSXYZnrc was used. Like BEAMnrc, DOSXYZnrc (B. R. B. Walters, Kawrakow, & Rogers, 2007) is an EGSnrc user code. Its purpose is to calculate dose deposition within a three dimensional cartesian geometry. Specifically, transport and dose scoring geometries are defined on a rectilinear grid of voxels. Each voxel on the grid is assigned a material and density by the user. Transport through the geometry is carried out on a voxel by voxel basis. During simulation, DOSXYZnrc scores energy deposition in each voxel. At the end of a simulated run, energy deposition is converted into dose deposition. The resulting dose grid is then written to a file. From this file (using an BEAM utility called STATDOSE), the user can extract percent depth dose curves and inplane/crossplane profiles at several depths.

DOSXYZnrc watertank simulations were calculated within a 50 cm x 50 cm x 40 cm volume. To achieve appropriate statistics and spatial resolution, voxel size was varied depending on the field size. For the 4x4 cm^2 field the voxel size was 0.25 cm x 0.25 cm x 0.50 cm. For the 10x10 cm^2 field, the voxel size was 0.50 cm x 0.50 cm x 0.50 cm. For the 40x40 cm^2 field, the voxel size was 2.0 cm x 2.0 cm x 0.5 cm. To examine the penumbra of the 40x40 field, voxel resolution was increased to 0.5 cm at the ends of the x and y profiles. All three simulations (4x4, 10x10 and 40x40 cm^2 field sizes) were run using 1.5×10^9 incident histories. As in the BEAM simulations, ECUT and PCUT were set at 0.700 and 0.01 MeV respectively. The PRESTA-II condensed history algorithm was used in combination with the PRESTA-I boundary crossing algorithm. No other variance reduction technique was used.

Inplane and crossplane profiles as well as central axis depth dose curves were extracted from the simulation and compared to the Wellhofer measurements. From this initial comparison, the beam model was tuned to better match the measured results. It is known from the literature that the two key tuning parameters of a MC beam model are the initial electron energy and the FWHM of the fluence distribution of the electron beam. The initial

electron energy has an effect on the gradient of the depth dose curves. The spatial width of the electron beam effects the height of the profile "shoulders" with respect to the central axis dose. To achieve better agreement with measurement, the incident energy and spatial width of the electron beam were adjusted. A new set of BEAM model/DOSXYZnrc simulations was run. This process was iteratively repeated until agreement between MC and measurement was within a defined tolerance.

To compare the depth dose curves of Monte Carlo simulation to measurement, the percent difference, defined as:

$$PD_{MC,meas} = 100 \cdot \frac{(D_{MC} - D_{meas})}{D_{meas}} \tag{3.1}$$

was used. The desired agreement between MC and measurement was 1% which is the achievable tolerance limit set by the American Association of Physicists in Medicine (AAPM) Radiation Therapy Committee Task Group 53 (TG-53) in their study of quality assurance for clinical radiation therapy treatment planning (Fraas et al., 1998). To examine the agreement between MC and measurement for the dose profiles, a γ analysis (Low, Harms, Mutic, & Purdy, 1998) was used. The γ procedure, which seeks out the minimum distance between two dose profiles in position-dose space, is summarized as follows:

$$\gamma(x_{MC}, D_{MC}) = \min \sqrt{\left(\frac{x_{MC} - x_{meas}}{x_{TOL}}\right)^2 + \left(\frac{PD_{MC,meas}}{D_{TOL}}\right)^2} : \forall (x_{meas}, D_{meas}). \tag{3.2}$$

In Eq.3.2, x_{MC} is the lateral position on a Monte Carlo profile while x_{meas} is the lateral position on a measured profile. The x_{TOL} parameter defines the maximum allowed tolerance of the distance-to-agreement (DTA). The DTA is the distance between a point on the Monte Carlo distribution and a point on the measured distribution that have the same dose value. The D_{TOL} in the second term under the square root defines the maximum allowed percent difference in dose. If one examines the form of γ, one will notice that it defines an ellipse in percent difference-position space. The major and minor axes of the ellipse are x_{TOL} and D_{TOL} (or vice versa). In calculating gamma, one seeks a data point on the measured profile which minimizes both the DTA and percent difference in dose. When γ is less than one, a point in PD-position space is within the ellipse (i.e. the agreement between measurement and MC is within the allowable tolerance for both percent difference

and position uncertainty). When γ is greater than one, the agreement between measured and simulated points exceed the PD and position tolerances by a factor of γ. The values of x_{TOL} and D_{TOL} were set at 0.3 cm and 1% as outlined in TG-53.

The optimized MC beam model had a beam energy of 6.2 MeV and a FWHM of 0.14 cm which is consistent with several published results (Deng et al., 2000; Ding, 2002; Tzedakis et al., 2004; Aljarrah, Sharp, Neicu, & Jiang, 2006; Keall, Siebers, Libby, & Mohan, 2003; Sheikh-Bagheri & Rogers, 2002). The final set of simulations yielded a 4x4 cm^2 field size phase space file of 280 Mb containing roughly 9.6×10^6 incident particles. The 10x10 cm^2 phase space file was 1.2 Gb in size and contained roughly 4.4×10^7 particles. The 40x40 cm^2 phase space file was the largest at 1.7 Gb and 6.2×10^7 particles.

Fig.3.4 shows a comparison of measured watertank central axis depth dose profiles compared to those generated by both Monte Carlo and the Pinnacle^3 collapsed cone convolution algorithm. It is clear that, for the three field sizes, the percent difference between measurement and MC is less than 1% for most data points. Figures 3.5 and 3.6 show a comparison for the crossplane and inplane profiles respectively. The γ values for Monte Carlo profiles are shown in Fig.3.7. In the figure, it is confirmed that the measured and Monte Carlo distributions are equivalent within the criteria defined in TG-53 for the 4x4 and 10x10 fields. For the 40x40 field, the value of γ increases with distance from the central axis. However, the majority of the points with a γ greater than one are in the low dose tail of the penumbra. The worst γ value for the Monte Carlo data is roughly 2.75. It is clear that there is a discrepancy between Monte Carlo and measured dose values in the penumbra of the 40x40 cm^2 field. The poor agreement is possibly due to perturbations in dose due to the watertank surface and motor drive mechanism. These structures were not explicitly modeled for the Monte Carlo calculations.

With the BEAM model benchmarking complete, phase space files were generated for the field sizes 1x1, 3x3, 5x5 and 7x7 cm^2. The only difference in these models was the size of the jaw opening. These four phase space files (outlined in Table 3.1) along with the original 10x10 cm^2 field were used in the simulations of this thesis.

Table 3.1: Specifications of the 6 MV BEAMnrc Monte Carlo linac model phase space files.

Field size (cm^2)	# number of particles	# of photons	file size (Gb)
1x1	36 399 127	36 277 666	1.0
3x3	93 957 752	93 637 553	2.5
5x5	264 140 263	263 169 525	7.0
7x7	485 585 022	483 731 356	14.0

3.3 The Pinnacle^3 treatment planning system linac model

Before one can use the Pinnacle^3 TPS for clinical dose calculations, one must create and benchmark a clinical beam model in the software. As was the case in the previous section, a beam model was parameterized and optimized to best match experimental measurements. The Pinnacle^3 TPS has a graphical user interface where one can perform this task. The Pinnacle^3 commissioning process is as follows:

1. Define the energy spectrum: In Pinnacle, the energy spectrum (relative number of photons at each energy) is defined for a discrete number of energy bins. The user may define their own spectrum or start with a pre-defined spectrum that closely matches the energy of their specific machine. This energy spectrum is used to create a planar fluence along the direction of the beam.

2. Add the electron contamination: A clinical linac x-ray beam will contain some electrons created in the treatment head of the machine. To account for the dose due to these electrons, an electron contamination function (ECF) is superimposed onto the dose distribution. The basic shape of the function is flat at and near the surface with an exponential decline to zero at deeper depths. The user can define the maximum depth of electron contamination, the rate of exponential decline, the slope and width of the linear portion of the curve, off-axis fall-off, and the change of EC due to field size changes. For a 6 MV linac as modelled in Pinnacle, the electron contamination

falls to zero at 3 cm depth. Generally, the Pinnacle user manual suggests a maximum ECF depth equal to the depth of maximum dose plus one centimeter.

3. Account for Flattening Filter Contamination: The flattening filter of a linac increases the photon fluence and softens the beam (filters out the number of high energy photons relative to low energy photons) as a function of off-axis distance. Flattening filter attenuated beams produce crossplane and inplane profiles with horns or raised shoulders near the edge of the field. To reproduce the horns in measured data, the planar photon fluence is modified by an inverted cone function. This function reduced the spectrum weight as a function of off axis angle. The width and height of the inverted cone can be adjusted to best reproduce the horns of the measured data.

4. Reproduce the penumbra shape: The penumbra observed in profile data is largely due to a finite electron source size. To produce a penumbra in the beam model, a Gaussian blurring function is convolved with the incident fluence. By adjusting the magnitude and full width half maximum of the blurring function, the user can adjust the penumbra to match measured data.

5. Account for Wedges: To change the shape of the beam, wedges are sometimes inserted into the path of the field. The TERMA below the wedge is modified to account for wedge attenuation. To account for scatter off the wedge, the modifier scatter factor may be adjusted to best match wedge measurements.

6. Adjust all parameters to match a wide variety of measured data: For the model to be deemed valid, it must be able to reproduce profiles and depth dose curves for several field sizes.

When the first Varian iX series linac was purchased for the Saskatoon Cancer Centre, Pinnacle^3 beam models of the 6 and 15 MV x-ray modes were created by the medical physics staff. When new linacs were purchased at the center, their beam parameters were tuned to create depth dose curves and profiles that matched the original linac data. This allowed for the implemantation of a single Pinnacle beam model for all linacs at the Centre. For this thesis, the pre-existing 6 MV beam model was used for all Pinnacle^3 calculations.

A comparison of Pinnacle[3] CCC and measured depth dose curves and profiles (Figures 3.4-3.6) showed good agreement. CCC depth dose curves were within 2% of those measured. The γ values along the crossplane and inplane profiles, shown in Fig.3.8, were less than or equal to one for the 10x10 field. For the 4x4 field and the central portion of the 40x40 field, the upper γ value was just below 2. As was the case in the Monte Carlo comparison, there was poor agreement in the penumbra region of the 40x40 field with γ values as high as 2.75.

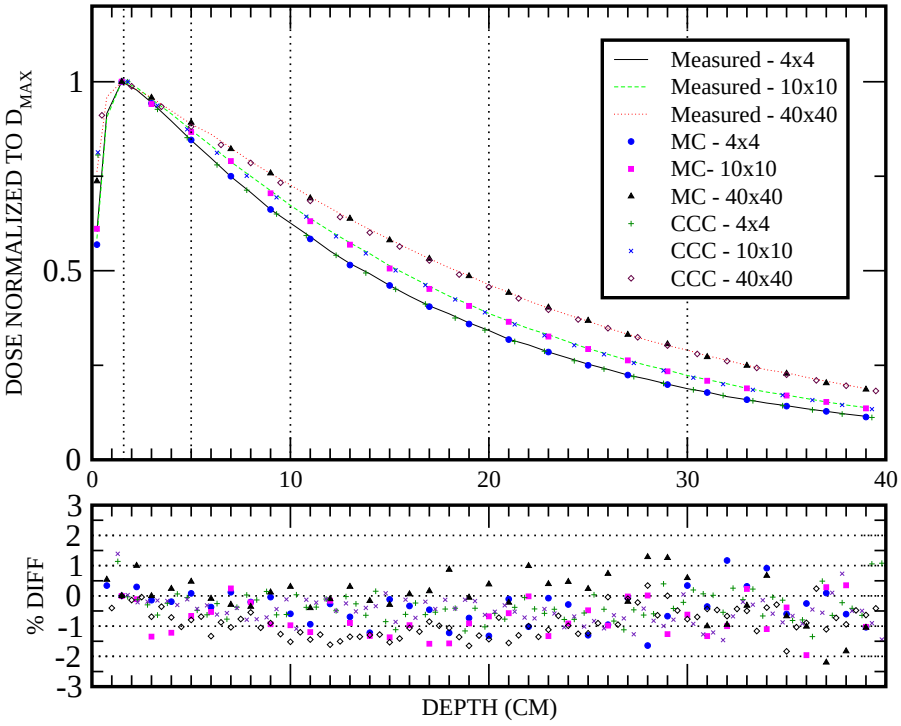

Figure 3.4: 6 MV central axis depth dose curves for a simulated Varian iX series linac. The three curved lines represent the depth dose curves for a 4x4, 10x10 and 40x40 cm^2 as measured using an IC-15 cylindrical ion chamber (with an active volume of 0.13 cm^3 and diameter of 6 mm) and Wellhofer watertank/scanner. The circle, square and triangle points represent the same curves as derived in a DOSXYZnrc simulation using a modelled BEAMnrc phase space source. The plus, cross and diamond points represent the same curves as derived in Pinnacle[3] CCC calculations. The uncertainties in the Monte Carlo dose values were less than 0.5%.

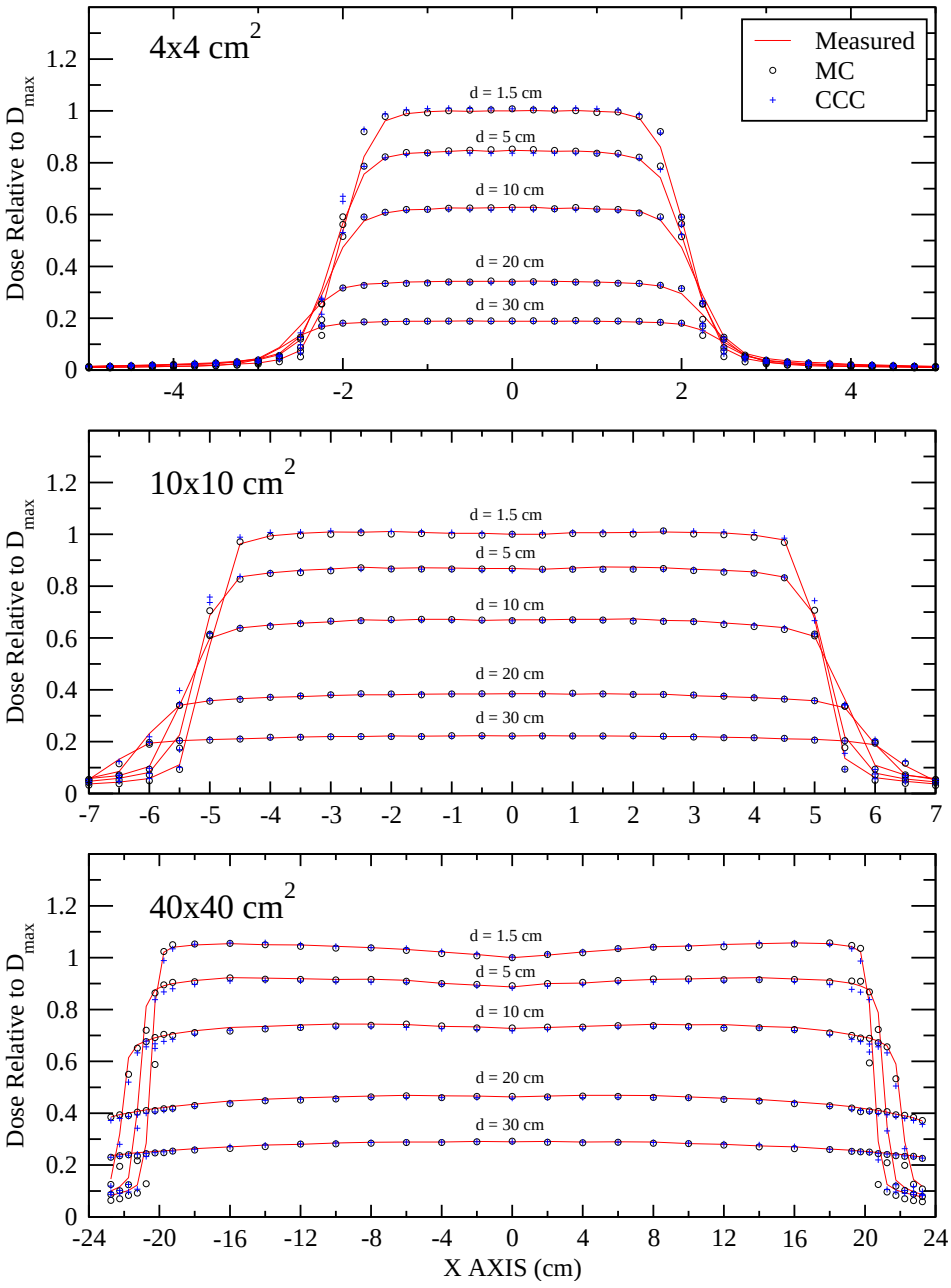

Figure 3.5: 6 MV crossplane profiles for a simulated Varian iX series linac. The solid lines in each figure represent crossplane profiles measured using an IC-15 cylindrical ion chamber and Wellhofer watertank/scanner. The circles represent profiles derived from Monte Carlo simulation while the plus symbols represent profiles derived using the Pinnacle CCC algorithm. From top to bottom, the profiles are at depths of 1.5, 5, 10, 20 and 30 centimeters.

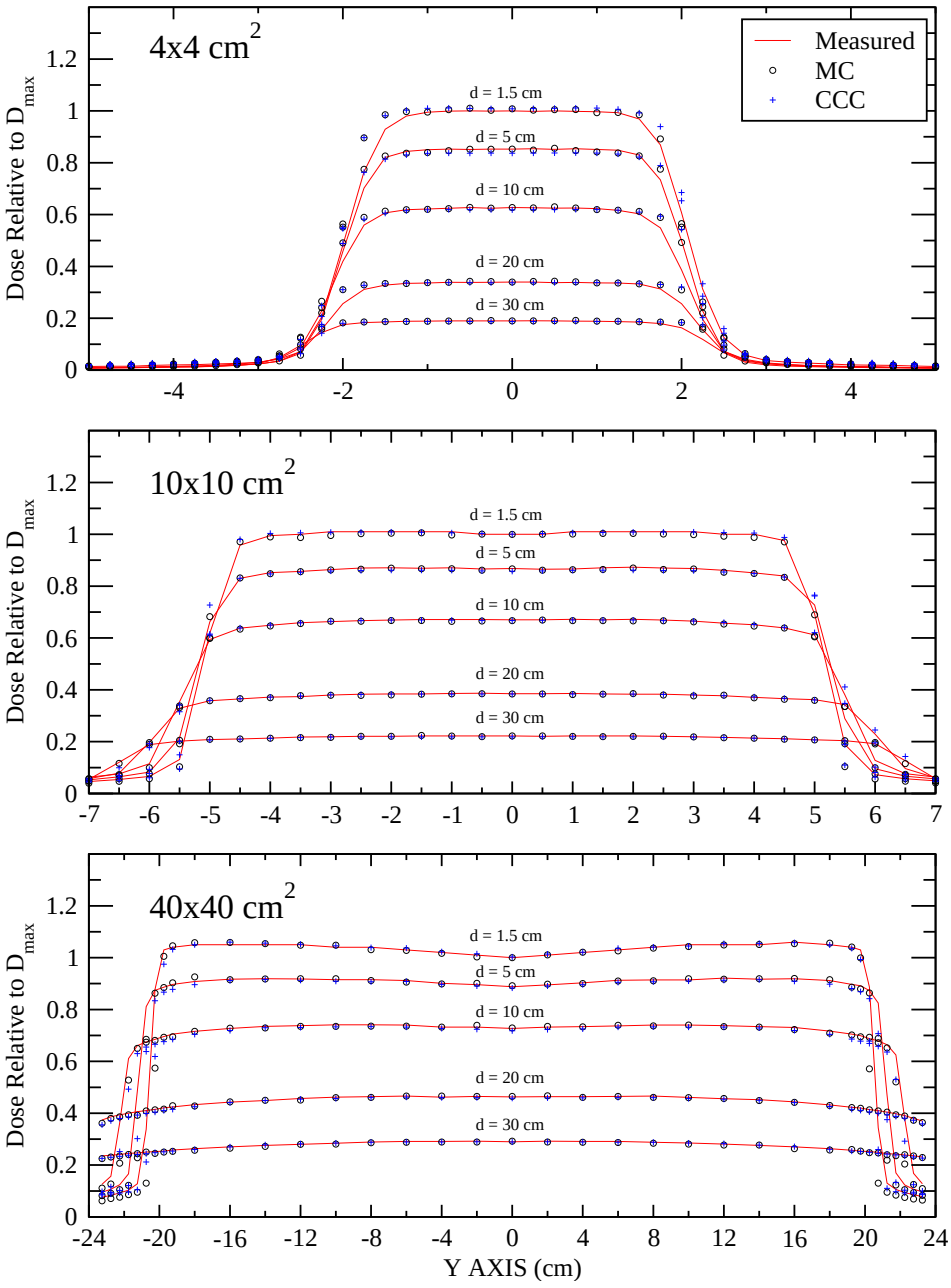

Figure 3.6: 6 MV inplane profiles for a simulated Varian iX series linac. The solid lines in each figure represent crossplane profiles measured using an IC-15 cylindrical ion chamber and Wellhofer watertank/scanner. The circles represent profiles derived from Monte Carlo simulation while the plus symbols represent profiles derived using the Pinnacle CCC algorithm. From top to bottom, the profiles are at depths of 1.5, 5, 10, 20 and 30 centimeters.

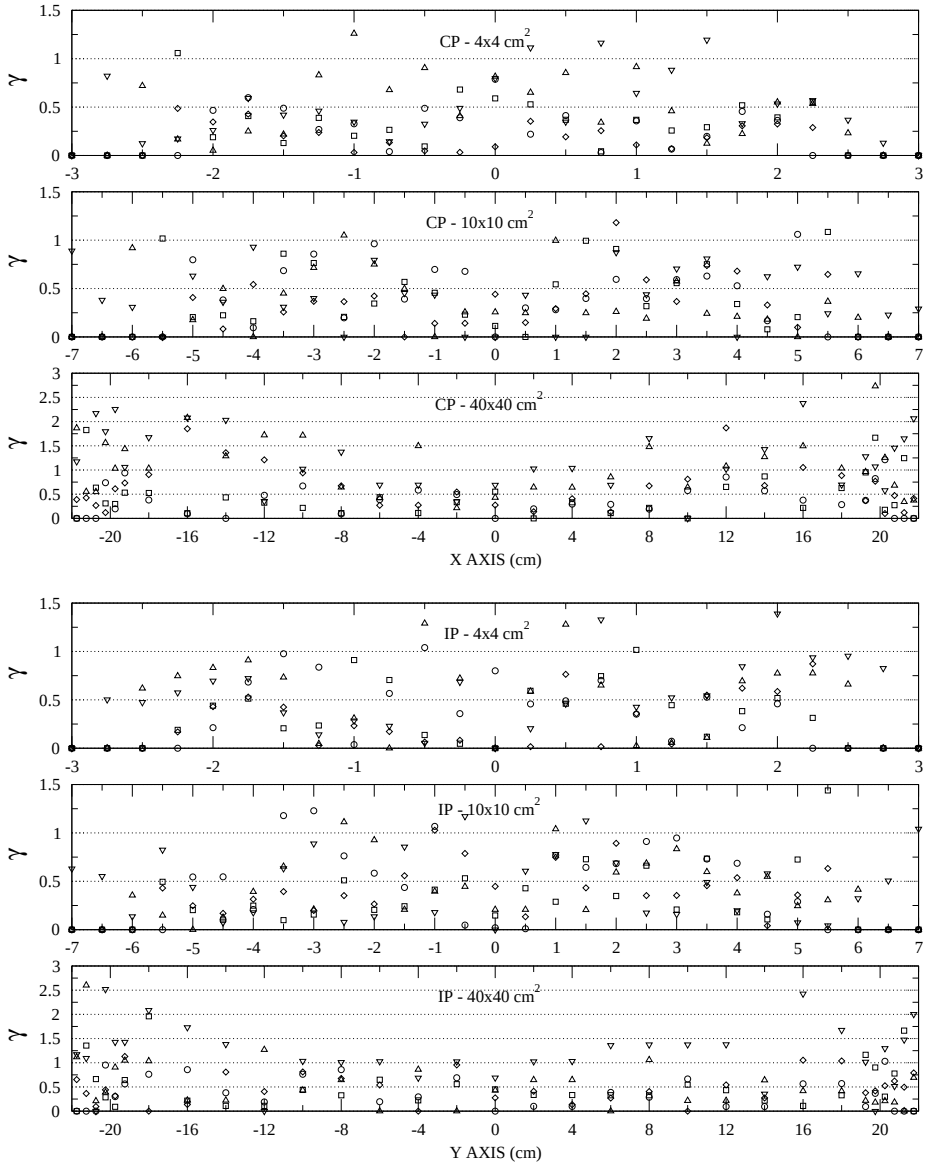

Figure 3.7: The γ values for crossplane and inplane profiles - Monte Carlo vs. Measurement. The circles, squares, diamonds, up-pointed triangles and down-pointed triangles represent the γ values for depths of 1.5, 5, 10, 20 and 30 cm respectively.

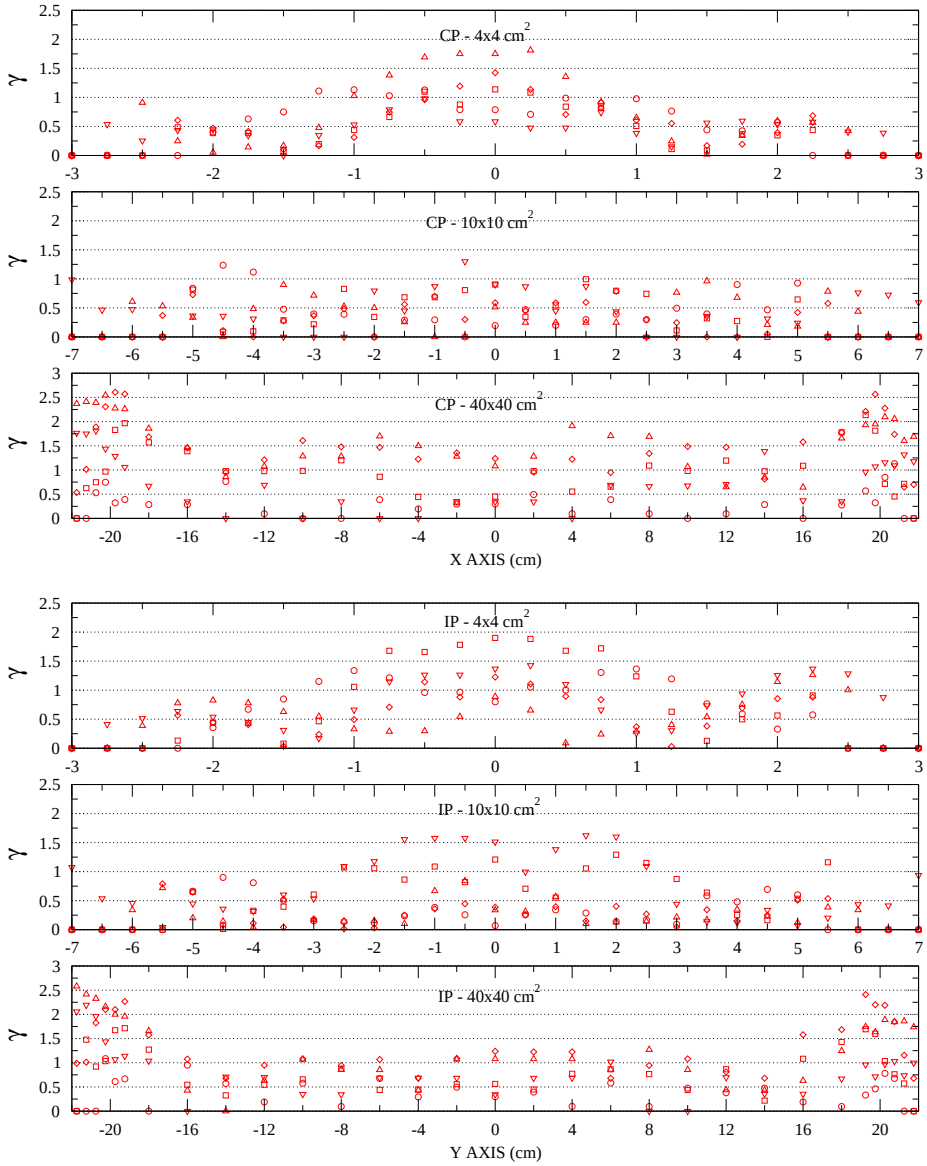

Figure 3.8: The γ values for crossplane and inplane profiles Pinnacle^3 CCC vs. Measurement. The circles, squares, diamonds, up-pointed triangles and down-pointed triangles represent the γ values for depths of 1.5, 5, 10, 20 and 30 cm respectively.

CHAPTER 4

ANATOMY AND PHYSIOLOGY OF THE LUNG

4.1 Introduction

In the human body, the extraction of oxygen and the expulsion of carbon dioxide is facilitated by the lungs. Bound by the diaphragm caudally (bottom), the spine to the posterior (back), the ribcage laterally (outside) and the mediastinum medially (midline), the lungs (see Fig.4.1) enclose a network of airways, arteries, veins and porous tissues. The purpose

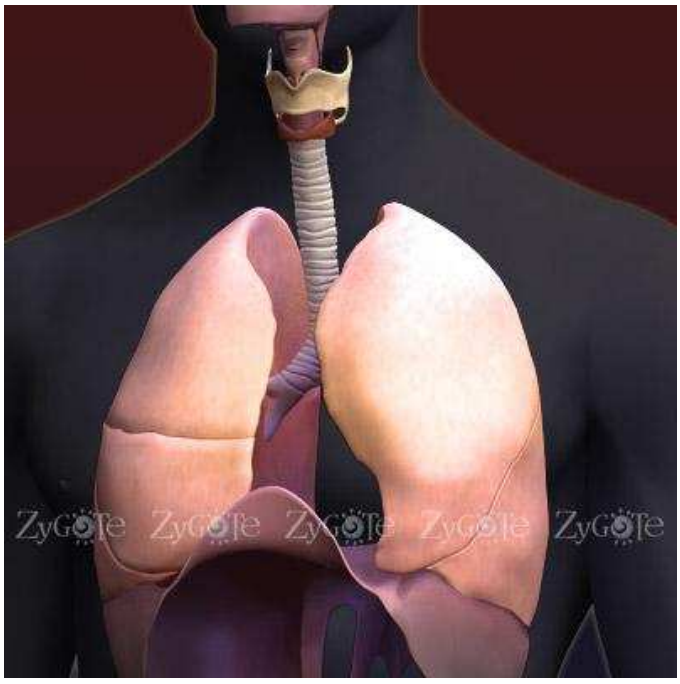

Figure 4.1: The human lung. The lung surface is bound by the mediastinum medially, the diaphragm caudally and the ribcage laterally (courtesy of 3DScience.com).

of this chapter is to provide an overview of the physical structures and basic function of the human lung. Included will be a description of the bronchial, arterial and venous branching trees as well as the supporting connective tissues contained within. These structures were incorporated into Monte Carlo models of the lung (see Chapter 5). Other anatomic structures such as the lymphatic and neural systems are assumed to be a part of the connective tissue sub-structure. The basic mechanics of respiration such as diaphragm and ribcage movement, and tissue deformation will also be presented here.

4.2 Lung mass, density and volume

The mass of the lungs is roughly 900-1000 g, half of which is attributed to the circulatory blood. Within the lungs, air volume can vary from 1.5 to 7 litres over the respiration cycle, resulting in an overall density range of 0.1-0.3 g/cm^3. The distribution of tissues within the lung volume is not uniform. From the hilus (where air and blood enter/exit the lung) to the periphery, lung density is reduced by as much of a factor of ten ("Textbook of respiratory medicine", 2000). There is also a density gradient in the cranial caudal direction of the lung due to the orientation of the bronchial, venous and arterial networks. The majority of alveolar tissues, where gas exchange takes place, are located in the outer 30% of the lung volume. As a result, density variation as a function of respiration is greatest at the lung's periphery.

4.3 The connective tissues

The connective tissues of the lung serve the function of perserving overall lung shape while allowing deformability during the breathing cycle. There are three types of tissues that make up the the lung: (1) peripheral tissues, (2) septal tissues, and (3) axial tissues (see Fig.4.2).

Peripheral tissues compartmentalize the lung to create independent gas exchange regions. Each lung is divided into several lobes (3 in the right lung, 2 in the left) which are divided into segments (10 in the right, 8 in the left) which are again divided into respiratory

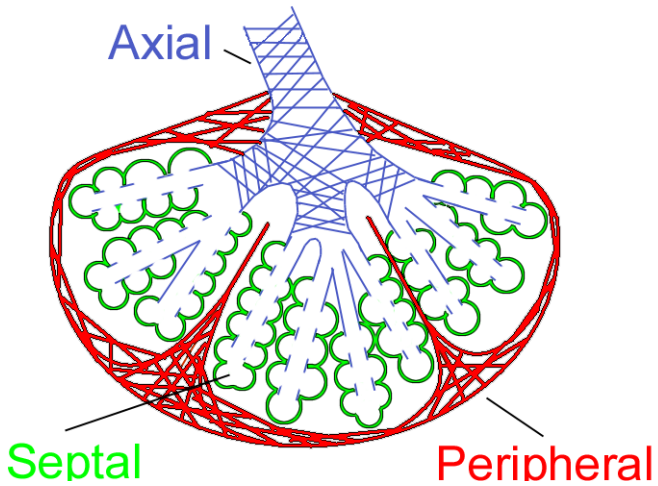

Figure 4.2: The fibrous continuum of the lung. Peripheral fibers compartmentalize the lung. The compartments are further divided by septal fibers, creating alveolar ducts and sacs. Axial fibers create the structure of the branching conduits of the lung.

units. Within the respiratory units, septal fibers divide the remaining space into groupings of cavities and ducts. Lastly, axial fibers give rigidity and structure to the bronchial, arterial and venous channels throughout the lung. Although each of these tissues is structurally distinct, they are assumed in this thesis to be dosimetrically similar.

4.4 The bronchial tree

To effectively perform the gas exchange process, it is important that all parts of the lung have a conduit to the atmospheric environment external to the body. This is the function of the bronchial tree. The bronchial tree (Fig.4.3) is a continuous network of tubular airways that facilitates the transport of oxygen and carbon dioxide between the gas exchanging tissues of the lung and the outside environment. Through a series of bifurcations, the bronchial tree radiates from a central airway (the trachea), uniformly filling the lung volume. The pattern of branching is best described as an irregular dichotomy. Each branch in the bronchial tree gives rise to two smaller daughter branches. The first generation off the trachea contains two offspring. Those branches each have two daughters giving a total of four branches in the second generation and so on. If all branches in the same generation

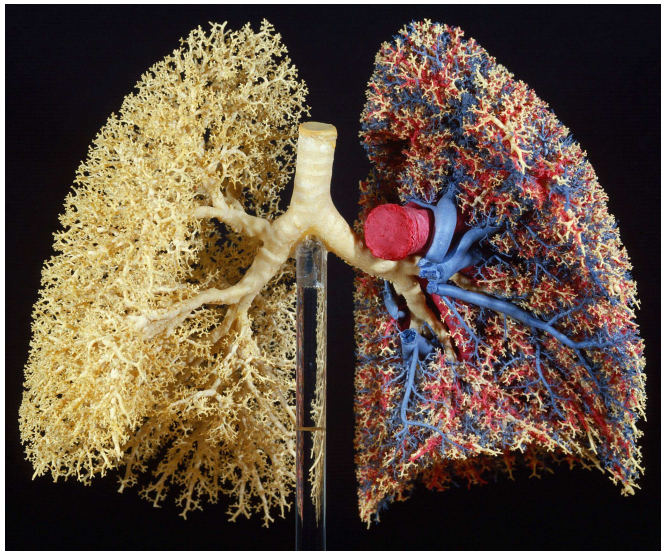

Figure 4.3: A cast of the bronchial arterial and venous trees of an adult lung. Taken from reference ("Textbook of respiratory medicine", 2000).

produce two bifurcations, the number of branches (N) at each generation (z) is:

$$N(z) = 2^z \tag{4.1}$$

All branches of the same generation have roughly the same diameter. Measurement (Weibel, 1963) has shown an approximate relationship between branch diameter (d_z) at generation z and trachea diameter (d_o) as:

$$d_z = d_0 2^{-\frac{z}{3}}. \tag{4.2}$$

This scenario describes a regular dichotomy. Due to its irregular shape, some regions of the lung contain more generations than others. Consequently, there is a wider variation in the diameter of branches at the same generation. This lack of symmetry in path length and diameter represents an irregular dichotomy.

There are two classes of airways found within the bronchial tree (see Fig.4.4). First are the bronchi. Bronchi are composed of rigid fibrous tissues and sparce amounts of smooth muscle, protected by cartilagenous plating. The function of the bronchi is to ensure an unobstructed flow of air to the lung periphery. The second class of branch are the bronchioles. Mostly composed of smooth muscle with no plating, the bronchioles are designed to close off, trapping air in the periphery to prevent lung collapse. Two sub-classes of

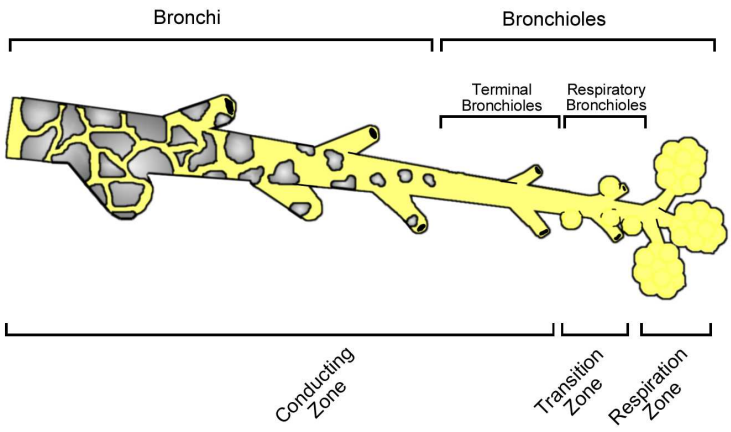

Figure 4.4: There are two types of bronchial branches. The cartilagenous plated bronchi and the smooth collapsable bronchioles. The branching tree can be broken into three regions. The conduction zone where only air is transported, the respiration zone where gas exchange occurs and the transition zone which joins the two.

bronchioles are the respiratory and terminal bronchioles. Respiratory bronchioles differ from normal bronchioles in that they have saccular cavities called alveoli protruding from their walls. They are part of the gas exchanging region of the lung and mark the end point of the bronchial tree. Terminal bronchioles are the last bronchioles before the respiratory bronchioles begin to appear. Transition from bronchi to bronchioles occurs when the diameter of branches reaches 1.0 mm in diameter. The terminal bronchioles appear when branch diameter drops below 0.5 mm.

To group branches of similar characteristics, several counting schemes have been proposed. The first was developed by Ewald Weibel (Weibel, 1963). In Weibel's approach (see Fig.4.5a), branches are counted from the trachea down to the periphery. The trachea is assigned a generation value of zero. The two main bronchi off the trachea are labelled generation one, their offshoots, generation two, and so on, resulting in approximately twenty-three generations down to the respiratory bronchioles.

Due to irregular dichotomy conditions, some researchers found the Weibel counting scheme inadequate for matching branches of similar size and structure. Branches of the same generation varied too greatly in both diameter and length to be classified as similar. The preferred approach was to count branches from the periphery towards the trachea.

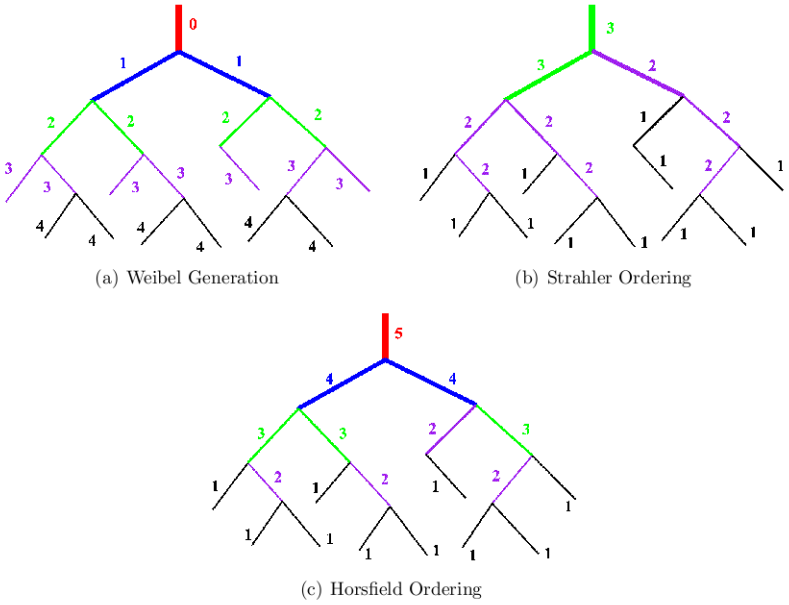

Figure 4.5: The Weibel, Strahler and Horsfield branch counting schemes.

This type of counting scheme classifies groups of branches in terms of "order" to distinguish it from the generation label used by Weibel.

There are two prevalent ordering schemes referred to in the literature. The first is the Strahler approach (see Fig.4.5b). In the Strahler approach, the peripheral branches are given an order of one. For a preceeding branch to increase in order, both its prodigy must be of equal order. If they are not, then the preceeding branch is assigned an order equal to the greater order of the two daughter branches. Once all branches are assigned an order, contiguous branches with the same order are considered to be one branch. Using this method, the bronchial tree contains about ten Strahler orders. A second ordering scheme is that of Horsfield (see Fig.4.5c). As in Strahler ordering, the peripheral branches of the tree are given an order of one. Each parent branch is given an order value equal to the greater value of the two daughters order plus one. This thesis will concentrate on measurements taken with the Strahler ordering scheme.

There is a functional relationship between the number, diameter and length of branches versus Strahler order (see Fig.4.6). When plotted on a semi-logarithmic graph, a logarithmic relationship becomes obvious. The anti-log of the absolute value of the slopes des-

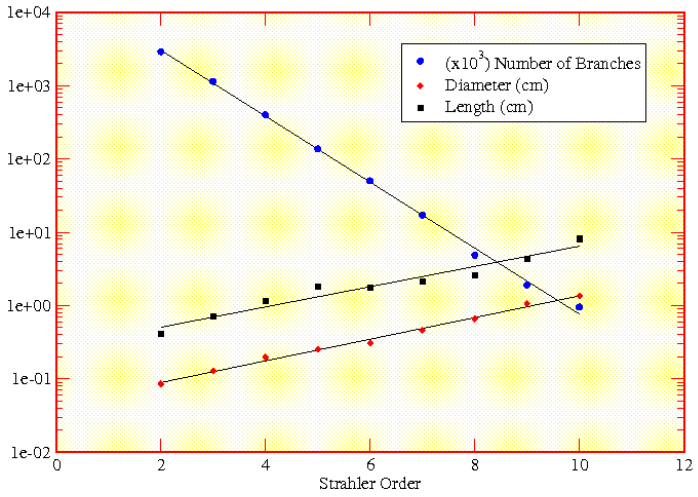

Figure 4.6: Semi-log plot of branch number, diameter and length vs. Strahler Order for the bronchial tree. The data shown are a combination of both physical measurement of a resin cast and extrapolation for missing branches. The data were reproduced from reference (Crystal & West, 1991).

ignate the branching ratio (R_b), length ratio (R_l) and diameter ratio (R_d) respectively. For symmetric branching, the value of R_b is exactly 2 while the diameter and length ratios, based on the expectation of minimal work (Murray, 1926; Horsfield & Cumming, 1967), are proportional to the cube root of the branching ratio.

$$R_d = R_l = R_b^{1/3} \tag{4.3}$$

The value of R_b is used to parameterize the asymmetry of the bronchial tree where, the more R_b varies from two, the more asymmetric the tree is. Table 4.1 summarizes the published values of R_b, R_d, and R_l.

There is an abundance of data available on the morphometry of the bronchial tree (Weibel, 1963; Merryn et al., 2004; Phillips & Kaye, 1995). Fig.4.7 shows the labeling convention used in the morphometry field. A non-terminal branch has one parent, one sister, and two daughter branches. It has a length (L) and a diameter (D) that is generally smaller than that of its parent and larger than that of its daughters. The branching angle (θ) of a daughter is defined with respect to the central axis of the parent branch. The major

Table 4.1: Branching, length and diameter ratios of the bronchial tree (Horsfield & Thurlbeck, 1981b; Merryn et al., 2004; Horsfield et al., 1976).

Ratio	Strahler Ordering
R_b	2.51-2.81
R_l	1.33-1.46
R_d	1.33-1.45

daughter is the larger of the two sibling branches with the remaining branch being labelled the minor daughter. The branching plane is defined by a normal vector in the direction of the cross product of the two daughter branches. The angle between consecutive branching planes is labelled ϕ and is typically close to ninety degrees.

One pattern observed in morphometric studies of the bronchial tree is the length to diameter ratio (L/D). The L/D ratio was found to be nearly constant regardless of where in the tree the branch was located. Even with the variation in both length and diameter within an order, the majority of branches have an L/D ratio close to three. The statistical spread in the values of L/D for a particular order is considered a quantitative measure of the irregularity or asymmetry of the tree. Published values for the L/D ratio, along with other measured morphometric properties of the bronchial tree are summarized in Table 4.2.

4.5 The arterial and venous trees

The pulmonary circulation is a network of arteries and veins responsible for the transport of oxygen and carbon dioxide between the heart and the gas exchanging regions of the lung. Much like an exchanger, CO_2 rich blood is routed from the heart to the lungs where it is replaced with oxygen and returned to the heart. Outward flow of CO_2 is handled by the pulmonary arteries which distribute carbon dioxide throughout the lung volume. Pulmonary veins absorb oxygen at the gas exchange site and bring it back to the heart.

The pulmonary vasculature shares many characteristics with the bronchial tree. Pul-

Table 4.2: Published data on the branching geometry of the bronchial tree.

	Published	Reference
L/D	3.04 ± 2.20	(Merryn et al., 2004)
	3.09, 3.14	(Sauret, Halson, Brown, Fleming, & Bailey, 2002)
	3.25 ± 0.65	(Weibel, 1963)
L/D_{minor}	3.63 ± 2.57	(Merryn et al., 2004)
	2.96 ± 0.97	(Phillips & Kaye, 1995)
L/D_{major}	2.48 ± 1.79	(Merryn et al., 2004)
	2.71 ± 1.13	(Phillips & Kaye, 1995)
D/D_{parent}	0.71 ± 0.14	(Merryn et al., 2004)
	0.83, 0.78	(Sauret et al., 2002)
	0.79	(Weibel, 1963)
	0.76	(Krause, Bandt, Schulz, & Shulz, 1995)
D_{min}/D_{parent}	0.66 ± 0.12	(Merryn et al., 2004)
D_{maj}/D_{parent}	0.79 ± 0.12	(Merryn et al., 2004)
	0.86	(Phillips & Kaye, 1995)
D_{min}/D_{maj}	0.85 ± 0.14	(Merryn et al., 2004)
	0.82, 0.74	(Sauret et al., 2002)
	0.86 ± 0.01	(Weibel, 1963)
	0.77	(Phillips & Kaye, 1995)
L_{min}/L_{maj} $(L_{min} < L_{maj})$	0.52 ± 0.23	(Merryn et al., 2004)
	0.58	(Sauret et al., 2002)
	0.62 ± 0.20	(Weibel, 1963)
L/L_{parent}	1.18 ± 1.20	(Merryn et al., 2004)
	0.94 ± 1.37	(Krause et al., 1995)
θ	$36.11^\circ \pm 20.85^\circ$	(Merryn et al., 2004)
	37.28°	
θ (D $\geq$ 4 mm)	33.98°	(Merryn et al., 2004)
	32°	(Horsfield, Dart, Olson, Filley, & Cumming, 1971)
θ (4 mm $>$ D $\geq$ 3 mm)	41.06°	(Merryn et al., 2004)
	30°	(Horsfield et al., 1971)
θ (3 mm $>$ D $\geq$ 2 mm)	36°	(Horsfield et al., 1971)
θ (2 mm $>$ D $\geq$ 1 mm)	43°	(Horsfield et al., 1971)
θ (1 mm $>$ D $\geq$ 0.7 mm)	50°	(Horsfield et al., 1971)
ϕ	$76.05^\circ \pm 45.73^\circ$	(Merryn et al., 2004)

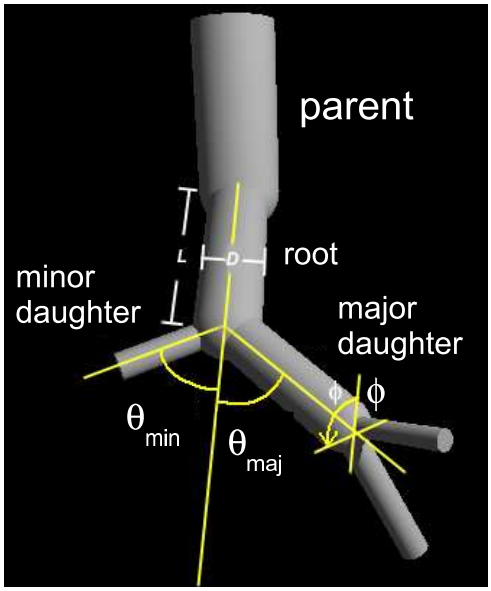

Figure 4.7: The Bronchial labeling scheme. A branch of diameter D and length L has one parent and two daughters. The daughter with the larger diameter is the major daughter and the smaller diameter the minor daughter.

monary arteries and veins spread throughout the lung in a series of dichotomous branches. This similarity is particularly true for the pulmonary arteries which closely mimic both the path and physical size of the bronchial network. The venous tree differs in that it takes an inter-lobular path, independent of the bronchial branches. In addition, the venous tree converges to two separate branches off the heart, contrary to the tree analogy. Below a branch diameter of 1.5 mm, the similarity with the bronchial tree begins to diverge as the pulmonary vasculature sprouts additional (superluminary) branches to adjacent groupings of alveoli.

Details of the pulmonary arterial structure were first quantified in a paper by Singhal et al. (Singhal, Henderson, Horsfield, Harding, & Cumming, 1973). In Singhal's work, a resin cast of an arterial tree was taken from a recently deceased subject and ordered using the Strahler convention. The branches of each order were counted, and their diameters and lengths measured. A total of 12 orders were counted for diameters ranging down to 0.1 mm. When the number, diameter or length of branches were plotted against Strahler

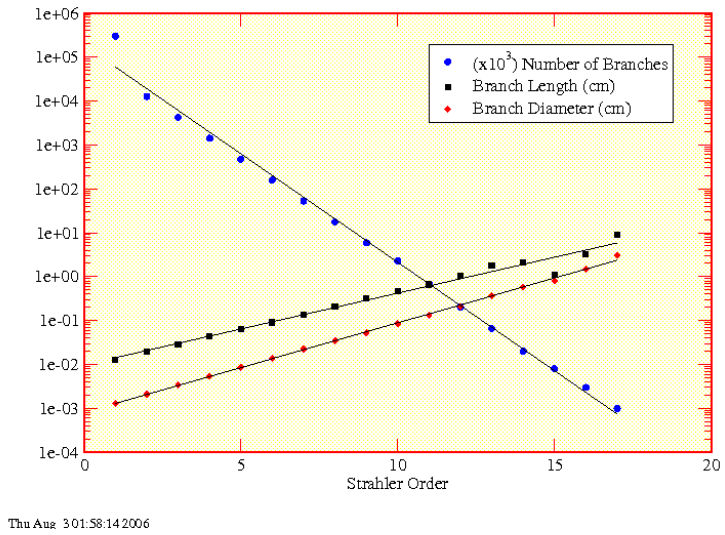

Figure 4.8: Semi-log plot of branch number, diameter and length vs. Strahler Order for the arterial vasculature. The data shown are a combination of both physical measurement of a resin cast and extrapolation for missing branches. The data were reproduced from reference (Singhal et al., 1973).

order, a semi-logarithmic relationship was found similar to that observed in the bronchial tree (see Fig.4.8).

A similar analysis of the venous tree was performed by Horsfield et al. (Horsfield & Gordon, 1981). Measurements were made on several resin casts containing branches as small as 0.02 mm. Extrapolations were made down to 15 Strahler orders in branch number, diameter and length to create a model of the venous tree (see Fig.4.9).

There is little anatomic data on the geometric characteristics of the pulmonary vasculature. However, based on the argument that turbulent flow should be minimized, it is assumed that the arterial and venous trees should closely mimic the structure of the bronchial tree.

4.6 The terminal respiratory unit

The terminal respiratory unit (TRU), shown in Fig.4.10, is the junction that connects the bronchial, arterial and venous trees. Roughly spherical in shape, a terminal respiratory

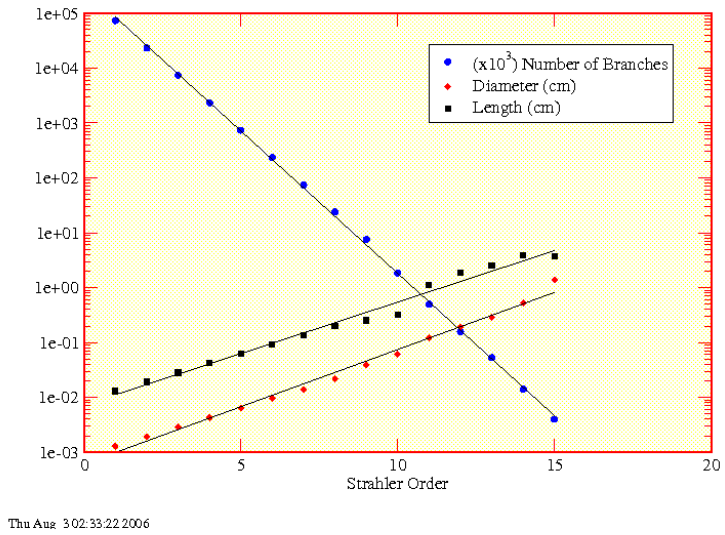

Figure 4.9: Semi-log plot of branch number, diameter and length vs. Strahler Order for the venous vasculature. The data shown are a combination of both physical measurement of a resin cast and extrapolation for missing branches. The data were reproduced from reference (Horsfield & Gordon, 1981).

unit is a loosly bound volume of small conducting airways and open cavities. Structured much like a foam ("Textbook of respiratory medicine", 2000), the respiratory unit can be visualized as a network of polyhedral surfaces (Aste & Weaire, 2000) that interlock to form a continuum of connected geometric boundaries. There is a branching structure within the terminal respiratory unit. From a terminal bronchiole , 2-5 orders of respiratory bronchioles route air to different parts of the TRU. The respiratory bronchioles lead into a series of smaller channels called alveolar ducts. Numbering in the hundreds, the alveolar ducts further distribute the air throughout the TRU volume. Adjacent to these structures are large numbers (roughly 2000 per TRU) of saccular protrusions called alveoli. Surrounding the terminal respiratory unit is a fine mesh of capillaries that are connected to both arterial and venous trees.

Gas exchange is mediated by the diffusion of oxygen and carbon dioxide through the alveolar surface. Carbon dioxide is brought to the capillary network though the arterial tree. The waste gas diffuses through the alveolar wall into the alveolar cavity. When exhale occurs, CO_2 is carried out of the lung through the bronchial network. At the same

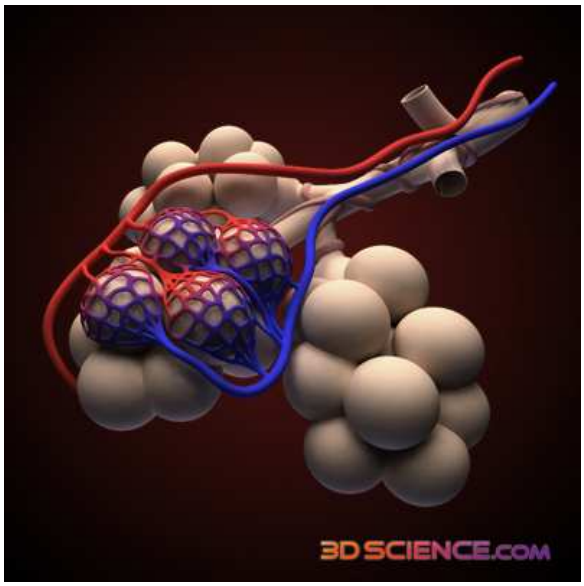

Figure 4.10: A representation of a terminal respiratory unit. The spherical cavities are the alveoli. Within the structure are a series of respiratory conduits and alveolar ducts that transport air to the alveolar volume. An arterial and venous mesh covers the alveolar surface (Courtesy of 3Dscience.com with permission).

time, oxygen is drawn from the alveolar air into the capillary network to be carried back to the heart through the venous system.

4.7 Respiratory mechanics

The process of respiration is carried out through a balanced coordination of different muscle groups throughout the ribcage and abdomen. The driving force behind respiratory motion is the diaphragm. The diaphragm is a large tendon that divides the thoracic and abdominal regions of the torso. Shaped like a truncated, elliptic paraboloid, the diaphragm moves in both the cranial-caudal and ventral-dorsal directions to regulate lung expansion. When the diaphragm contracts, it lowers to create space between itself and the lungs surface. Simultaneous to this, muscles in the chest wall also contract, rotating the ribs outward and upward. This expansion creates a negative pressure differential between the outer lung surface and the atmospheric pressure within the airway system. The lung inflates until a new equilibrium state is reached. During exhale, contraction of the abdominal muscles,

relaxation of the ribcage and recoil of elastic lung tissues squeezes air out of the lung, returning it to its rest volume.

The specific shape of the diaphragm over the respiration cycle was studied by Gauthier (Gauthier, 1994). Using MRI technology, Gauthier imaged the diaphragm of 10 volunteers at four phases of respiration from deep exhale to full inhale. The results, shown in Fig.4.11, illustrate both the shape and motion of the diaphragm during deep breathing maneuvers.

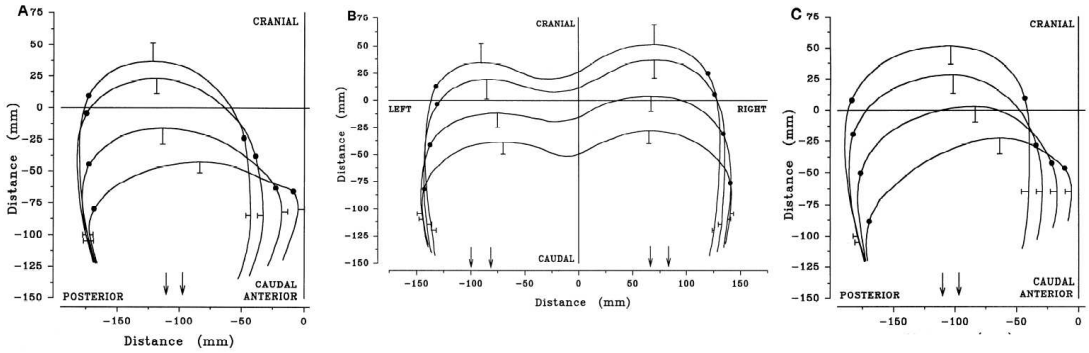

Figure 4.11: Diaphragm shape at various phases of the respiration cycle (Taken from Gauthier (Gauthier, 1994)).

The respiratory motion of the ribcage, diaphragm, and abdomen, can be visualized using the two-compartment model developed by Ward et al. (Ward, Ward, & Macklem, 1992). In the model (see Fig.4.12), the torso is split into ribcage and abdominal components by the diaphragm, which is represented as a piston, driven by two muscles . During inspiratory maneuvers, the ribcage hinges up and out while the diaphragm portion moves laterally outward creating the greatest possible expansion of the chest cavity. The natural recoil of the tissues and resistance due to static or incompressible structures is simulated by springs located at various points within the model frame.

4.8 Spirometry of the lung

Lung volume is often used as an indicator in the diagnosis of disease in patients with suspected pulmonary conditions. Through the use of a spirometer, a precise differential pressure transducer, physicians measure a patient's lung volume and volume differences at specific points throughout the breathing cycle. This process, known as spirometry,

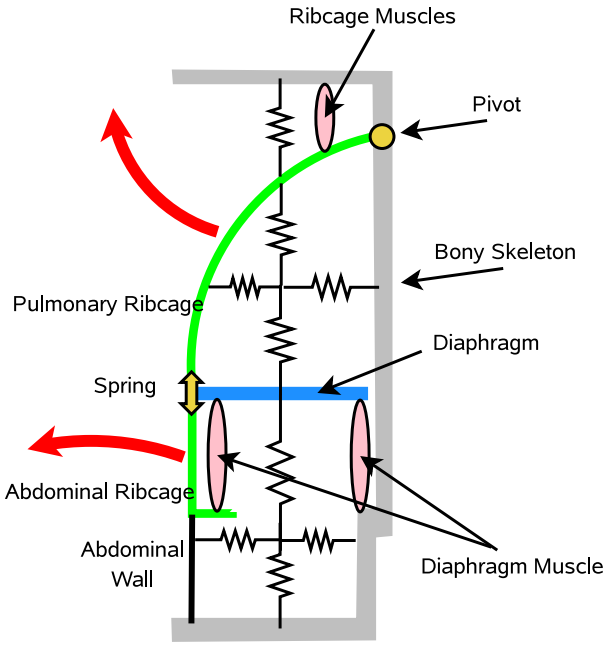

Figure 4.12: The two compartment model of the lung: In the figure, the chestwall pivots up and out from the base of the neck. This motion is driven by the ribcage muscles and the diaphragm. The diaphragm also drives the motion of the abdominal ribcage outward. The internal resistance of the body tissues is represented by springs (resistor symbols). The motion of the diaphragm is represented by the yellow arrow.

yields valuable information that the physician can use to identify illness. The practice of spirometry has produced a lot of data on lung volume. The following list along with Fig.4.13 defines the terminology used in the spirometry field.

- Expiratory Reserve Volume (**ERV**): volume change between normal exhale and full exhale.
- Functional Residual Capacity (**FRC**): volume after normal exhale.
- Inspiratory Capacity (**IC**): volume change between normal exhale and full inhale.
- Inspiratory Reserve Volume (**IRV**): volume change between normal inhale and full inhale.
- Reserve Volume (**RV**): the volume after full exhale.

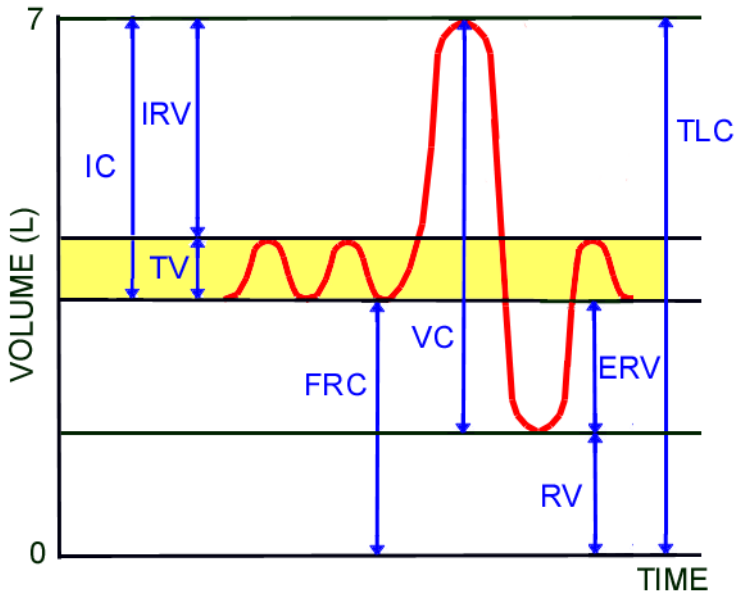

Figure 4.13: Nomenclature conventions of lung volume throughout the breathing cycle.

- Total Lung Capacity (**TLC**): the volume after full inhale.
- Tidal Volume (**TV**): the volume change between normal inhale and normal. exhale.
- Vital Capacity (**VC**): the volume change between full inhale and full exhale.

There is much variation in these volumes depending on a subject's age, height, sex, stature and ethnicity. To deal with this fact, there are formulaic and scaling methods used to deduce the proper normal values for a given group. Table 4.3 shows a sampling of reference values for RV, TLC, FRC and TV obtained from various sources. The American Thoracic Society's (ATS)(American Thoracic Society, 1991) published values are formula based and represent estimates for a non-smoking caucasian male 1.75 m in height and age 45 yrs and a caucasian female of 1.65 m and 45 yrs. The European Respirology Society's (ERS)(Stocks & Quanjer, 1995) published values are also formula based and represent the same patient info as the ATS values with the exception that the sampled population contains current and former smokers. The data used by Gauthier (Gauthier, 1994) was

Table 4.3: Published values of lung volume at reserve volume, functional residual capacity and total lung capacity.

Phase of Resp	Volume [L]		Reference
	Male	Female	
RV	2.05	1.89	ATS
	1.89±0.27	1.62±0.18	ERS
	1.55±0.11	-	Gauthier
FRC	3.46	2.97	ATS
	2.66±0.18	-	Gauthier
TLC	6.90	5.76	ATS
	6.6±0.25	5.12±0.13	ERS
	6.84±0.28	-	Gauthier
TV	~ 0.5		TRM

from a set of 4 non-smoking male patients with a height range of 1.79±0.04 m and age 38.2±2.7 years. An estimate of tidal volume was given in Reference ("Textbook of respiratory medicine", 2000), *The Textbook of Respiratory Medicine* (TRM), but no population sampling data could be found. Needless to say, these value are not representative of an entire population but for the purposes of this work are adequate as a general guide.

CHAPTER 5

MONTE CARLO MODELS OF THE LUNG

5.1 Introduction

This chapter describes the creation of Monte Carlo based models of the lung. Two models will be presented here. The first lung model, called TISSUE (see right hand portion of Fig.5.1) represents the connective tissues of the lung described in sections 4.3 and 4.6 of the previous chapter. The second model, called BRANCH (see left hand portion of Fig.5.1), consists of geometric representations of the bronchial, arterial and venous branching networks of the right lung described in sections 4.4 and 4.5. The branching networks are enclosed within a representation of the lung's outer boundary. The boundary may be modified to represent the shape, volume and density of the lung at any phase of the respiration cycle. The BRANCH model work presented in this thesis has been subsequently published in Medical Physics (Babcock & Sidhu, 2010a, 2010b)

As mentioned in Chapter 2, an EGSnrc Monte Carlo code requires user defined geometric and output subroutines. In developing Monte Carlo models of the lung, it was decided that a modification of DOSXYZnrc was the best approach. DOSXYZnrc contains many features required for simulation within the lung models. The two most important features were: (1) the use of a BEAMnrc created phase space source and (2) the scoring of dose to a 3D voxelated grid. The only deficiency in DOSXYZnrc was its voxelated representation of the treatment environment. In principle, one could resolve the fine structures of the lung by defining a sufficiently small voxel size. However, as voxel size is decreased, the number of voxels required to represent an equal volume increases. Unfortunately, the physical memory of the computer places an upper limit on the number of voxels that can be defined. The structures of the lung could not be sufficiently resolved

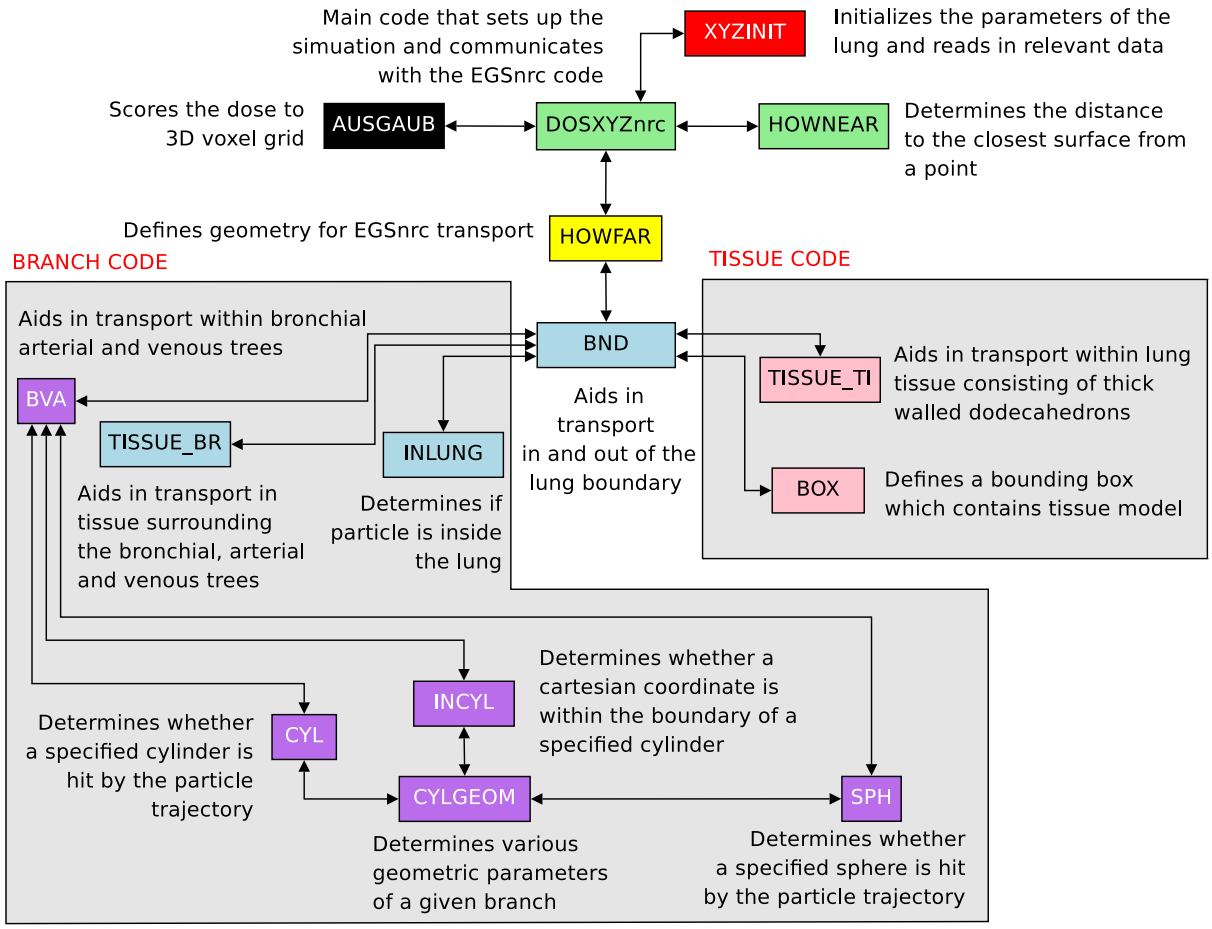

Figure 5.1: The lung model algorithms: Two lung models were created for Monte Carlo simulation. The first model is TISSUE which defines the geometries of the connective alveolar tissues of the lung. The second model is BRANCH which defines the geometries of the bronchial arterial and venous networks.

within this limit. Therefore, a modification to DOSXYZnrc which allowed for the inclusion of non-voxelated geometries (to define the lung geometry) was needed (Babcock, Cranmer-Sargison, & Sidhu, 2008).

DOSXYZnrc was expanded to handle transport and scoring within the nonvoxelated boundaries of the lung models. The proceeding sections describe the expanded code as well as the various lung model components. For each model, a comparison to relevant anatomic and physiologic measurements will be made.

5.2 Modifications to DOSXYZnrc

DOSXYZnrc is designed to transport particles within a voxelated cartesian geometry. Since lung geometries are inherently non-cartesian, a method was needed that allowed for the inclusion of any geometry into a DOSXYZnrc simulation while still scoring to a voxelated grid. The separation of the scoring grid from the phantom geometry has been done, in part, by a new feature of DOSXYZnrc designated HOWFARLESS (B. Walters & Kawrakow, 2007). HOWFARLESS removes the voxel boundary restrictions for simple homogeneous phantoms. In HOWFARLESS, the phantom geometry is defined by the outer boundaries of the voxel grid. During particle transport, individual voxel boundaries are not checked. When an energy depositing event occurs, the position of the interaction is converted to a voxel position in the scoring grid. Another user code called DOSSCORE (De Smedt, Reynaert, Nerve, & Thierens, 2004) uses two independent voxelated grids for scoring and transport. Particle transport is carried out on the geometric grid. When energy is deposited, the interaction position in the geometric grid is converted to the position in the scoring grid. Neither HOWFARLESS nor DOSSCORE allow for the inclusion of non-cartesian representations of the transport environment. A new method was needed to incorporate non-cartesian geometries into the DOSXYZnrc transport routine.

The voxelated geometry of DOSXYZnrc consists of `irmax+1` separate regions. This includes the ($\mathtt{i}_{\mathtt{max}} \times \mathtt{j}_{\mathtt{max}} \times \mathtt{k}_{\mathtt{max}}$) regions representing the voxel grid plus two regions used to represent the volume surrounding the voxel geometry and the region where particle transport originates/terminates. In the non-voxelated code, regions greater than `irmax+1`

were needed. To include additional regions, the DOSXYZnrc variable, $MXREG, was increased from irmax+2 to irmax+20 in the macro file dosxyznrc_user_macros.mortran

Two new subroutines, XYZINIT and BOUNDARY, were added to the DOSXYZnrc code. These routines interact with the original code to facilitate non-voxelated particle transport. The following sections outline the function of these routines, as well as, the changes made to the scoring routine, AUSGAB and the electron transport routine HOWNEAR.

5.2.1 XYZINIT: initialization of lung transport

To set up non-voxelated particle transport, it was necessary to initialize several new parameters. These parameters were defined in a new input file called xyzinit. The xyzinit parameters were needed to determine:

1. whether non-voxelated geometries were requested
2. how many non-voxelated regions were in the simulation
3. the composition and density of each non-voxelated region

The input file xyzinit is read by a subroutine of the same name. The call to the subroutine XYZINIT is made one time in the initialization portion of the original DOSXYZnrc code.

5.2.2 BOUNDARY: transport independent of the voxel grid

Conventionally, DOSXYZnrc transports a particle through a geometric voxelated grid on a voxel by voxel basis. Each voxel represents a unique region or geometric boundary with a user defined atomic composition and density. To handle non-voxelated transport, a new subroutine called BOUNDARY was created. The BOUNDARY algorithm serves very much the same function as a general HOWFAR subroutine in an EGSnrc user code. It checks for a distance-to-intercept (DTI) with the surfaces that define the non-voxelated geometries. An auxiliary function of BOUNDARY was to mediate particle transport into and out of the non-voxelated regions.

5.2.3 AUSGAB: separating the geometric and scoring voxel grids

Each voxel in DOSXYZnrc represents a separate region in cartesian space. The scoring routine, AUSGAB, is designed to keep a running total of absorbed energy in each voxel. For both lung models, the absorbed energy is the sum of absorbed energy to all geometric regions (including regions containing air). At the end of a simulation, this information is converted into dose by dividing the absorbed energy by the mean mass of the voxel. Once the absorbed dose array is calculated, it is written to a 3ddose file.

DOSXYZnrc defines a region in one of two ways. The first is the position in the voxel grid ($\mathtt{ir_x}$, $\mathtt{ir_y}$, $\mathtt{ir_z}$). For example, one can define a region as 5 voxels in the x direction, 2 voxels in the y direction and 10 voxels in the z direction from the origin. The second definition is the region index (ir) which is related to voxel position by the following equation:

$$\mathtt{ir} = 1 + \mathtt{ir_x} + ((\mathtt{ir_y} - 1) + (\mathtt{ir_z} - 1) \cdot \mathtt{j_{max}}) \cdot \mathtt{i_{max}}. \tag{5.1}$$

By defining a region in this way, a single region index contains information about particle position in three dimensional space. In AUSGAB, the region index is used to encode the position of energy deposition. For non-voxelated transport however, the region index does not correspond to a position in the voxel grid. To score dose within non-voxelated regions, AUSGAB required modification. When energy is deposited within a non-voxelated geometry, AUSGAB now searches the boundaries of the voxel grid to determine which voxel element contains the event. When the grid position is found, the information is converted into a region index through Eq.5.1. This region index is used to assign the deposited energy to the appropriate position in the voxel grid.

Within the original implementation of DOSXYZnrc, an electron undergoing a condensed history event deposits its energy at the endpoint of its path as opposed to along the entire pathlength. This is reasonable as a condensed step is limited by the voxel boundary. Since the pathlength of the electron is contained by the voxel, all energy deposited is still properly scored to the voxel. For non-voxelated transport, this boundary limitation is removed. This can result in a significant miscalculation of dose. Essentially, energy that should have been deposited over many voxels is deposited in the voxel containing the

endpoint of the path. The solution to this problem already existed within the AUSGAB implementation of HOWFARLESS. The NRC group, who developed the HOWFARLESS code, introduced a hinge step approach for condensed history electrons. The hinge step approximation uses two vectors attached by a hinge point to represent the curved pathlength of the electron. Energy deposited in a condensed history step is distributed along the hinged pathlength to ensure proper energy deposition within the phantom. The HOWFARLESS implementation of condensed history energy deposition was incorporated into the non-voxelated scoring routine. Essentially, transport within each region can be thought of as a HOWFARLESS simulation where the region boundary replaces the normal outer phantom boundary. When a particle exits a region and enters a new one, HOWFARLESS transport is reinitialized.

5.2.4 HOWNEAR: condensed history transport of charged particles

To allow condensed history electron transport, the HOWNEAR subroutine is used to determine the perpendicular distance to the closest boundary. For a conventional DOSXYZnrc simulation, only the six voxel boundaries are checked. In principle, HOWNEAR could be expanded to include the geometric surfaces that define the lung model. However, since the number of geometric surfaces in the lung models was large, condensed history transport was turned off. Consequently, electron transport was carried out in single scatter mode for all simulations. However, if one uses the non-voxelated DOSXYZnrc code with a HOWNEAR routine (which was the case for voxel regions outside the boundaries of the lung models), the condensed history HOWFARLESS method is used.

5.3 The TISSUE model

To simulate particle transport within the porous connective tissues of the lung, the TISSUE model was created. The TISSUE geometry was made to represent the smallest connective tissue structure in the lung: the alveoli. As was discused in Chapter 4, the alveoli are walled polyhedral cavities of air that fit together to form the respiratory portion of the lung. For the TISSUE model, it was not practical to reproduce the irregular patterns

of polyhedral shapes throughout the lung volume. However, alveolar transport may be approximated by assuring that a particle encountered the correct proportion and spacing of alveolar components (i.e. tissue and air) along its path. This was accomplished by modeling the alveoli as a continuous chain of dodecahedron shells (see Fig.5.2).

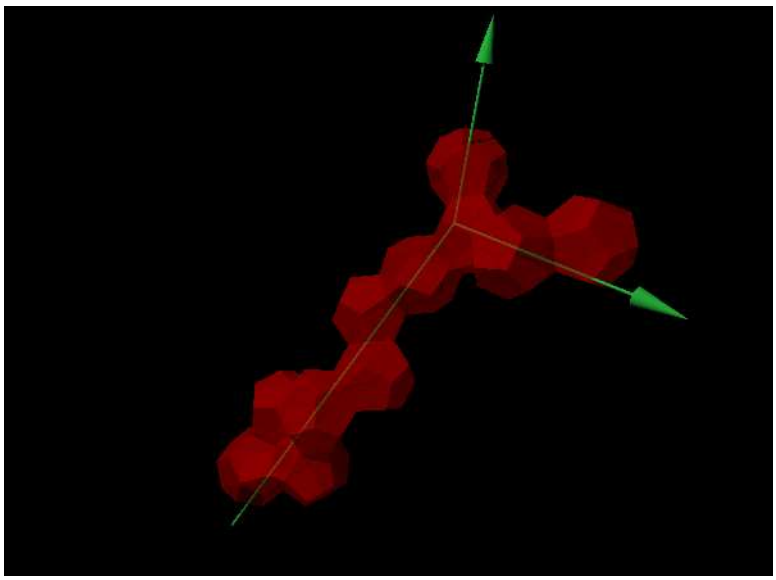

Figure 5.2: Transport within the TISSUE model: As a particle travels, it "walks" along a continuous path of dodecahedrons. When a particle leaves a dodecahedron, a new dodecahedron is created. The normal of the new dodecahedron surface being entered is aligned with the direction vector of the particle.

5.3.1 The simulation setup

The TISSUE model was set up as a two slab geometry (illustrated in Fig.5.3). The slab geometry was divided into an 80 x 80 x 80 element voxel grid with each voxel having a dimension of 0.25 cm x 0.25 cm x 0.25 cm. The first slab layer was modeled as water. This water layer, which was 3.0 cm thick, represented the tissues of the chest wall that surround the lung. Within this layer, conventional voxelated transport was used (i.e. the voxel grid was used to define both the geometry and scoring regions of the simulation). The second slab layer, which was 17.0 cm thick, represented the lung tissue. In the lung layer, particle transport was performed in the non-voxelated dodecahedron regions of the TISSUE model (i.e. the voxel grid was only used for scoring dose). The particle source, a

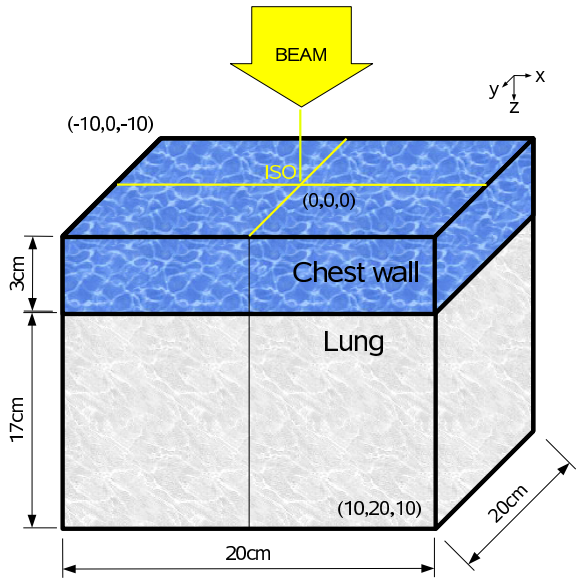

Figure 5.3: The TISSUE simulation setup.

clinical 6 MV x-ray beam (see Section 3.2) with an SSD of 100 cm, was placed incident on the origin, perpendicular to a slab plane. The upper and lower corners of the grid were located at (-10 cm ,-10 cm , 0 cm) and (10 cm ,10 cm ,20 cm) respectively.

For the water slab, simulations were run using the PRESTA-II condensed history electron transport and the EXACT boundary crossing algorithm. To allow for condensed history transport in the lung slab, a HOWNEAR routine was written for the dodecahedrons of the TISSUE model. However, it was found that simulation time was not improved when condensed history was performed. Therefore, electron transport in the dodecahedron regions of the lung slab was performed in single scatter mode. The EXACT boundary crossing algorithm was used for the dodecahedron geometries. The ECUT and PCUT parameters were set to 0.7 and 0.01 MeV respectively. All MC transport parameters were left at their recommended (default) values. No variance reduction techniques were used. A 16 node cluster consisting of four 2.0 GHz Opteron 270 processors and one 2.2 GHz AMD Phenom 9500 was used to perform the Monte Carlo calculations. Each node had 1 Gb of memory.

Three TISSUE models were created corresponding to three different phases of lung respiration (reserve volume, functional capacity and total lung capacity). For simulations

using the DOSXYZnrc Monte Carlo and Pinnacle^3 CCC methods five field sizes were simulated: 1x1, 3x3, 5x5, 7x7 and 10x10 cm^2. Due to long simulation times, only the 1x1, 3x3, 5x5 cm^2 were simulated using the TISSUE model.

5.3.2 Region composition and density

There are two region indices assigned in the TISSUE model. The first region corresponds to the air cavity of an alveolar unit. The second regions corresponds to the alveolar wall. Each region in TISSUE was assigned a material and density from the PEGS4 file 700icru.pegs4dat which was included with the EGS distribution. The PEGS4 material AIR700ICRU (air) with a density of 1.205×10^{-3} g/cm^3 was assigned to the air cavity. The PEGS4 material H2O700ICRU (water) with a density of 1.000 g/cm^3 was assigned to the alveolar wall.

5.3.3 The TISSUE model outer boundary

To handle transport inside and outside the boundaries of the lung tissue slab, the subroutine BOX was created. Within BOX, the distance-to-intercept to the six planes of the lung slab surface was calculated. When a particle trajectory crossed the lung slab boundary before the next interaction site, the particle step size and region index were updated. When a particle crossed the lung slab boundary from outside, the region was updated to air (representative of an alveolar air cavity). If a particle crossed the lung slab boundary from the inside, the region index was updated to water (the chest wall).

5.3.4 The dodecahedron model of the alveoli

A regular dodecahedron (a 12 sided polyhedron with identical faces) was used to represent the general shape of individual alveoli in the TISSUE model. Ideally, the 14 sided tetrakaidecahedron would have been used as it is the most common shape within polyhedral structures such as lung tissue (Aste & Weaire, 2000). However, due to it's easy to define geometry, the dodecahedron served as an adequate substitute.

A regular dodecahedron (see Fig.5.4) is defined by the intersection of twelve planes.

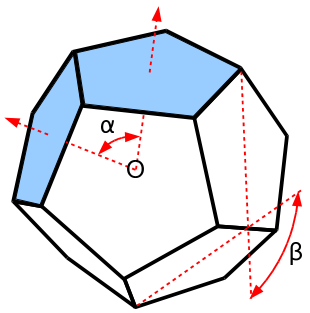

Figure 5.4: A regular dodecahedron is defined by twelve pentagonal planes joined together. The angle between the normal of two adjacent planes (α) is 63.43°. The angle where two faces of a polyhedron connect is called the dihedral angle (β). For a dodecahedron, the dihedral angle is 116.57°. Each pentagonal plane is equidistant from the origin.

Each plane is pentagonal, equal in area and equidistant from the center of the dodecahedron volume. The angle between two adjacent normal vectors is 63.43°. The angle between any two adjacent planes (the dihedral angle) is 116.57°. The volume of a dodecahedron (Weisstein, 2009) is:

$$V = \frac{1}{4}\left(15+7\sqrt{5}\right)\left(\frac{1}{2}\cot\frac{\gamma}{2}\cdot\cot\frac{\beta}{2}\right)^3 D^3 \tag{5.2}$$

where γ is the angle of a perfect pentagon (108°), β is the dihedral angle and D is the distance from the dodecahedron center to a dodecahedron plane along its perpendicular.

A dodecahedron model of the alveoli was defined by two dodecahedron surfaces that characterized a dodecahedron shell. The two dodecahedron surfaces defined two regions: an inner dodecahedron cavity (alveolar air) and an outer dodecahedron shell (alveolar wall). The model dodecahedron shell was parameterized by: (1) an orthogonal basis that defined the orientation of the dodecahedron, (2) a point that defined the center of the dodecahedron, (3) two lengths that defined the perpendicular distances from the dodecahedron center to the inner and outer planes of the wall and (4) twelve unit vectors that define the normal of the twelve dodecahedron planes. In the TISSUE code, new dodecahedron geometries were constructed as needed along a particle's path. It should be noted here that the constructed dodecahedrons were discarded once used (i.e. they did not cumulatively fill the model volume). As a result, the TISSUE model is not completely physical. Two

particles can pass through the same region and encounter differently orientated dodecahedrons. However, it is not possibly to completely fill a volume with a single repeating polyhedral structure. Although the TISSUE model is not completely physical, it still creates a transport environment where a particle encounters the proper proportion of tissue (wall) and air (cavity).

During transport, a particle is transported into a dodecahedron shell, through a dodecahedron air cavity and out through the same dodecahedron shell. When a particle exits a dodecahedron, a new dodecahedron is defined that connects to the previous dodecahedron at the surface of particle exit. If a particle changes direction due to an interaction, the new dodecahedron is re-orientated to put the orthogonal basis along the particle direction. This ensures that a particle will see the same proportion of air and tissue regardless of its direction. This process is repeated until the particle exits the lung tissue region.

Several papers have quoted the alveolar cavity diameter to be approximately 200 μm (Weibel, 1963; Hansen & Ampaya, 1975; Kitaoka, Tamura, & Takaki, 2002). The thickness of the alveolar wall is on the order of 5-10 μm. However, lung tissue is not comprised solely of alveolar tissue. Other tissues such as capillary blood and lymphatics contribute to overall lung tissue density. If one were to use the quoted values for cavity diameter and alveolar wall thickness, the attenuating properties of the model tissue would be much lower than that observed in real lung tissue. As a first approximation, the dodecahedron wall thickness was increased to account for these non-alveolar tissues. By doing so, it was possible to create a TISSUE model with attenuating properties that were consistent with measurement.

The x-ray attenuation of lung tissue can be broken up into air (alveolar cavity) and tissue (alveolar wall) components:

$$\frac{N}{N_0} = exp\left[-\frac{\mu_L}{\rho}(x_T + x_A)\rho_L\right] = exp\left[-\frac{\mu_T}{\rho}\rho_T x_T - \frac{\mu_A}{\rho}\rho_A x_A\right]. \tag{5.3}$$

In Eq.5.3, N/N_0 represents the fractional number of incident particles that are attenuated by lung tissue, x_T and x_A represent the thicknesses of alveolar tissues and air cavities subtended along a particle path and the μ/ρ variables represent the attenuation coefficients of lung (L), tissue (T) and air (A) (see Table 5.1). Solving for wall thickness, the preceeding

equation becomes:

$$x_T = \frac{(\frac{\mu_L}{\rho}\rho_L - \frac{\mu_A}{\rho}\rho_A)}{(\frac{\mu_T}{\rho}\rho_T - \frac{\mu_L}{\rho}\rho_L)} x_A. \tag{5.4}$$

By assigning an anatomically realistic value to x_A and the desired lung density ρ_L, an alve-

Table 5.1: X-ray attenuation coefficients for air,water and lung over a range of x-ray energies (Taken from ICRU report 44 (*ICRU Report 44 : Tissue Substitutes in Radiation Dosimetry and Measurement*, 1989)). The final column calculates the value of x_T/x_A from Eq.5.4. It can be seen that x_T/x_A is nearly constant over the range of energies.

Energy (MeV)	Mass Attenuation (m^2kg^{-1})			
	μ_L/ρ	μ_T/ρ	μ_A/ρ	x_T/x_A
0.100	1.70E-02	1.71E-02	1.54E-02	0.658
0.200	1.36E-02	1.37E-02	1.23E-02	0.657
0.300	1.18E-02	1.19E-02	1.07E-02	0.656
0.400	1.05E-02	1.06E-02	9.55E-03	0.654
0.500	9.61E-03	9.69E-03	8.71E-03	0.656
0.600	8.88E-03	8.96E-03	8.06E-03	0.655
0.800	7.80E-03	7.87E-03	7.07E-03	0.655
1.000	7.01E-03	7.07E-03	6.36E-03	0.655
1.500	5.71E-03	5.75E-03	5.17E-03	0.657
2.000	4.90E-03	4.94E-03	4.45E-03	0.656
3.000	3.94E-03	3.97E-03	3.58E-03	0.657
4.000	3.37E-03	3.40E-03	3.08E-03	0.655
5.000	3.00E-03	3.03E-03	2.75E-03	0.654
6.000	2.75E-03	2.77E-03	2.52E-03	0.657
			AVG:	0.656

olar wall thickness was calculated. The resulting TISSUE model retained the attenuation properties of real lung tissue.

To create a reserve volume TISSUE model, the x_A and ρ_L parameters were set at 200 μm and 0.400 g/cm^3 respectively. Although the lung density value was rather high for reserve volume, it was chosen because it matched well with the upper lung density limit in our institution's treatment planning system (see Table 5.6 for the treatment planning system density-to-CT ramp). The volume of the lung (V_L) was set at 2.5 L. The alveolar wall thickness was calculated from Eq.5.4 for energies ranging from 0.100-6.00 MeV (see Table 5.1). It was found that regardless of energy, the wall thickness was very close to 131 μm.

To construct dodecahedron models at other phases of respiration, two conditions had to be met: (1) lung mass had to be conserved (i.e. $m = \rho_L \cdot V_L = \text{constant}$) and (2) for two phases of respiration, the ratio of lung volumes had to equal the ratio of dodecahedron air cavity volumes. From these two conditions, dodecahedron models were constructed for three other phases of respiration: reserve volume, functional capacity and total lung capacity corresponding to densities of 0.300, 0.200 and 0.125 g/cm^3 respectively. Table 5.2 shows the summary of model parameters at four lung volumes. For TISSUE simulations, only the last three models in the table were used.

Table 5.2: Dimensions of the TISSUE model dodecahedron cell at four phases of respiration.

Volume (L)	ρ_L (g/cm^3)	x_A (μm)	x_T (μm)
2.5	0.400	200	131
3.3	0.300	219	92
5.0	0.200	252	62
8.0	0.125	295	41

5.3.5 The TISSUE code logic

The majority of the TISSUE algorithm (illustrated in Fig.5.5) is executed within the BOUNDARY subroutine. First, BOUNDARY determines the region of the current particle. If the particle region corresponds to the chest wall, the subroutine BOX is called and

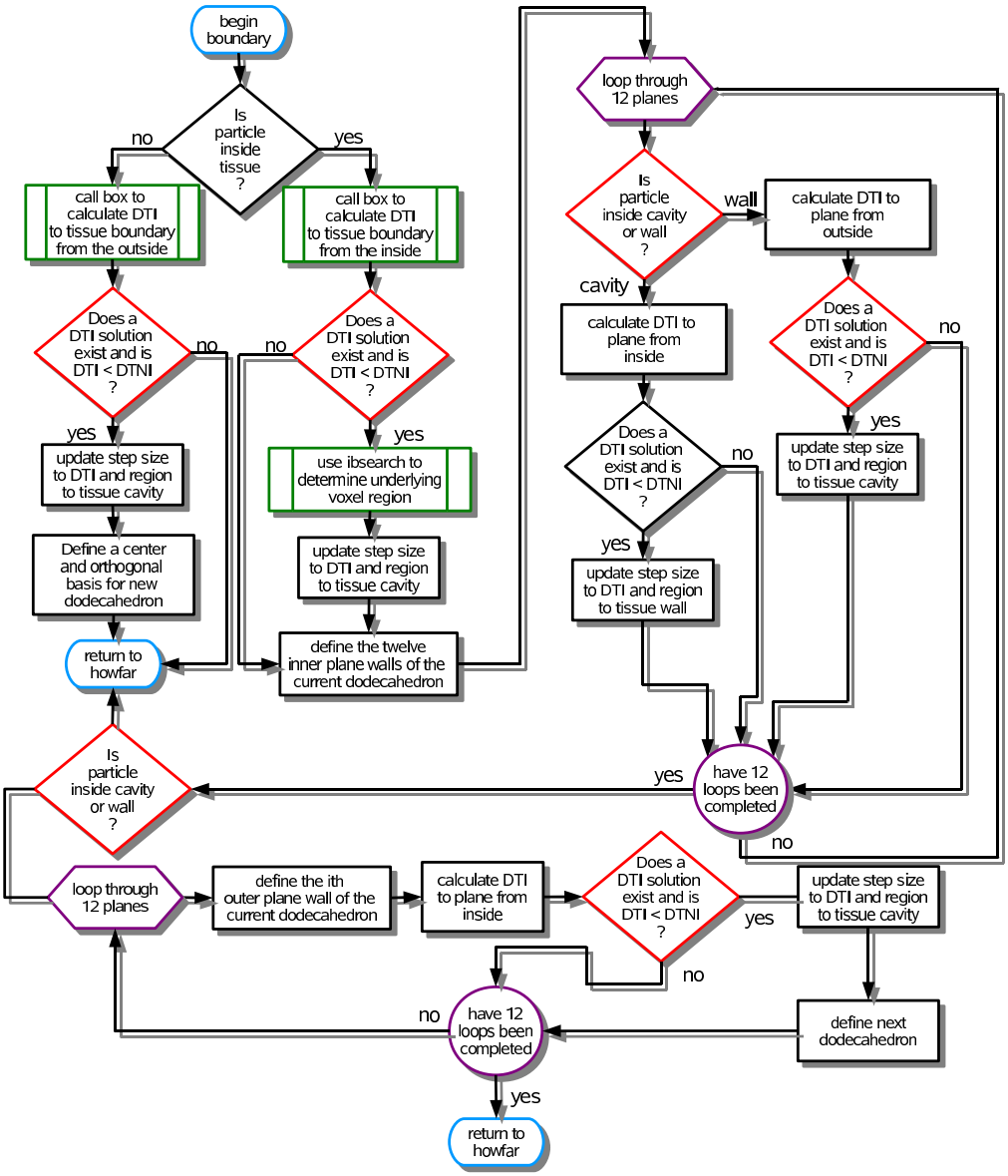

Figure 5.5: The TISSUE model algorithm.

the DTI to the lung tissue slab boundary is calculated from the outside. If the DTI is closer than the distance to the next interaction (DTNI), the particle is transported to the boundary and the particle region is updated to alveolar air. A dodecahedron is created which is centered at the intercept position on the bounding box. A dodecahedron orthogonal basis is defined with one axis parallel to the particle trajectory. The dodecahedron parameters are stored as global variables and BOUNDARY is terminated.

If a particle region corresponds to lung tissue, BOX is called to calculate the DTI to the lung tissue slab boundary from the inside. Again, if the DTI is closer than the DTNI, the particle step size is updated to intercept the boundary surface. The underlying voxel region is calculated and the region index is then updated. Once the DTI to the bounding box has been determined, BOUNDARY calculates the DTI for the surfaces of the current dodecahedron.

For a particle within the air cavity region, the DTIs to the twelve planes that define the inner alveolar wall are calculated. If the smallest of the twelve DTIs is less than the DTNI, the step size is updated and the region changed to the alveolar wall. If a particle region corresponds to the alveolar wall region, the DTIs to the twelve planes of the inner alveolar wall are checked from the outside. If the DTI is less than the DTNI and the surface intercept point is inside[3] the remaining eleven planes, the region index is updated to the air cavity region. After the inner wall surfaces have been checked, the DTIs to the twelve planes of the outer wall surface are calculated. Again, if the smallest DTI is less than the DTNI, the step size is updated. The region is updated to the air cavity and the next dodecahedron is defined.

5.3.6 Verifying the TISSUE code

To verify the TISSUE code, the position, direction, region and step size of several particle histories were examined. It was clear that particle transport was properly contained to the boundaries of the dodecahedron model. An all-water simulation was performed using the TISSUE model. A 3x3 cm^2 field was placed incident on the all-water phantom.

[3]the inside and outside of a plane is defined by its normal vector. If the normal points into the region of a particle, the particle is outside the plane surface

A homogeneous, voxelated, DOSXYZnrc phantom was simulated under the same setup conditions. A comparison of depth dose curves and crossplane/inplane profiles for the two simulations showed good agreement (see Figs.5.6 and 5.7). Along the central axis, the percent difference between the two distributions was within 1% for the majority of points. The outliers, which were between 1 and 2%, were a result of incomplete convergence of the simulations. This was unavoidable due to the long simulation times (5-10 days per simulation to achieve the statistics presented here). Gamma analysis of the crossplane and inplane profiles showed the majority of points were within a position tolerance of 0.1 cm and a percent different tolerance of 1%. There were a few outliers in the plateau portions of the profiles which had a percent differences upwards of 1.2%. The χ^2 difference between the two distributions was 0.34 which indicates that the two distributions match.

5.4 The BRANCH model

As mentioned in the introduction, the BRANCH model consists of the right bronchial, arterial and venous networks surrounded by a representation of the right lung boundary. The outer boundary of the BRANCH model was represented by set of polynomial surfaces of order four and lower (i.e. quartic, cubic, quadric and planar surfaces). A quartic polynomial surface is defined as:

$$P(\vec{x}) = \sum_{i_1}^{3}\sum_{i_2}^{3}\ldots\sum_{i_4}^{3} n_{i_1 i_2 \ldots i_4}(x_{i_1} - \delta x_{i_1})(x_{i_2} - \delta x_{i_2})\ldots(x_{i_4} - \delta x_{i_4}) = 0 \qquad (5.5)$$

where $\vec{x} = \{x_1, x_2, x_3\}$ represents a point in cartesian space, $\vec{\delta x} = \{\delta x_1, \delta x_2, \delta x_3\}$ is a translation component, $n_{i_1 i_2 \ldots i_4}$ are arbitrary constants and $i_1, i_2, \ldots i_n$ are integers between 1 and 3. The choice of the polynomial form was twofold. First, the DTI solution for the quadric subset of surfaces has been well documented (Bielajew, 1995). Second, polynomial surfaces yield a wide variety of shapes under a single formalism. By adjusting the $n_{i_1 i_2 \ldots i_4}$ values, one can define a multitude of geometric shapes including common second order (quadric) polynomials such as spheres, ellipsoids, paraboloids, cylinders and hyperboloids.

The bronchial, venous and arterial branching networks were represented by a series

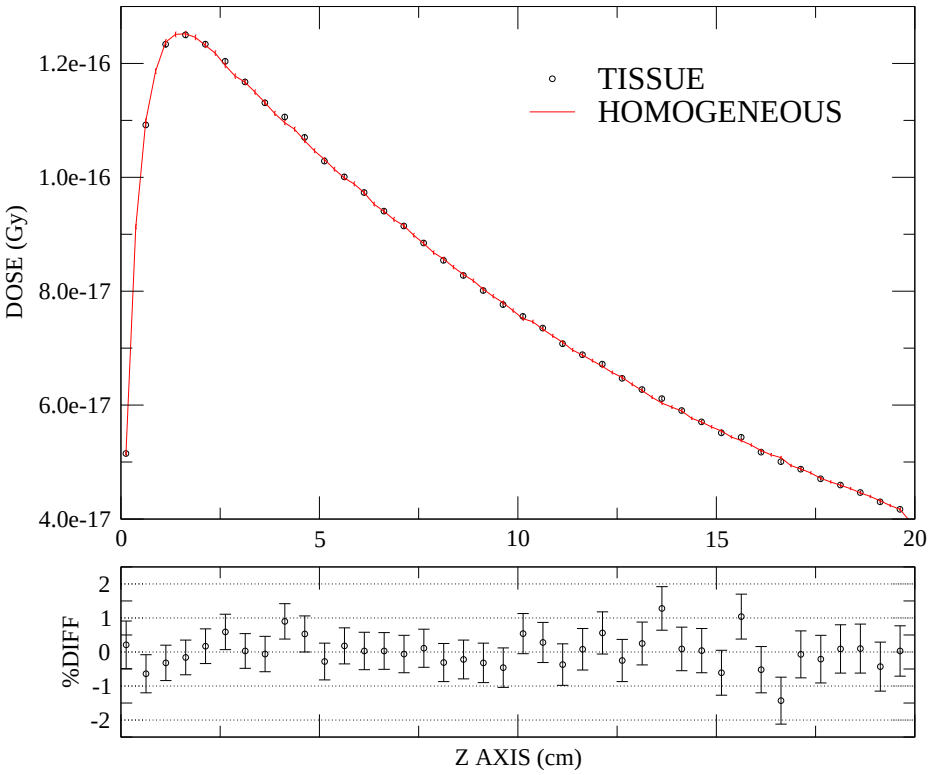

Figure 5.6: Comparison of all-water TISSUE simulation and the voxelated homogeneous DOSXYZnrc simulation depth dose curves: In the bottom figure, the percent difference between the two simulations is presented. The uncertainty in dose values is roughly 0.5%.

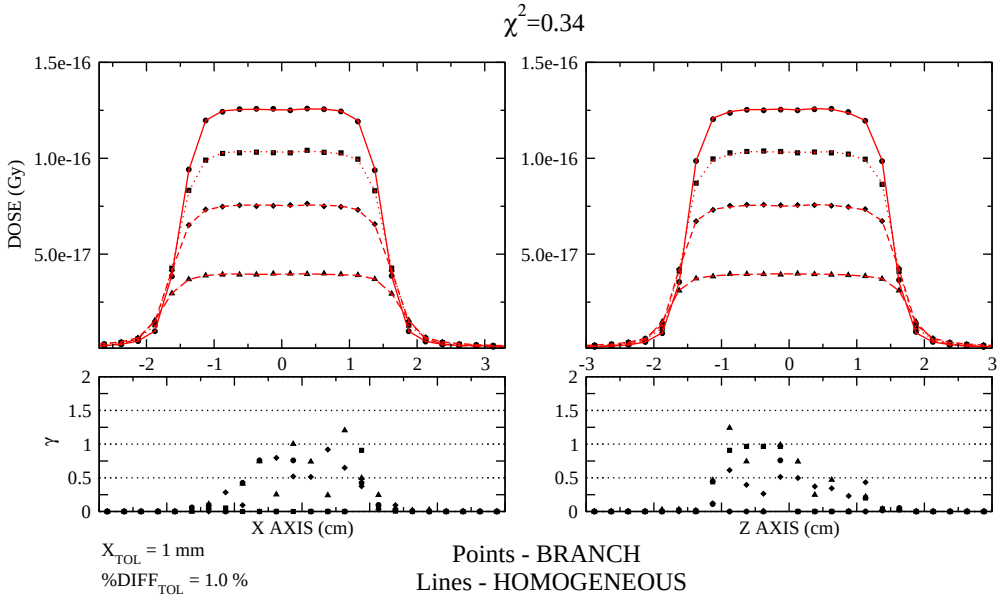

Figure 5.7: Comparison of all-water TISSUE simulation and the voxelated homogeneous DOSXYZnrc simulation crossplane/inplane profiles: In the top two figures are the crossplane and inplane profiles at depths of 1.6, 5.0, 10.0 and 20.0 cm along the beam (z) axis. The bottom two figures show the value of the γ function for each profile. The positional and dose percent difference tolerances were set at 0.1 cm and 1.0% respectively.

of overlapping cylinders and spheres, as shown in Fig.5.8. Each cylinder represents a branch while a sphere acts as a junction point between adjacent branches. To include both

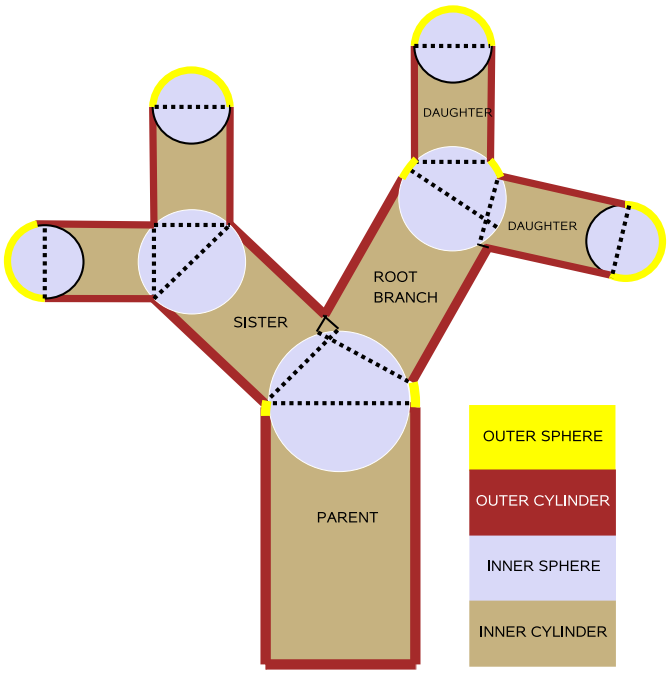

Figure 5.8: Geometric representation of the bronchial branch geometry: Each branch in the bronchial network is simulated as a cylindrical shell of specified length and inner/outer radius. At any point where two or more branches meet, a spherical shell acts as a junction to form a continuous network of branches.

a bronchial wall and bronchial airway in the BRANCH model, the bronchial tree was represented by series of thick walled cylindrical and spherical shells. The inner portion of the cylindrical shell was simulated as air. The composition of the shell wall was dependent on the outer radius of the cylinder. If the radius was below the threshold of 0.5 cm, the cylinder wall was simulated as tissue. These branches were representative of the bronchioles. If the radius was above the threshold, the cylinder wall was simulated as cartilage. These branches were representative of the bronchi. The venous and arterial branching networks were modeled as a series of solid cylinders and spheres. The blood within the arterial/venous branches was assumed to be dosimetrically identical to the containing walls. The

solution of the DTI for all geometric surfaces is outlined in Appendix A.

5.4.1 The simulation setup

The simulation setup for the BRANCH model is illustrated in Fig.5.9. For all BRANCH simulations, the source beam was incident along the y (anterior-posterior) axis in the negative direction. The beam isocenter was located at (-5.0 cm, 1.0 cm, -7.0 cm) which was the approximate center of the lung volume. Three BRANCH models were created each corresponding to a specific phase of respiration: (1) reserve volume, (2) functional capacity and (3) total lung capacity. For each model, the lung boundary parameters were adjusted to produce the appropriate lung volume and dimension as discussed in Section 5.4.6. For the three respiration phases, the tissue densities were set at 0.300, 0.200 and 0.125 g/cm^3 respectively. A voxel grid was superimposed over each model. The voxel grid for the exhale model contained 110 x 160 x 80 voxels. For the midbreath and inhale models, the voxel grid contained 160 x 180 x 120 voxels. The change in voxel grid size was needed to properly cover the increased volume occupied by the inhale and midbreath models. The lower and upper corners of the exhale model were defined at (x0, y0, z0) = (-10.5 cm, -8.0 cm, -18 cm) and (x1, y1, z1) = (0.5 cm, 8.0 cm, -2.0 cm). For the midbreath and inhale models the corners were defined at (x0, y0, z0) = (-14 cm, -10 cm, -18 cm) and (x1, y1, z1) = (2 cm, 8 cm, 6 cm). The voxel size within the grid was set at 0.1cm x 0.1cm x 0.2 cm for all three models. A total of 9 BRANCH simulations were run. For each of the three BRANCH models, three field sizes were simulated: 1x1, 3x3, and 5x5 cm^2.

During initial testing of the BRANCH model, it was found that simulating the entire lung model produced unfavorably long simulation run times. To decrease simulation time, the BRANCH models were truncated to include the upper lobe of the lung only. This involved the removal of the middle and lower lobe branches from bronchial, arterial and venous models. The number of branches in the new bronchial, arterial and venous branching networks was reduced by approximately 60%.

For regions outside the lung boundary, conventional DOSXYZnrc voxelated transport was performed. In these voxel regions, the PRESTA-II condensed history electron transport and the EXACT boundary crossing algorithm were used. Due to the complexity of the

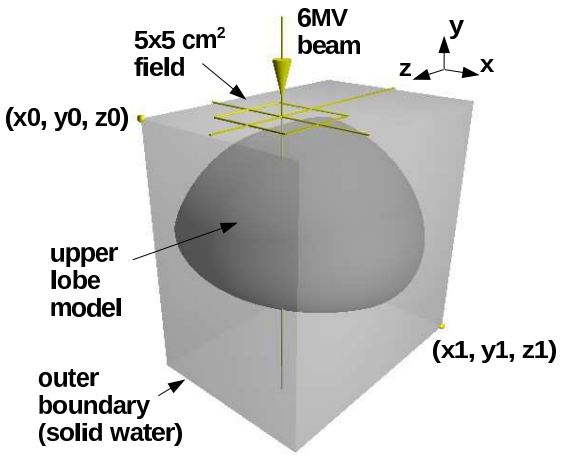

Figure 5.9: The BRANCH simulation setup: The upper lobe of the lung model is situated within a solid paralleliped of water. A 6 MV beam is incident on the phantom along the y axis. The 5x5 cm^2 field is shown. The isocenter of the beam is within the phantom and is located at (-5 cm, 1 cm, -7 cm). (Axes not at origin).

non-voxelated BRANCH geometries, a HOWNEAR routine could not be written. Therefore, electron transport within the lung boundary was performed in single scatter mode. For the non-voxelated regions, the EXACT boundary crossing algorithm was used. The ECUT and PCUT parameters were set to 0.7 and 0.01 MeV respectively. All MC transport parameters were left at their recommended (default) values. No variance reduction techniques were used. A 16 node cluster consisting of four 2.2 GHz Opteron 275 processors and one 2.2 GHz AMD Phenom 9550 was used to perform the Monte Carlo calculations. Each node had 1 Gb of memory.

5.4.2 Region composition and density

There are eleven region indices assigned in the BRANCH model. The first region corresponds to lung tissue, which refers to regions inside the lung, but outside the branching networks. The second and third regions define the spherical and cylindrical walls of the bronchioles (walls composed of tissue only). The fourth and fifth regions define the spherical and cylindrical walls of the bronchi (walls composed of cartilage). The sixth and

seventh regions define the spherical and cylindrical portions of the bronchial airway. The eighth and ninth regions define the spherical regions of the arterial and venous branches. Finally, the tenth and eleventh regions define the cylindrical portions of the arterial and venous branches. Each region in the BRANCH code was assigned an appropriate material and density from a list of materials defined in ICRU Report 44 (*ICRU Report 44 : Tissue Substitutes in Radiation Dosimetry and Measurement*, 1989) (see Table 5.3).

Table 5.3: Atomic composition (in %) and density for regions of the BRANCH model.

Region	H	C	N	O	Other	Density (kg/m^3)
Lung Tissue	10.3	10.5	3.1	74.9	0.2Na,0.2P, 0.3S, 0.3Cl, 0.2K	125-300
Bronchiole Wall,Artery,Vein	10.2	14.3	3.4	71.0	0.1Na,0.2P, 0.3S, 0.1Cl, 0.4K	1050
Bronchi Wall	9.6	9.9	2.2	74.4	0.5Na, 2.2P, 0.9S, 0.3Cl	1100
Airways	-	0.0124	75.5	23.18	1.283Ag	1.205

5.4.3 The BRANCH code subroutines

The flowchart in Fig.5.10 gives a general outline of the BRANCH code logic. There are three main subroutines used by the BRANCH code: (1) BOUNDARY, (2) TISSUE and (3) BVA.

5.4.3.1 BOUNDARY

The role of BOUNDARY (see Fig.C.1 for flowchart logic) is to determine what type of transport is to be performed (i.e. voxelated or non-voxelated). BOUNDARY uses the conventional DOSXYZnrc voxel grid to discretize the volume of the BRANCH model. When BOUNDARY is first called, it checks whether the voxel encompassing the current particle (calculated from the particle's position) is inside or outside the lung volume. Each of the eight corners of the voxel is checked against the lung's outer boundary. If all or some of the corners of the voxel are outside the boundary, the BOUNDARY code is terminated and HOWFAR proceeds with normal voxelated transport. If all corners of the voxel are inside the lung boundary, transport is carried out using the non-voxelated boundaries. This

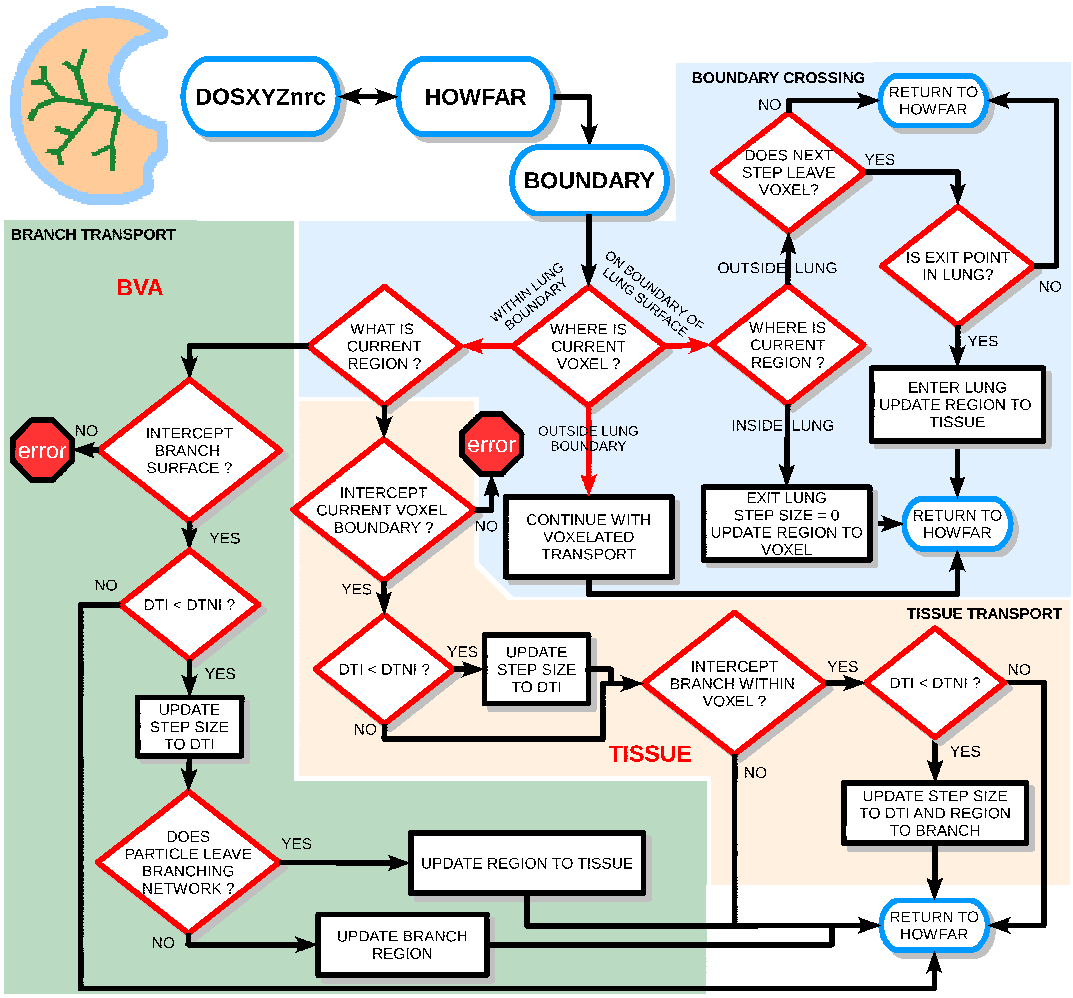

Figure 5.10: The BRANCH model algorithm: The BRANCH model consists of an anatomic representation of the lung's right outer boundary filled with bronchial, arterial and venous branches. The outer boundary (blue) is defined by several polynomial surfaces. The branching airways (tan) are constructed from a series of cylinders joined together by spheres.

approach of "crossing" the lung boundary was chosen over the conventional calculation of DTI to the lung surface. Although an algorithm exists for calculating DTI to quartic surfaces, it was found that the calculation time was slow and the DTI result lacked the necessary precision. By limiting step size to the voxel dimensions, an exact DTI was not necessary. The voxels that intersect the boundary are treated as a density averaged homogeneous voxel. In this treatment, transport through the boundary is the same for both the original and modified versions of DOSXYZnrc. Since the structures of interest are inside the lung boundary, this method of boundary crossing was deemed adequate.

5.4.3.2 TISSUE

The TISSUE subroutine (see Fig.C.2 of Appendix C for flowchart) handles the transport of a particle within the lung boundary and outside the branching networks. For TISSUE to be called, the following two criteria must be met: (1) the particle region index corresponds to lung tissue and (2) all corners of the current voxel are inside the outer boundary (determined by BOUNDARY). In the original implementation of the TISSUE code, lung tissue was treated as a single region. This required TISSUE to calculate a DTI to all branches of the bronchial, venous and arterial trees. This made the code impractically slow as there were roughly 180 000 surfaces in the branching network models. To overcome this, TISSUE was reworked to transport within the boundaries of the voxelated grid. For each voxel in the grid, a list of branches that intersect the voxel is compiled. With this information, TISSUE only checks the geometries of the branches that intersect the current voxel boundaries. If there is no intercept with a branch, TISSUE transports the particle to the next voxel without changing the region. If there is a branch intercept, the particle is transported into the branching network and its region updated.

5.4.3.3 BVA

The BVA algorithm is tasked with transporting a particle through the bronchial, venous and arterial branches. Rules are established to calculate the DTI to the relevant spheres and cylinders that make up the branching networks. As an example of the BVA logic, an arterial/venous sphere would be treated as follows: (1) Calculate the DTI to the sphere

surface; (2) Determine if the DTI is less than the distance-to-the-next-interaction (DTNI)? If it is not, transport to the next interaction site and exit. If it is, transport the particle to the sphere boundary; (3) If the particle exits the sphere, check for an entrance into an adjacent branch structure (i.e. a parent, root, daughter or sister cylinder or sphere). If an entrance occurs, transport the particle into the new region and update the branch identifier. If no entrance occurs, transport out of the branching network and into lung tissue. The preceeding description applies to transport within the arterial/venous sphere. The bronchial sphere is more complicated as it is composed of both airway and wall surfaces. The cylindrical branch regions are further complicated by an increased number of relevant geometric surfaces. For a complete treatment of the BVA logic, refer to Appendix C.3.

BVA relies on five external subroutines to perform the transport process:

1. **SPH** - calculates the DTI to a sphere in a branching network. SPH is fed a sphere index which identifies where in the tree the sphere is located, a location index which tells whether the sphere is to be checked from the inside or outside, and a type index which identifies the sphere as bronchial, arterial or venous.

2. **CYL** - calculates the DTI to a cylinder in a branching network. As was the case for SPH, CYL is fed an identifier, location and type index.

3. **INCYL** - determines whether a set of cartesian coordinates is inside or outside a cylinder with a given branch and type index.

4. **INSPH** - determines whether a set of cartesian coordinates is inside or outside a sphere with a given branch and type index.

5. **CYLGEOM** - gathers geometric data about a requested branch and prepares variables for transport calculations. This routine is used by the preceeding four subroutines.

5.4.4 Initialization of transport

For the BRANCH model, the initialization subroutine XYZINIT serves three functions. The first function was to initialize and store the parameters that define the outer boundary.

The second function was to read in the geometric information for the bronchial, venous and arterial models. Branch geometry information was contained within one of three input files that were read at the beginning of a simulation run. Within the input file, bdata.dat, the bronchial branches were defined. Each line represented a single branch and was organized as follows:

$$\langle \text{index},\ r_{\text{inner}},\ r_{\text{outer}},\ \vec{x}_{\text{start}},\ \vec{x}_{\text{end}},\ \text{parent, daughter 1, daughter 2, sister} \rangle \qquad (5.6)$$

The first variable is the index identifier of the branch. The variables r_{inner} and r_{outer} represent the inner and outer radius of the branch. The cartesian coordinates $\vec{x}_{\text{start}}$ and $\vec{x}_{\text{end}}$ specify the start and end position of the branch on its axis. The remaining four variables give the index identifier for the parent, two daughter and sister branches respectively. In a similar fashion, the files adata.dat and vdata.dat defined the arterial and venous branches respectively. The format of these two files differed slightly from bdata.dat in that a single radius was given:

$$\langle \text{index},\ \text{radius},\ \vec{x}_{\text{start}},\ \vec{x}_{\text{end}},\ \text{parent, daughter 1, daughter 2, sister} \rangle. \qquad (5.7)$$

To simplify transport in the arterial and venous branches, branches were treated as solid cylinders (and spheres). This is a reasonable simplification as the dosimetric properties of tissue and blood are similar.

The third function of XYZINIT was, for each voxel, to calculate and store the index identifier of each branch that intersects the voxel volume. There were three data files created for this function. The first data file, hcstore.dat, stored the number of branch intersections for each voxel. The second data file, cstore.dat, stored the index of each branch that intersects a given voxel. The last data file, bvastore.dat contained a flag which identified a branch as bronchial, venous or arterial. For each voxel, a sphere was defined at the voxel center with a radius equal to the distance between the voxel center and outer corner of the voxel. Each branch in the model was checked for the closest distance between the voxel center and the axis of the branch cylinder. If the distance was less than the sum of the cylinder radius and the voxel sphere radius, then the branch overlapped with the voxel. The relevant branch information was then stored in the three data files. The line

number of each data file corresponds to the region index of the voxel defined in Eq.5.1. Once the data files were created, a flag was set in XYZINIT to turn off the calculation and read in the information from the data files.

5.4.5 Defining the outer bounds of the lung

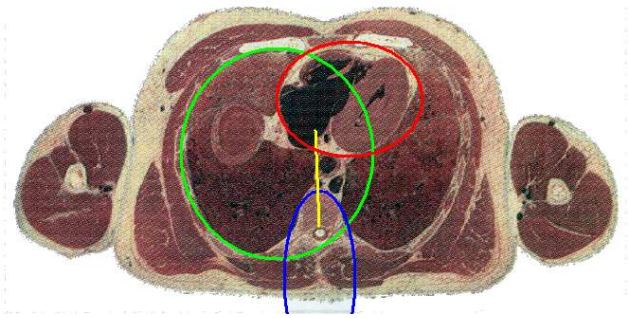

Figure 5.11: Defining the BRANCH outer boundary. A series of polynomial surfaces (ellipsoids, parabaloids etc...) were matched to anatomic features of the lung surface (Anatomic image taken from the Visible Human Project database).

Several polynomial surfaces were used to approximate the anatomic features that define the lung's surface (see Fig.5.11). The shape of the lung is defined by the contours of several adjacent anatomic structures. These include the ribcage, spine, mediastinum, heart and diaphragm. For the ribcage, spine, mediastinum and heart, the main reference for the lung's shape was the Visible Human Project (VHP) (Spitzer & Whitlock, 1998). In the VHP project, a visual atlas of the male human form was created from a consenting, healthy 38 year old death row inmate of average physical proportions. The subject, who died by lethal injection, was frozen shortly after death, imaged using CT and MRI technology, and finally cut into 1 millimeter slices from head to toe. Each slice was photographed to create a complete visual database of the male anatomy. To create a dataset from the VHP images, several transverse photographs from this database were scanned into a computer. Using a data extraction utility, a contour of each slice was taken and converted into physical coordinates. The 2D data sets were then combined into a single 3D data set to be visualized with 3D rendering software.

For the diaphragm shape, data was extracted from an article by Gauthier et al.(Gauthier, 1994). In this article, the diaphragms of 10 volunteers were imaged using MRI at four phases of respiration. Each phase of respiration was related to the total lung capacity (TLC). The four respiration phases were residual volume (23% TLC), functional residual capacity (39% TLC), functional residual capacity plus (70% TLC) and total lung capacity (100% TLC).

The surface of the ribcage was initially modelled as a simple quartoid. A planar surface was added to define the boundary of the mediastinum. A parabolic depression was then added to represent the heart. To represent the spinal column towards the lungs posterior, a hyperboloid was inserted. Finally a paraboloid representing the diaphragm at the lungs caudal surface was defined. The parameters of each of these surfaces were then adjusted to approximately match anatomic reference data. Once the adjustments were complete, the initial surface equations were generalized to the more basic quartic surface formula of Eq.(5.5). The added constants were then adjusted to better match the features of the VHP and Gauthier data. The result was a quartic represention of the ribcage and spine, a quadric representation of the heart and a planar representation of the mediastinum. Fig.5.12 shows a comparison of the VHP images in the sagittal (dividing left and right), coronal (dividing front and back) and transverse (dividing head and toe) planes with equivalent slices from the BRANCH model. It can be seen that there is good agreement between the contours of the data and the lung model.

Gauthier's work included measurements of the air volume within the lung at each of the four respiration phases imaged. The volume measurements in their work pertain to the air volume of both the left and right lung. In contrast, the BRANCH model consists only of the right lung. Further, it is not possible to exactly separate the BRANCH model volume into air and tissue components. To compare the BRANCH model volume to Gauthier's measurements, it was necessary to make several estimations. First, the total volume (air plus tissue) of the BRANCH model was estimated by overlaying a grid of volume elements (1 mm x 1 mm x 1mm) onto the BRANCH geometry. These volume elements should not be confused with the voxels that define the scoring or geometric grids of a Monte Carlo simulation. They were only used to estimate the model volume. The number of volume

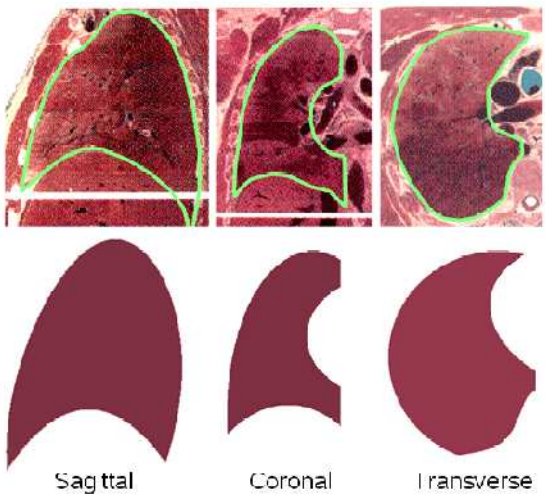

Figure 5.12: A comparison of sagittal, coronal and transverse slices from the Visible Human Project with the quartic polynomial representation of the BRANCH model outer surface.

elements completely within the BRANCH boundary were counted to estimate the model volume. Using this method, the total model volume was estimated at 1.56 L. It was then necessary to infer the total lung volume (left plus right lung) of the BRANCH model. This was done by assuming that the right lung makes up 60% of the total lung volume. This was based on the known observation that the left lung is slightly smaller than the right due to the heart volume. Applying this estimation, the total volume of the BRANCH model was 2.6 L. To estimate the air volume of the BRANCH model, it was necessary to subtract the tissue volume from the total volume. Measurement has shown that lung tissue makes up roughly 1.0 L of the total lung volume("Textbook of respiratory medicine", 2000). Subtracting the tissue volume resulted in a total air volume of 1.6 L which matched well with Gauthier's reserve volume value of 1.55 ± 0.11 L.

5.4.6 Modeling the respiration cycle

To create a model of the lung at respiration phases other than reserve volume, it was necessary to extrapolate the reserve volume case. First, quadric surfaces were fit to the diaphragm data of the remaining three respiration phases in Gauthier's work. Due to a lack of measured data, the remaining boundary surfaces were varied to follow the basic

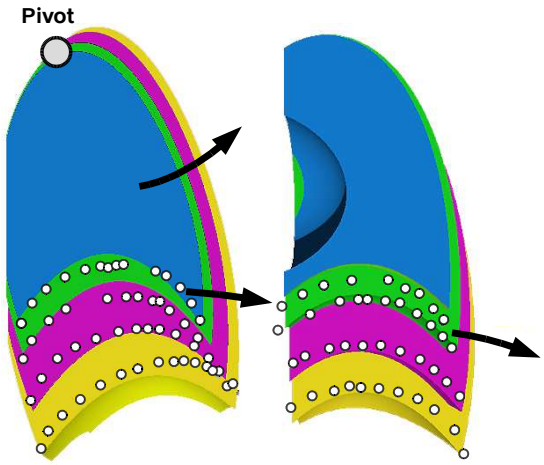

Figure 5.13: A comparison of BRANCH model diaphragm shape at various phases of respiration against published diaphragm shape data (Gauthier, 1994) (points). The arrows indicate the respiratory motion of the lung model. This motion is consistent with that observed in the two compartment model.

motions of the two-compartment ribcage model (see Fig.4.12) developed by Ward et al. (Ward et al., 1992). An attempt was made to match both the diaphragm border and airway volume at the four phases measured by Gauthier in a manner consistent with the two compartment model. The parameters of the reserve volume surfaces describing the ribcage, mediastinum and heart were adjusted to match the diaphragm data while preserving correct values for lung volume. It was assumed, as is the case in the two compartment model, that the spine is static and does not change shape during the respiration maneuver.

The resulting respiratory model is illustrated in Fig.5.13. In the figure, cross sections of the BRANCH boundary model at four phases of respiration are presented. The ribcage surface meets the diaphragm along an edge that intercepts the bounds of the diaphragm data. The volume of each phase was calculated as in the reserve volume case to show good agreement with the Gauthier data. The results are outlined in Table 5.4.

Once the boundary surfaces were defined for the four phases of respiration, the boundary parameters were fitted to simple polynomial functions to derive a single set of surface equations as a function of %TLC (See Appendix B for the analytical form of the boundary surfaces).

Table 5.4: A comparison of estimated air volume for the BRANCH boundary to measurements taken by Gauthier et al.

	Volume in Litres			
%TLC	Measured	Model		
	Both Lungs Air	Right Lung Air + Tissue	Both Lungs Air+Tissue	Both Lungs Air
22.6	1.55±0.11	1.56	2.60	1.60
38.8	2.66±0.18	2.14	3.56	2.56
69.4	4.75±0.21	3.34	5.57	4.57
100.0	6.84±0.28	4.67	7.78	6.78

5.4.7 The bronchial model

The bronchial tree model was generated using an algorithm created by Kitaoka et al. (Kitaoka, Takaki, & Suki, 1999). Their code, written in C++, generates a dichotomous, asymmetric branching network of hollow cylinders from the trachea down to the terminal bronchioles. The model consists of more than 54,000 branches broken up into 5 lobes and 18 segments as is the case in the lung. The branches are bound by several polynomial surfaces that define the allowable branching volume. The use of these polynomial surfaces in the Kitaoka code was a motivating factor in the choice of boundary surfaces for the BRANCH model.

The Kitaoka algorithm contains two key criteria that each branch in the tree must satisfy. The first is that the volume of a given branch is directly related to the volume it supplies. The second is that the terminal branches are distributed equally thoughout the lung volume. These conditions are achieved, in part, by defining branch characteristics based on the expectation that the bronchial tree is designed for optimal flow conditions.

For minimum work to be achieved, it has been shown (Murray, 1926) that the flow rate through a branch is related to its diameter using the following equation:

$$Q \propto d^n \tag{5.8}$$

In the formula, Q represents the volume flow rate, d, the diameter of a branch and n, the diameter exponent. The constant of proportionality is dependent on the type of fluid flowing through the system. For minimum work in the lung, the value of n has been

estimated to be between 2.4 and 2.9 for various mammal species (Horsfield & Thurlbeck, 1981a). In the work of Kitaoka et al., the value of n was set at 2.8. Since flowrate is conserved, the flow rate of two daughter branches will be equal to that of the parent:

$$\begin{aligned} Q_0 &= Q_1 + Q_2 \quad (5.9) \\ d_0^n &= d_1^n + d_2^n. \quad (5.10) \end{aligned}$$

The flow dividing ratio is then defined as the ratio of the flow of the smaller daughter to that of the parent:

$$r = \frac{Q_1}{Q_0} = \left(\frac{d_1}{d_0}\right)^n. \quad (5.11)$$

Substituting back into Eq.(5.10), the daughter diameters can be related to the parent diameter by the following:

$$\begin{aligned} d_1 &= d_0 r^{1/n} \quad (5.12) \\ d_2 &= d_0 (1-r)^{1/n}. \end{aligned}$$

Assuming that the total volume of the parent and daughter branches is also minimized, it has been shown (Kamiya, Togawa, & Yamamoto, 1974) that the angle of the daughter branches (θ_1 and θ_2) off the parent branch are related to the branch diameters as:

$$\frac{d_0^2}{sin(\theta_1 + \theta_2)} = \frac{d_1^2}{sin\theta_1} = \frac{d_2^2}{sin\theta_2}. \quad (5.13)$$

Combining Eq.5.12 and Eq.5.13, branching angles for each daughter branch can written as:

$$\begin{aligned} cos\theta_1 &= \left[1 + r^{4/n} - (1-r)^{4/n}\right] / 2r^{2/n} \quad (5.14) \\ cos\theta_2 &= \left[1 + (1-r)^{4/n} - r^{4/n}\right] / 2(1-r)^{2/n}. \end{aligned}$$

When the branch diameter and branching angle were defined in this manner, the resulting bronchial model was found to match well with morphometric data.

The Kitaoka algorithm is composed of nine basic rules that compliment the optimal flow formalism:

1. Branching is dichotomous (based on observation).

2. The parent and two daughters branches lie in the same branching plane (based on observation).

3. Flow rate is conserved (conservation of mass).

4. The region supplied by a parent is divided into two separate daughter regions by a space-dividing plane perpendicular to the branching plane (a space dividing scheme to evenly fill the lung volume).

5. The flow-dividing ratio (r) is set equal to that of smaller daughter volume over the parent volume (uniform fill of the volume).

6. Diameters and branching angles of the daughter branches are determined by Eq.5.12 and Eq.5.14.

7. The length of each daughter branch is three times its diameter (based on experimental data).

8. The branching plane of a daughter branch is rotated 90 degrees from the branching plane of the parent (isotropic breakup of lung volume).

9. Branching is terminated once a threshold flow rate is reached or a branch leaves the region it supplies (branching termination).

For the BRANCH model, the Kitaoka code was modified to include the reserve volume lung boundary described in Section 5.4.5 . The re-definition of the lung boundary was motivated by the desire to introduce a more detailed boundary than the one used in the Kitaoka code. Since the BRANCH model was representative of the right lung alone, the Kitaoka code was also adjusted to exclude the generation of a left bronchial tree.

The resulting bronchial tree model (illustrated in Fig.5.14) contained 27,798 branches ranging from 0.02-0.54 cm in diameter. The branches of the bronchial tree model were labeled using the Strahler ordering convention illustrated in Fig.4.5. The branching, diameter and length ratios were extracted for comparison to measured values. The Strahler

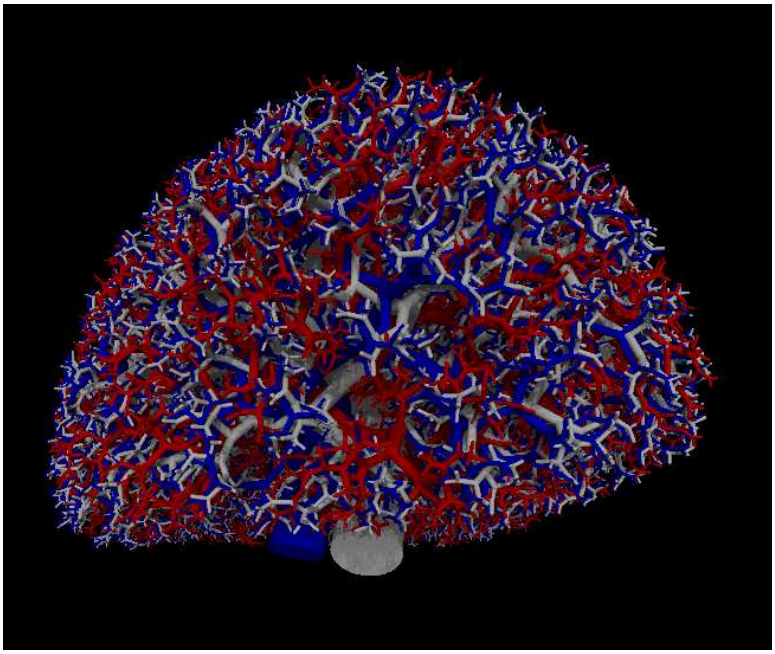

Figure 5.14: Model of the branching networks: The bronchial tree is represented in light grey, arteries in blue and veins in red.

plots, shown in Fig. 5.15, yielded a branching ratio of 2.77 which fell within the acceptable range outlined in Table 4.1. The diameter and length ratios were calculated to be 1.34 and 1.37 respectively. These values also fell within the range given in Table 4.1.

In addition to branch, diameter and length ratios, the bronchial tree was analyzed for other geometric parameters such as branching angle and L/D ratio. These results, outlined in Table 5.5, indicated that the bronchial model had geometric dimensions similar to the true bronchial tree.

5.4.8 The arterial/venous models

The modified Kitaoka bronchial algorithm was re-used to generate models of the arterial and venous branching networks. Since it was assumed that the arterial and venous networks are designed for optimal flow, the bronchial model formalism was deemed applicable. The Kitaoka code was expanded to generate the bronchial, arterial and venous branches concurrently. The main difference between the networks was the initial position and orientation of the root branches from which the trees were "grown". Morphometric

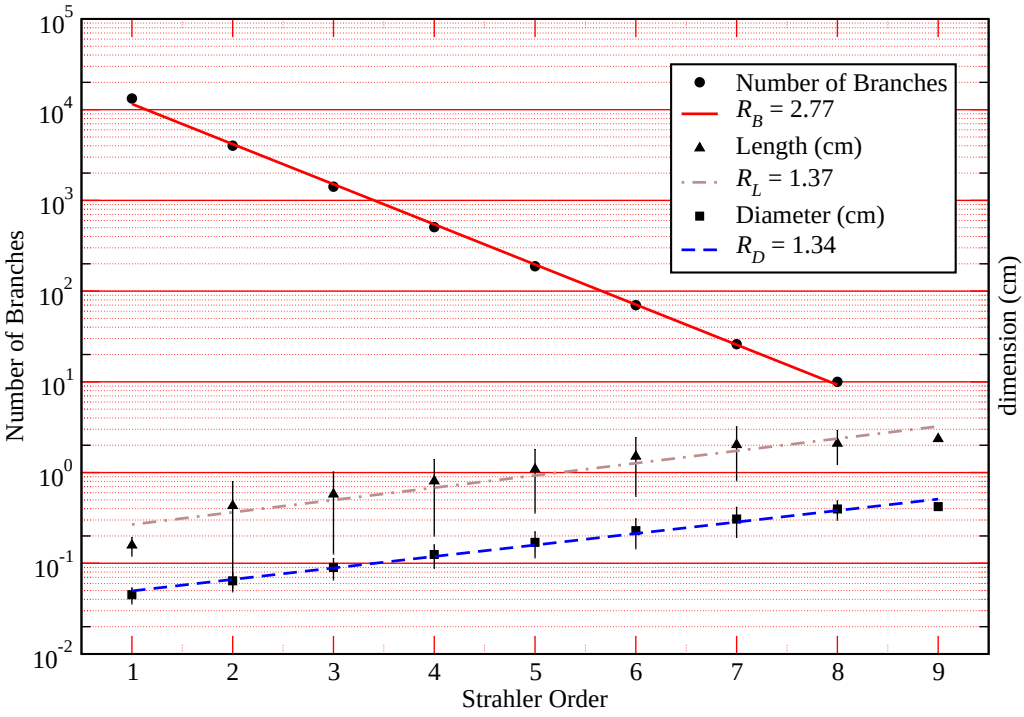

Figure 5.15: Plot of bronchial number, diameter and length vs. Strahler order.

Table 5.5: The geometry of the BRANCH bronchial tree compared to published data. Variables used in Table are defined in Fig.4.7.

	Model	Published	Reference
L/D	3.15 ± 0.75	3.04 ± 2.20	(Merryn et al., 2004)
		3.09, 3.14	(Sauret et al., 2002)
		3.25 ± 0.65	(Weibel, 1963)
L/D_{minor}	3.29 ± 0.75	3.63 ± 2.57	(Merryn et al., 2004)
		2.96 ± 0.97	(Phillips & Kaye, 1995)
L/D_{major}	3.00 ± 0.75	2.48 ± 1.79	(Merryn et al., 2004)
		2.71 ± 1.13	(Phillips & Kaye, 1995)
D/D_{parent}	0.78 ± 0.10	0.71 ± 0.14	(Merryn et al., 2004)
		0.83, 0.78	(Sauret et al., 2002)
		0.79	(Weibel, 1963)
		0.76	(Krause et al., 1995)
D_{min}/D_{parent}	0.66 ± 0.12	0.66 ± 0.12	(Merryn et al., 2004)
D_{maj}/D_{parent}	0.89 ± 0.08	0.79 ± 0.12	(Merryn et al., 2004)
		0.86	(Phillips & Kaye, 1995)
D_{min}/D_{maj}	0.74 ± 0.16	0.85 ± 0.14	(Merryn et al., 2004)
		0.82, 0.74	(Sauret et al., 2002)
		0.86 ± 0.01	(Weibel, 1963)
		0.77	(Phillips & Kaye, 1995)
L_{min}/L_{maj} $(L_{min} < L_{maj})$	0.71 ± 0.18	0.52 ± 0.23	(Merryn et al., 2004)
		0.58	(Sauret et al., 2002)
		0.62 ± 0.20	(Weibel, 1963)
L/L_{parent}	0.81 ± 0.33	0.85	(Merryn et al., 2004)
		0.94 ± 1.37	(Krause et al., 1995)
θ	$49.82^\circ \pm 16.89^\circ$	$36.11^\circ \pm 20.85^\circ$	(Merryn et al., 2004)
θ (D $\geq$ 4 mm)	$18.43^\circ \pm 17.79^\circ$	33.98°	(Merryn et al., 2004)
		32°	(Horsfield et al., 1971)
θ (4 mm $>$ D $\geq$ 3 mm)	$39.89^\circ \pm 17.71^\circ$	41.06°	(Merryn et al., 2004)
		30°	(Horsfield et al., 1971)
θ (3 mm $>$ D $\geq$ 2 mm)	$43.97^\circ \pm 20.78^\circ$	36°	(Horsfield et al., 1971)
θ (2 mm $>$ D $\geq$ 1 mm)	$47.68^\circ \pm 20.07^\circ$	43°	(Horsfield et al., 1971)
θ (1 mm $>$ D $\geq$ 0.7 mm)	$48.12^\circ \pm 19.14^\circ$	50°	(Horsfield et al., 1971)
ϕ	$75.6^\circ \pm 12.7^\circ$	$76.05^\circ \pm 45.73^\circ$	(Merryn et al., 2004)

observation has shown that arterial network closely follows the path of the bronchial network. This observation was reproduced in the arterial model. The venous network path is somewhat independent from those of the bronchial and arterial trees. Furthermore, the venous tree has a two trunk origin entering the lung. To generate a venous model from the bronchial model code, the venous tree was split into two single trunk trees with different branch origins. The resulting venous model filled the remaining space not occupied by the bronchial and arterial trees. When a branching model was generated, intersections between branches occurred. An algorithm was added to the Kitaoka code which identified and removed intersections between the bronchial, arterial and venous networks. The algorithm identified the intersection of two branches based on their radii and perpendicular distance apart. If an intersection occurred, the two branches were translated in opposite directions along the perpendicular. To remove new intersections created from the translation, the intersection removal process was repeated several times. After the process was complete, the code identified any branch that still intersected another and wrote collision information to the terminal. It was found that roughly 100 collisions still remained after branch generation was complete. The majority of these intersections involved large branches near the root of the tree. Part of the difficulty in removing these intersections automatically was the inflexible shape of the large branches. A branch may be bent or curved to fit within a confined space. Since, for this thesis, structure below the CT resolution threshold was of interest, large intersecting branches were removed. In addition, if an intersecting branch was found to be terminal (i.e. had no daughter) it was removed from the branch model.

The arterial tree model contained 27,957 branches ranging from 0.02-1.2 cm in radius. The venous tree contained 26,347 branches ranging from 0.02-0.34 cm in radius. Compared to the bronchial tree, there is a less extensive set of published results for arterial and venous tree morphometry. The arterial model branching ratio had a value of 2.81 which was roughly comparable to the 2.99 value published be Singhal et al. (Singhal et al., 1973) and somewhat low compared to the 3.33 and 3.10 values published by Huang et al. (Haung, Yen, McLaurine, & Bledsoe, 1996) and Horsfield et al. (Horsfield, 1978) respectively. The lower branching ratio of the arterial model may be due to the omis-

sion of lateral arterial branches. In the true arterial tree, there are small arterial branches that shoot off the branching network at right angles. These branches are included in the Strahler counting of the published data. Although the arterial model is not exact, it still gives a general representation of the composition and density distribution of the true arterial tree. The diameters and lengths of the arterial branch model (see Fig.5.16) were

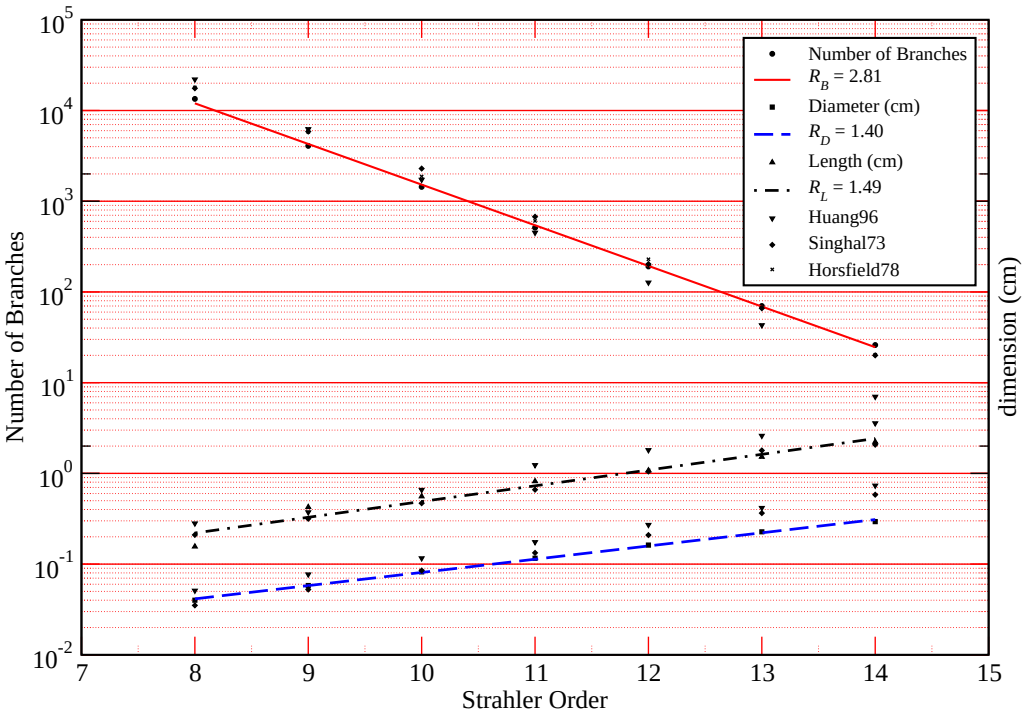

Figure 5.16: Plot of arterial branch number, diameter and length vs. Strahler order.

slightly lower than those published by Singhal and Horsfield. The diameter and length ratios of the model were 1.40 and 1.49 respectively. These values are lower than the ratios obtained from other publications: R_D=1.56, 1.55 and R_L=1.60, 1.49 from Huang and Singhal respectively.

For the venous tree, the branching, length and diameter ratios were 3.00, 1.44 and 1.46 respectively (see Fig.5.17). The same values from Huang et al. (Haung et al., 1996) were estimated at 3.45, 1.63 and 1.75 respectively. These values are much higher than the values published by Horsfield and Gordon (Horsfield & Gordon, 1981) which were 2.73, 1.35 and 1.47. The venous model ratios are between the values of the two published results.

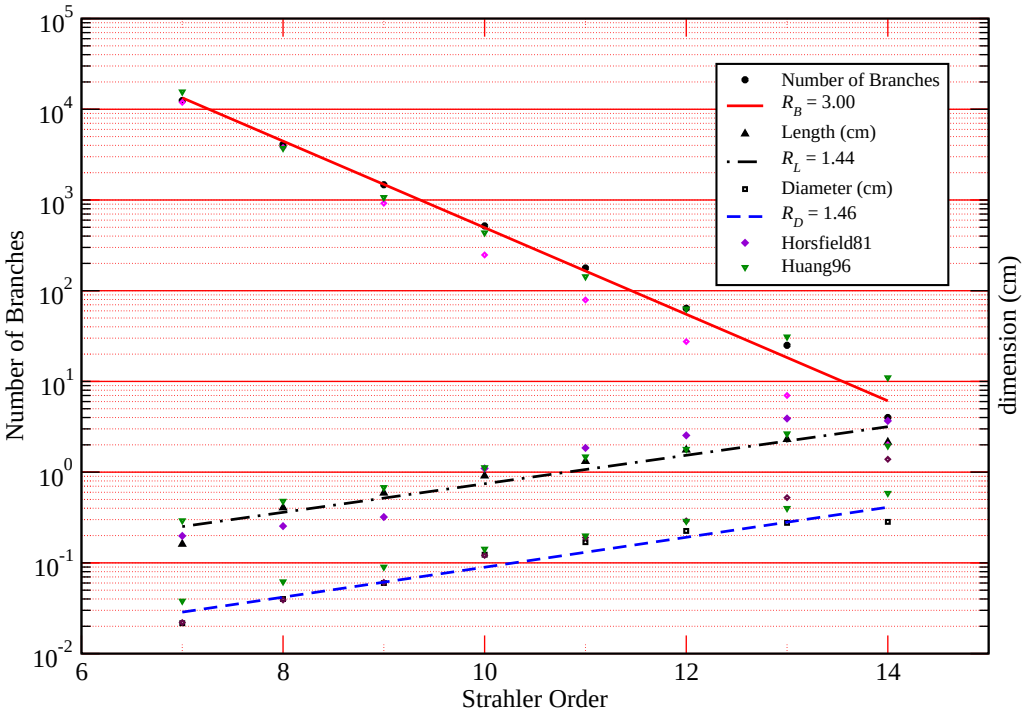

Figure 5.17: Plot of venous branch number, diameter and length vs. Strahler order.

5.4.9 Verifying the BRANCH code

To ensure that transport within the BRANCH Monte Carlo model was correct, several error checks were added to the code. If any of the following conditions were met, the code would output an error:

1. a particle's region index corresponded to a region outside the lung boundary but its position was inside the boundaries of the lung
2. a particle's region index corresponded to a region inside the lung boundary but its position was outside the boundaries of the lung
3. a particle's region index corresponded to a branch region but its position was outside the branching networks
4. a particle's region index corresponded to lung tissue but its position was inside a branching network
5. a particle's region index corresponded to a bronchial airway but its position was inside a bronchial wall
6. a particle's region index corresponded to a bronchial wall but its position was inside a bronchial airway
7. a bronchi was incorrectly assigned a region index corresponding to a bronchiole (and vice versa)

The BRANCH code was modified to temporarily output particle position, particle direction, region index, region density and branch index at the end of each transport step. An examination of this output clearly showed that particles correctly moved from outside the lung to inside the lung tissue, then in and out of several branches, and finally out of the lung. Density and medium indices were correctly assigned and the code was stable.

To test the validity of a BRANCH dose calculation, an all-water version of the branch model was created. The test model had an identical geometry to the total lung capacity (inhale) model described in Section 5.4.1. The only difference was that all regions were

assigned the medium water (H2O700ICRU from the PEGS4 file 700icru.pegs4dat which was included with the EGS distribution) and a density of 1.00 g/cm^3. A simulation was run using the 3x3 cm^2 field as a source. To improve statistical uncertainty in the dose results, the scoring grid was re-binned so that each voxel was 0.2 cm x 0.2 cm x 0.2 cm in dimension. Percent depth dose curves and crossplane/inplane profiles were extracted from the resulting dose distributions. These results were compared to depth dose curves and profiles from a conventional DOSXYZnrc simulation using a voxelated homogeneous water phantom. The percentage depth dose plot, shown in Fig.5.18, indicates good agreement between the two simulations. A percent difference analysis defined as:

$$PD_{BRA,DOS} = 100 \cdot \frac{(D_{BRA} - D_{DOS})}{D_{DOS}} \tag{5.15}$$

showed that the two depth dose curves varied by less than 1% for the majority of data points. Analysis of the crossplane/inplane profiles also showed good agreement between the BRANCH and DOSXYZnrc simulations (see Fig.5.19). A gamma analysis defined as:

$$\gamma(x_{BRA}, D_{BRA}) = \min \sqrt{\left(\frac{x_{\mathrm{BRA}} - x_{\mathrm{DOS}}}{x_{\mathrm{TOL}}}\right)^2 + \left(\frac{PD_{\mathrm{BRA,DOS}}}{D_{\mathrm{TOL}}}\right)^2} : \forall(x_{DOS}, D_{DOS}) \tag{5.16}$$

(refer to Eq.3.2 on page 30 for details on gamma analysis) indicated that BRANCH and DOSXYZnrc profiles agreed within a position tolerance of 0.1 cm and a percent difference in dose of 0.5%. A χ^2 comparison of the two distributions yielded a value of 0.62 which indicated that the two distributions were statistically indiscernible. From these results, the BRANCH code was deemed ready for use.

5.5 The CT representation of the TISSUE and BRANCH models

After defining the BRANCH and TISSUE models, a computed tomography (voxelated) representation of each was created for input into the Pinnacle^3 treatment planning system and DOSXYZnrc Monte Carlo code. For Monte Carlo simulations, the atomic composition and density of each CT voxel was defined. For Pinnacle^3 CCC calculations, the resulting density information was converted into Hounsfield units and written into the

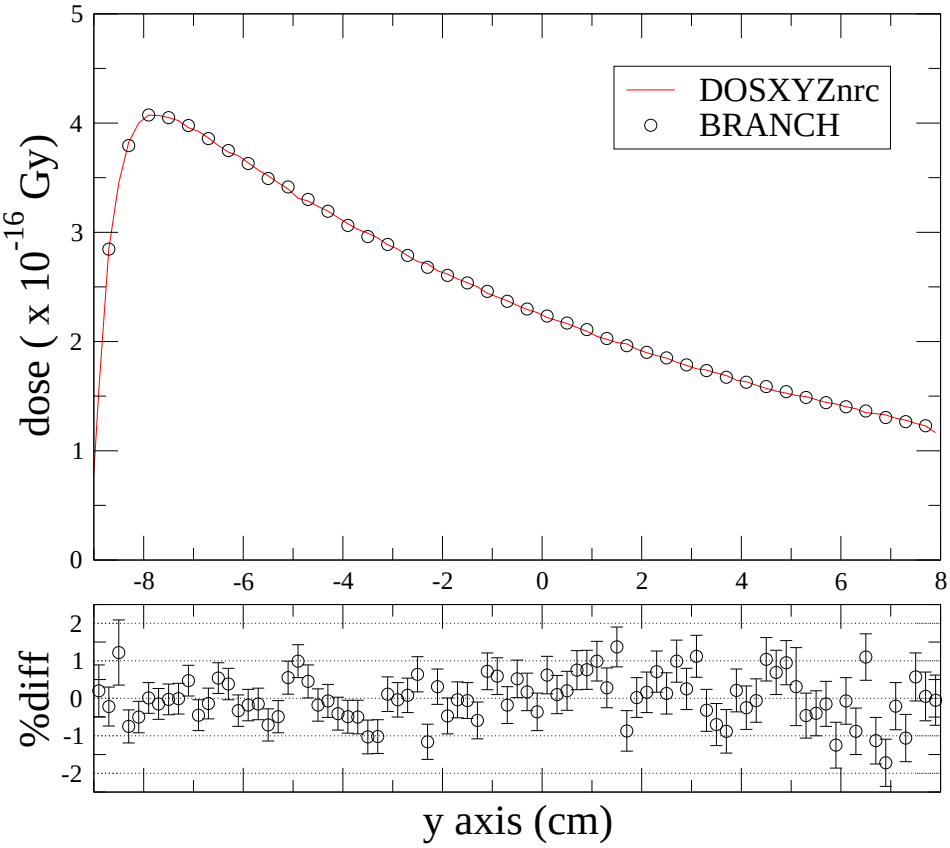

Figure 5.18: Comparison of all-water BRANCH simulation and the voxelated homogeneous DOSXYZnrc simulation depth dose curves: In the bottom figure, the percent difference between the two simulations is presented. The dose uncertainty in each distribution was approximately 0.5%.

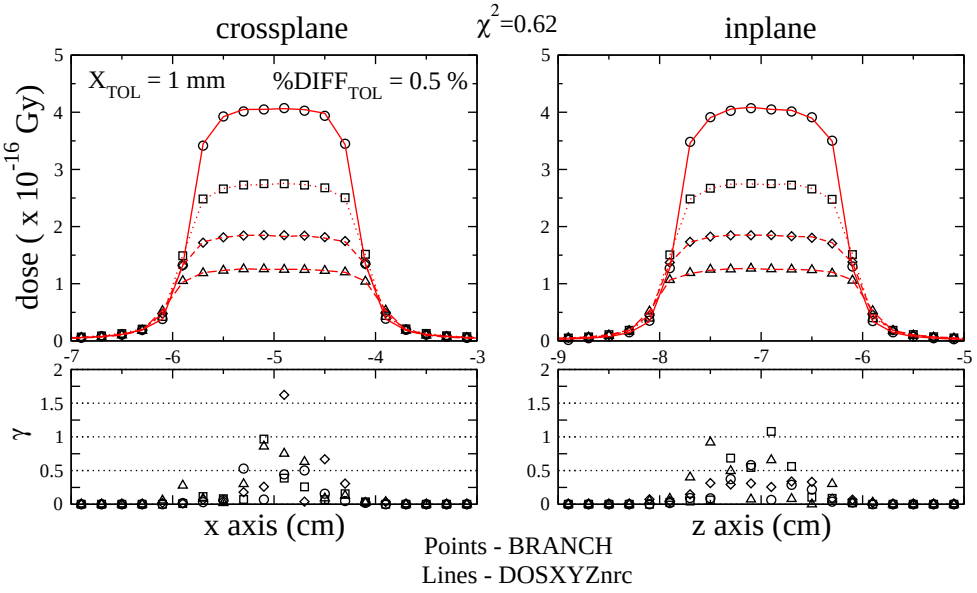

Figure 5.19: Comparison of all-water BRANCH simulation and the voxelated homogeneous DOSXYZnrc simulation crossplane/inplane profiles: In the top two figures are the crossplane and inplane profiles at depths of -7.5, -2.5, 2.5 and 7.5 cm along the beam axis of the BRANCH model. The bottom two figures show the value of the γ function for each profile. The positional and dose percent difference tolerances were set at 0.1 cm and 0.5% respectively.

pinnacle CT binary format. The following two sections describe the creation of the CT models.

5.5.1 The BRANCH CT model

A CT representation of each BRANCH model was defined within a DOSXYZnrc egsphant file. The egsphant file is read in at the beginning of a DOSXYZnrc simulation and defines:

1. The PEGS4 media names used in the simulation (see Table 5.3).
2. The number of voxels along each of the three Cartesian directions.
3. The position of the voxel boundaries along the three Cartesian directions.
4. The medium and density of each voxel.

The egsphant file was generated by a small code called CTGEN. In CTGEN, the density within each voxel was calculated by sampling the density on a discrete grid of points. At each sample point, the point position was checked against all the regions of the branching model (airway, bronchial wall, etc...). If the sample point was inside a bronchial airway, it was indexed as an airway point. If the sample point was inside an artery, it was indexed as an artery and so forth. A tally was kept of the number of points within each BRANCH model region. The number of sample points for each region (N_{region}) divided by the total number of sample points in the sample grid (N_{tot}) was taken to be the fraction of the total voxel volume occupied by each region. The density was calculated by multiplying the fractional volume by each density as follows:

$$\rho = \sum_{i=1}^{4} \frac{m_i}{V_{tot}} = \sum_{i=1}^{4} \frac{\rho_i V_i}{V_{tot}} \approx \sum_{i=1}^{4} \frac{\rho_i N_i}{N_{tot}} \tag{5.17}$$

where i is the region index and 4 is the number of material regions in the BRANCH model (air, tissue, lung and cartilage).

The accuracy of the density calculation was dependent on the number of sample points. To determine the number of sample points needed, two simple phantoms were created. Both phantoms consisted of a single voxel that was 0.1 cm x 0.1 cm x 0.2 cm in dimension. Within one phantom (voxel) a single cylindrical shell was centered and orientated along

the x axis. Within the second phantom, a spherical shell was centered. As was the case for the BRANCH model, the inner cylinder/sphere was assigned the composition and density of air; the cylindrical/spherical wall, was assigned the composition and density of tissue and the region outside the cylindrical/spherical geometries was assigned the composition and density of lung. The cylindrical/spherical phantom geometries allowed for an exact calculation of voxel density. The density of the cylindrical shell phantom was:

$$\rho_{voxel} = \rho_{lung} + 50\pi \left[R_i^2(\rho_{air} - \rho_{wall}) + R_o^2(\rho_{wall} - \rho_{lung})\right] \tag{5.18}$$

where R_i and R_o are the inner and outer radii of the cylindrical shell. The density of the spherical phantom was:

$$\rho_{voxel} = \rho_{lung} + \frac{2000}{3}\pi \left[R_i^3(\rho_{air} - \rho_{tissue}) + R_o^3(\rho_{tissue} - \rho_{lung})\right] \tag{5.19}$$

For each phantom, CTGEN was run using increasing numbers of sample points. Average density calculations were made for cylinder/sphere densities ranging from 0.1 to 1.1 g/cm^3 in steps of 0.1 g/cm^3 and outer cylindrical/spherical radii between 0.1 and 0.5 cm in steps of 0.1 cm. The radii of the inner cylinder was fixed at $0.6R_o$. The resulting CTGEN density values were compared to the exact values. It was found that a sampling grid of 50 x 50 x 100 was sufficient to produce a calculated density that was within 1% of the true values for all cases. For the cylindrical shell calculations the percent difference between the CTGEN and true density values ranged from 0.00-0.34% with a mean value of 0.04%. For the spherical shell calculations, the percent difference ranged from 0.01-0.95% with a mean of 0.20%

To import the phantom into the Pinnacle^3 TPS, the density information of the voxelated density grid was converted into Hounsfield units using the density-to-CT ramp function outlined in Table 5.6. The density-to-CT ramp was derived during the commissioning and calibration of the CT scanner at the Saskatoon Cancer Center.

Once the Hounsfield value for each voxel was obtained, the information was written into the CT format used by Pinnacle^3. A Pinnacle^3 CT dataset is defined by two files. The first is the header file which lays out the geometry of the voxel grid (number of voxels in x,y and z directions, voxel size and lower x,y and z bounds of the phantom). The second file is the image binary file which stores the Hounsfield array in two-byte integer form.

Table 5.6: The Pinnacle^3 TPS default density-to-CT ramp.

Medium	Density Range(g/cm^3)	Hounsfield Range (HU)
air	0	0
lung-inhale	0-0.195	0-183
lung-exhale	0.195-0.465	183-516
adipose	0.465-0.967	516-928
breast	0.967-0.991	928-969
water	0.991-1.000	969-999
muscle	1.000-1.062	999-1047
liver	1.062-1.071	1047-1056
trabecular bone	1.071-1.161	1056-1236
bone	1.161-1.609	1236-1919

5.5.2 The TISSUE CT model

Due to the simple slab geometry and well defined density of each slab, it was not necessary to create a TISSUE egsphant file. Instead, density was defined manually within the DOSXYZnrc egsinp file. The entire TISSUE geometry was set to the PEGS4 material H2O700ICRU. The density of the chestwall slab was set to 1.00 g/cm^3. The density of the lung tissue slab was varied depending on the phase of respiration being modeled (total lung capacity, functional capacity and reserve volume corresponding to densities of 0.125, 0.200 and 0.300 g/cm^3 respectively). An additional feature of DOSXYZnrc allows for the generation of an egsphant file from the user input. An egsphant file was generated and converted into a Pinnacle^3 CT dataset as described in the previous section.

CHAPTER 6

RESULTS

6.1 The TISSUE model

As mentioned in Chapter 5, dose distributions of the TISSUE model were calculated using three distinct methods:

1. MC-M: TISSUE Monte Carlo simulations using the dodecahedron model to represent the alveolar tissues of the lung. MC-M simulations transport particles through a series of dodecahedron shells. Each shell represents an individual alveoli roughly 200 μm in diameter. Along any trajectory, a particle encounters a repeating series of tissue (alveolar wall) and air (alveolar cavity) layers. The dimensions of the dodecahedron shells are set to produce attenuation consistent with lung of a desired density. MC-M transport in the alveolar tissues is non-voxelated.

2. MC-CT: DOSXYZnrc Monte Carlo simulations using the homogeneous CT representation of the dodecahedron model. Unlike the MC-M simulations, MC-CT transport is voxelated. The lung tissue region is represented by a homogeneous slab of water that is density scaled to represent lung tissue.

3. CCC: Pinnacle^3 Collapsed Cone Convolution calculations using the CT representation of the TISSUE model. The homogeneous representation of the MC-CT simulations is converted into the Pinnacle^3 CT format and dose distributions calculated using the CCC algorithm.

For all simulations, a 6 MV Varian clinac x-ray beam was used (see Chapter 3 for details on the beam model construction). For the MC-CT and CCC methods, simulations were

run for five field sizes (1x1, 3x3, 5x5, 7x7 and 10x10 cm^2) and four tissue densities (0.125, 0.200, 0.300 and 1.00 g/cm^3). Due the constraints of long simulation runtimes, the MC-M simulations were run for three field sizes (1x1, 3x3 and 5x5 cm^2) and three tissue densities (0.125, 0.200 and 0.300 g/cm^3). Monte Carlo simulations using both the MC-CT and MC-M methods had dose uncertainties ranging from 0.5-1.0%. The CCC method did not prescribe an uncertainty to its dose distributions. For each field size, dose distributions were normalized relative to the maximum central axis dose in normal water. The International Commission on Radiation Units and Measures (ICRU) Report 24 (*ICRU Report 24 : Determination of Absorbed Dose in a Patient Irradiated by Beams of X or Gamma Rays in Radiotherapy Procedures*, 1976) recommends that the delivery of dose should not have an overall uncertainty exceeding 5%. In order to achieve this, it has been estimated (Loevinger & Loftus, 1977) that the dose calculation step requires an accuracy of 2-3%. For TISSUE simulations, the tolerance on the agreement between two dose distributions was 2%.

In Fig.6.1 central axis percentage depth dose curves (PDD) for the three methods are provided. Figures 6.2 and 6.3 contain the crossplane (CP) profiles. To address the objectives of this thesis, the following subsections will make reference to these figures.

6.1.1 The effects of structure below the CT/dose resolution on dose accuracy

A qualitative examination of the depth dose curves and crossplane profiles in figures 6.1-6.3 indicates that the MC-M and MC-CT distributions are equivalent regardless of lung density or field size. To quantify the agreement between MC-M and MC-CT dose values, the percent difference was defined as follows:

$$PD = 100 \times \frac{\mathrm{D}^{(\mathrm{i})}_{\mathrm{MCM}} - \mathrm{D}^{(\mathrm{i})}_{\mathrm{MCCT}}}{\mathrm{D}^{(\mathrm{i})}_{\mathrm{MCCT}}} \tag{6.1}$$

where $\mathrm{D}^{(\mathrm{i})}$ represents the dose in the i^{th} voxel. The percent difference between MC-M and MC-CT central axis depth dose curves was calculated and is presented in Fig.6.4. In the figure, it is shown that MC-CT and MC-M depth dose curves fall within the 2% tolerance of each other for all data points with the majority of data points falling within 1%.

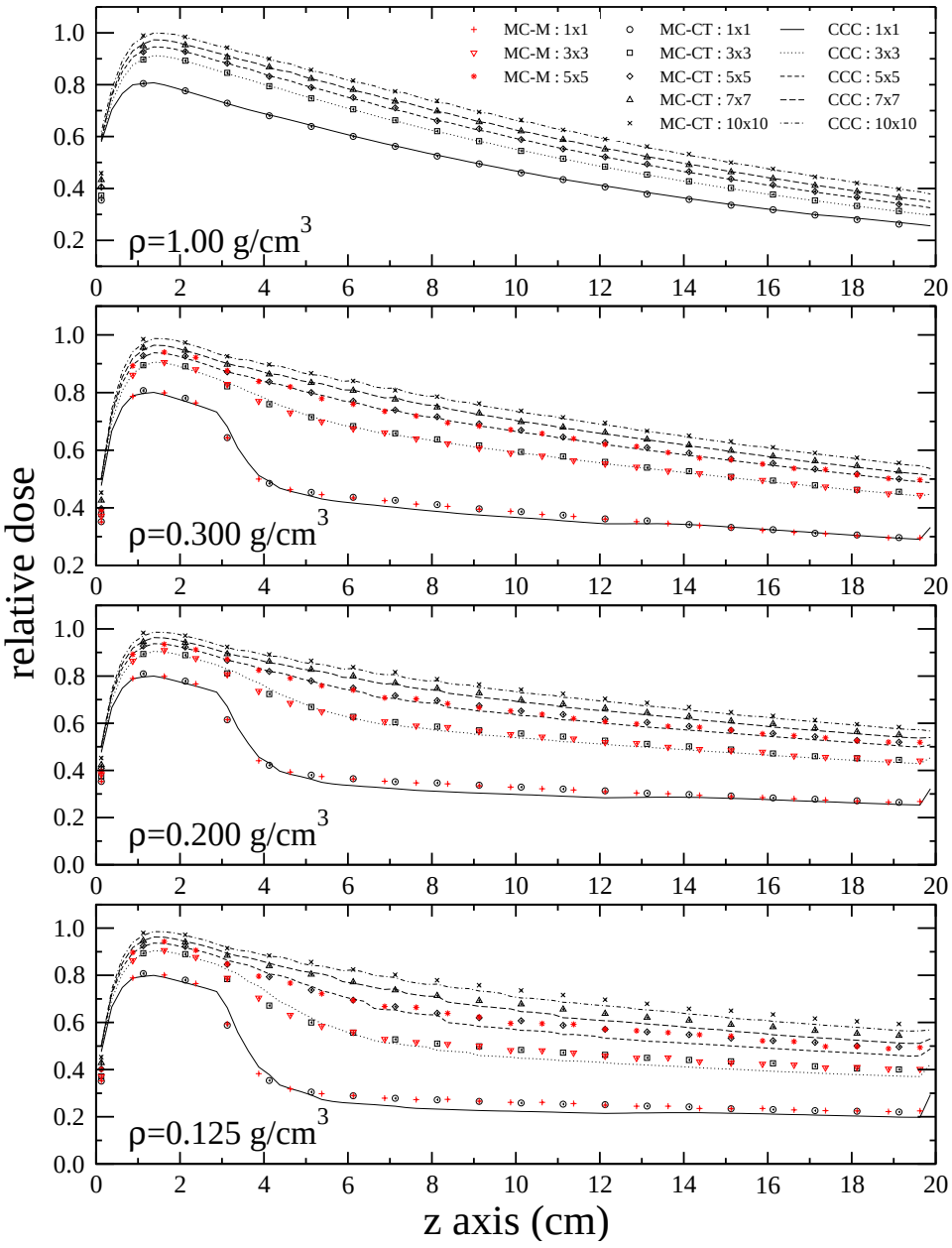

Figure 6.1: MC-M, MC-CT and CCC depth dose curves for the TISSUE model. In the figure, MC-CT, MC-M and CCC are shorthand for Monte Carlo simulation using CT model, Monte Carlo simulation using dodecahedron model and Collapsed cone convolution calculation respectively. Data points are omitted for viewability. The uncertainties in the MC-M and MC-CT dose values was roughly 0.5%. There was no assigned uncertainty in the CCC calculations.

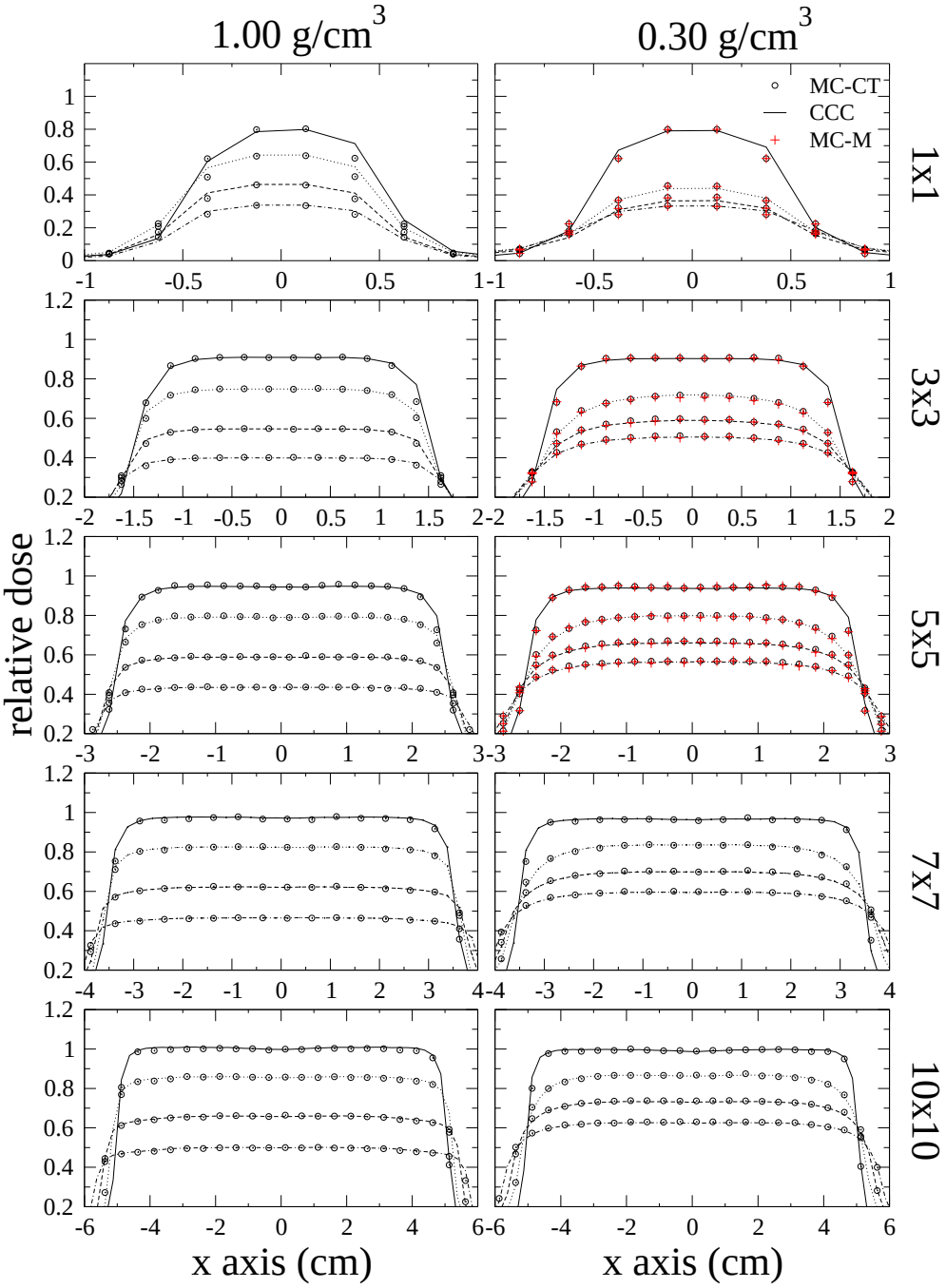

Figure 6.2: MC-M, MC-CT and CCC crossplane profiles for the 1.00 and 0.300 g/cm^3 TISSUE model. In each graph, there are four profiles corresponding to depths (from top to bottom) of 1.5, 5.0, 10.0 and 15.0 cm. The uncertainties in the MC-M and MC-CT dose values was roughly 0.5%. There was no assigned uncertainty in the CCC calculations.

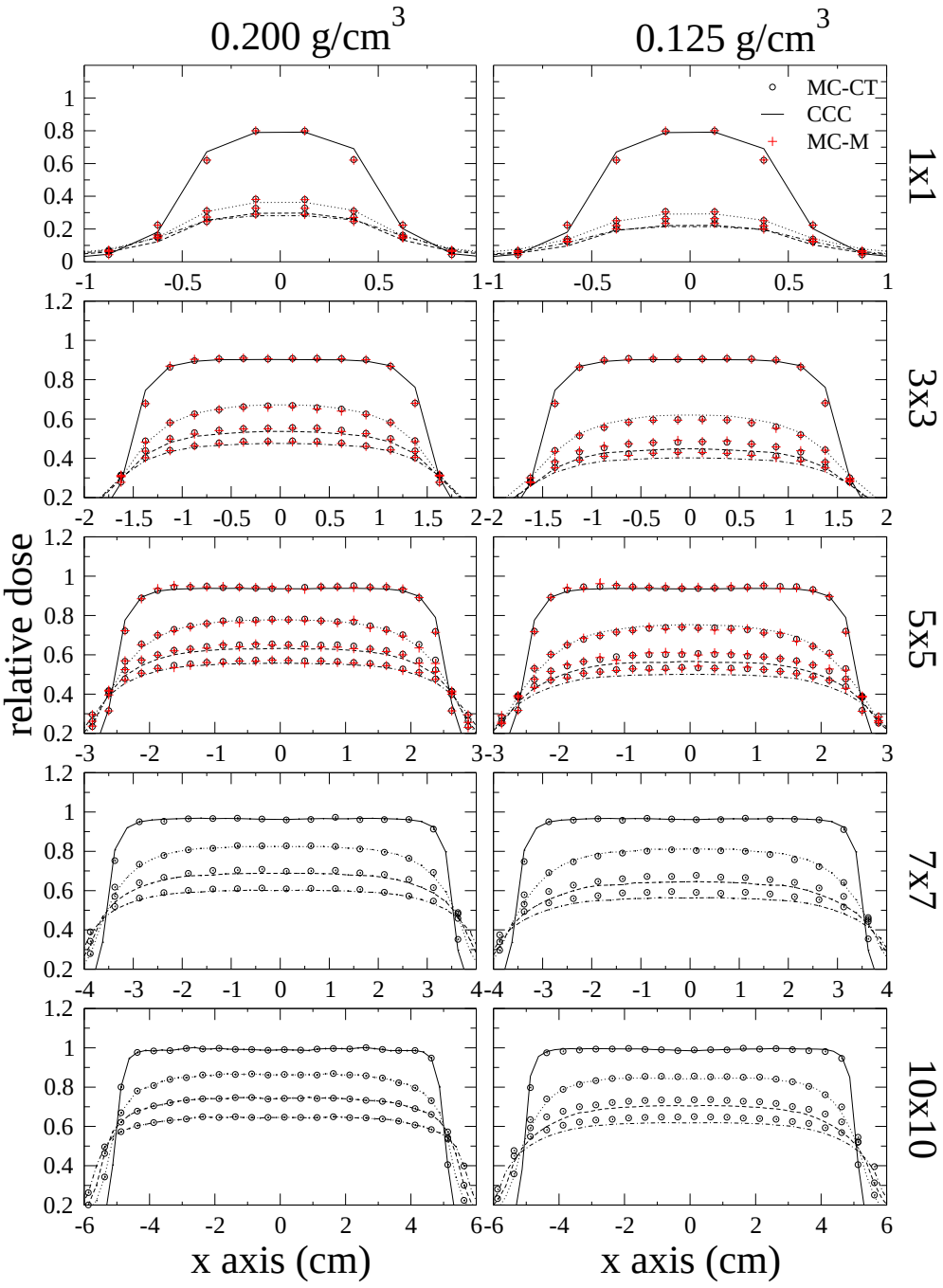

Figure 6.3: MC-M, MC-CT and CCC crossplane profiles for the 0.200 and 0.125 g/cm^3 TISSUE model. In each graph, there are four profiles corresponding to depths (from top to bottom) of 1.5, 5.0, 10.0 and 15.0 cm. The uncertainties in the MC-M and MC-CT dose values was roughly 0.5%. There was no assigned uncertainty in the CCC calculations.

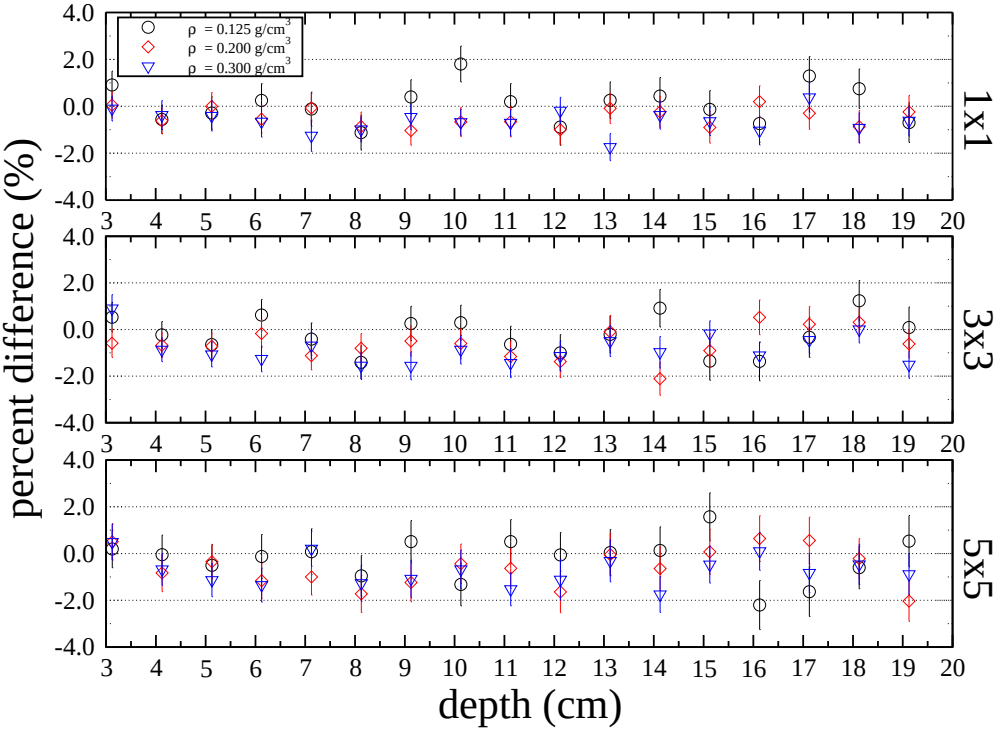

Figure 6.4: Percent difference between MC-CT and MC-M central axis depth dose curves for the TISSUE model: For the three field sizes and three lung tissue densities sampled, the MC-CT and MC-M central axis depth dose curves fall within 2% of each other. It should be noted that depths below 3 cm were omitted as that region corresponds to the chestwall slab. In the chestwall slab for both the MC-CT and MC-M calculations, transport was identical (voxelated).

Table 6.1: Mean Percent Difference between MC-CT and MC-M simulations for the TISSUE model. There were approximately 800, 7,500 and 23,000 sample voxels for the 1x1, 3x3 and 5x5 distributions respectively. The uncertainty in the percent difference (propagated from uncertainty in dose) was roughly 1%. The uncertainty in the mean percent difference was less than 0.01%.

Density	Mean Percent Difference ± Sample Deviation (%)		
g/cm^3	1x1	3x3	5x5
0.125	-0.11±1.09	0.25±0.86	0.30±1.07
0.200	0.46±0.60	0.63±0.62	0.69±0.87
0.300	0.60±0.52	0.83±0.56	0.85±0.81

To quantify the agreement between MC-M and MC-CT dose distributions, the percent difference as a function of phantom volume was calculated. Data points within the lung tissue slab with dose values greater than 80% of the maximum dose at the same depth were sampled. The percent difference in dose for each voxel was calculated and binned at 1% intervals. The number of sample points in each bin was normalized to the total number of voxels sampled to calculate the fraction of total volume. The average uncertainty in the resulting percent difference values (propagated from the uncertainty in dose) was less than ±1%. A plot of percent difference vs. percent volume (see Fig.6.5) showed that, for the three field sizes and three lung tissue densities sampled, the MC-CT and MC-M distributions fell within the 2% prescribed tolerance of each other over the majority of the sampled volume. For each percent difference distribution in Fig.6.5, a mean percent difference and associated sample deviation was calculated. The results, presented in Table 6.1 confirm that the mean percent difference is centered near zero for all comparisons. There is a subtle increase in percent difference as a function of increasing field size and/or increasing density. However, the increase is not statistically significant. From these results, it is concluded that the explicit inclusion of the connective tissue structures of the lung in the dose calculation did not introduce a significant change in the resulting dose distributions. There is no loss in dose accuracy when the connective tissue structures of

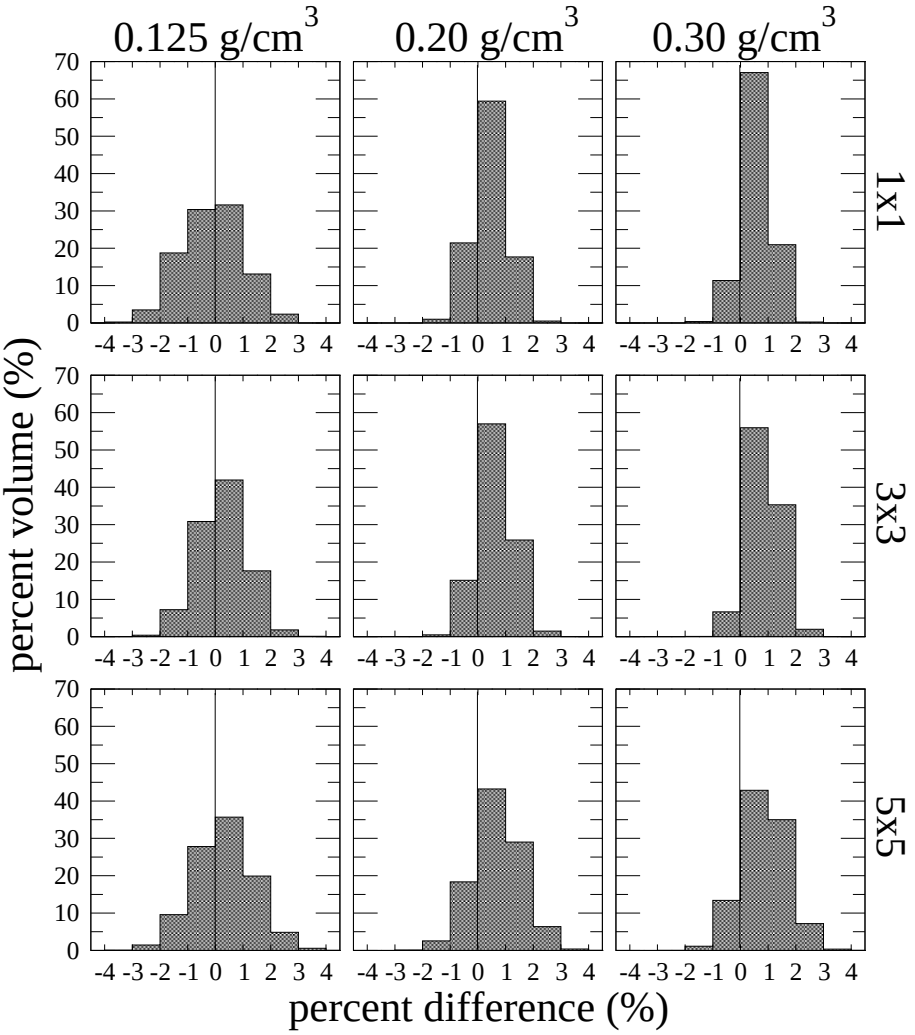

Figure 6.5: Percent difference vs. percent volume between the MC-CT and MC-M dose distributions for the TISSUE model: The percent difference was calculated for voxel pairs with dose values greater than 80% of the central axis dose at equal depth. The resulting set of percent difference values were binned at percent difference intervals of 1%.

the lung are represented as a homogeneous region uniform in both atomic composition and density.

6.1.2 The effects of structural variation due to respiration on dose accuracy

There is not a significant change in the percent difference between MC-CT vs MC-M dose distributions as as a function of respiratory phase. As illustrated in Table 6.1, there is a marginal increase in the mean percent difference as a function of increasing density. However for the three phases of respiration simulated, the mean percent difference between MC-CT and MC-M dose distributions was within $\pm 1\%$. Therefore, it is concluded that the structure of the lung connective tissue, for each phase of respiration, may be approximated by a single atomic composition and density without any loss in dose accuracy.

6.1.3 The accuracy of the Pinnacle^3 CCC dose calculation for different phases of the respiration cycle

To examine the accuracy of CCC dose along the central axis, MC-CT and CCC depth dose curves were plotted and are presented in Fig.6.1. As expected, there appears to be excellent agreement between the curves for normal water (ρ=1.00 g/cm^3). Similarly, the crossplane profiles in Fig.6.2 show that the water MC-CT and CCC dose distributions appear comparable off the central axis.

The percent difference between MC-CT and CCC central axis depth dose curves is presented in Fig.6.6. For the MC-CT/CCC comparison, percent difference was defined as:

$$PD = 100 \times \frac{\mathrm{D}^{(\mathrm{i})}_{\mathrm{CCC}} - \mathrm{D}^{(\mathrm{i})}_{\mathrm{MCCT}}}{\mathrm{D}^{(\mathrm{i})}_{\mathrm{MCCT}}} \tag{6.2}$$

where $\mathrm{D}^{(\mathrm{i})}$ represents the dose in the i^{th} voxel. There is an interesting trend in the percent difference curves. The CCC depth dose curves tend to overestimate the MC-CT curves at the boundary of the lung region. This overestimation reverses with depth until the CCC depth dose values are less than those of MC-CT. The prominence of this overestimation-underestimation trend decreases with both increasing field size and increasing density. As

expected, normal water percent difference values are lowest at approximately $\pm 1\%$ for all field sizes. The ρ=0.30 g/cm^3 curves fall within the prescribed 2% tolerance for field sizes 3x3 to 10x10. However, the 1x1 curves show a percent difference of roughly 6% between depths of 7 and 11 cm. The percent difference between the ρ=0.20 g/cm^3 curves is somewhat poor. Only the 7x7 and 10x10 curves fall within the 2% tolerance. The 1x1, 3x3 and 5x5 curves show percent differences as high as -10, -4 and -3.5% respectively. None of the ρ=0.125 g/cm^3 comparisons fall within 2% of each other. The percent differences for the 1x1, 3x3, 5x5, 7x7 and 10x10 curves plateaued at roughly -15, -8, -7, -6 and -4% respectively. From the percent difference curves, one concludes that agreement between CCC and MC-CT central axis dose curves worsens with decreasing density and/or decreasing field size.

To examine the percent difference between MC-CT and CCC dose distributions off the central axis, inplane and crossplane profiles were calculated at three depths. The three depths correspond to three regions in the depth dose curve of Fig.6.6 (represented by dotted lines). The first depth (3.75 cm) corresponds to a peak in the overestimation of dose by the CCC algorithm. The second depth (9.75 cm) corresponds to a plateau in the underestimation of dose by the CCC algorithm. This plateau is particularly prominent in the 1x1 cm^2 field depth dose curves. The third depth (15.75 cm) corresponds to a second plateau in the underestimation of dose by the CCC algorithm. Upon examination of the percent difference between MC-CT and CCC dose profiles, it was found that there was little difference between inplane (z axis) and crossplane (x axis) percent difference curves. Consequently, only crossplane profiles are presented here. Figures 6.7, 6.8 and 6.9 show the percent difference between MC-CT and CCC crossplane profiles at depths of 3.75, 9.75 and 15.75 cm respectively. The percent difference calculations in the crossplane were restricted to voxels with a dose greater than 80% of the maximum dose along the profile. In the figures, the percent difference along the profiles are relatively constant in the plateau region of the profiles. Towards the shoulder of the profiles, the percent difference increases. This increase becomes more prominent with increasing field size and decreasing density. In general however, the percent difference along the central axis in Fig.6.6 gives a lower limit on the percent difference at that depth.

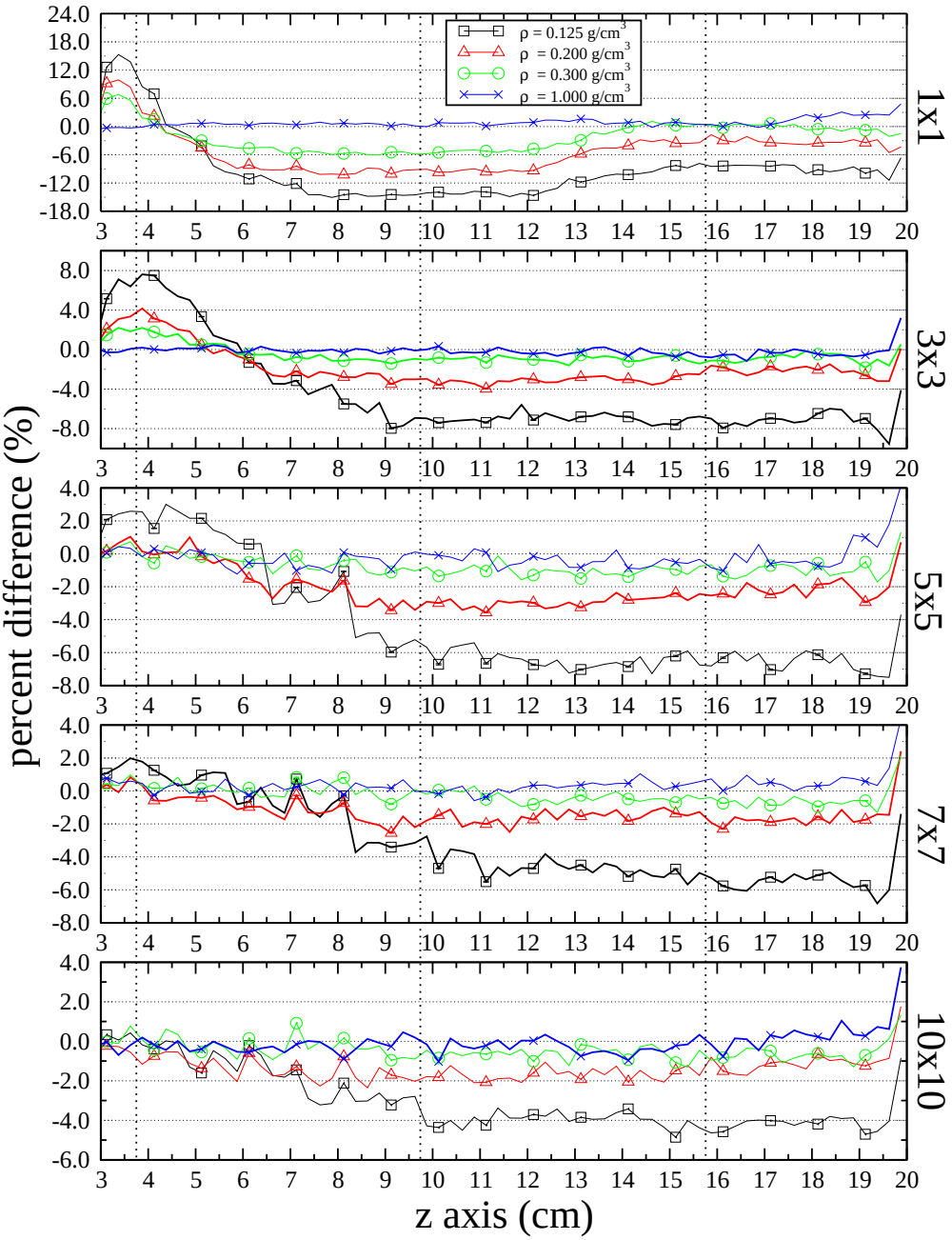

Figure 6.6: Percent difference between MC-CT and CCC depth dose curves for the TISSUE model. The dashed lines indicate the depths at which profiles were calculated. The statistical precision in MC-CT dose values was roughly 0.5%. There was no assigned statistical precision in the CCC dose values.

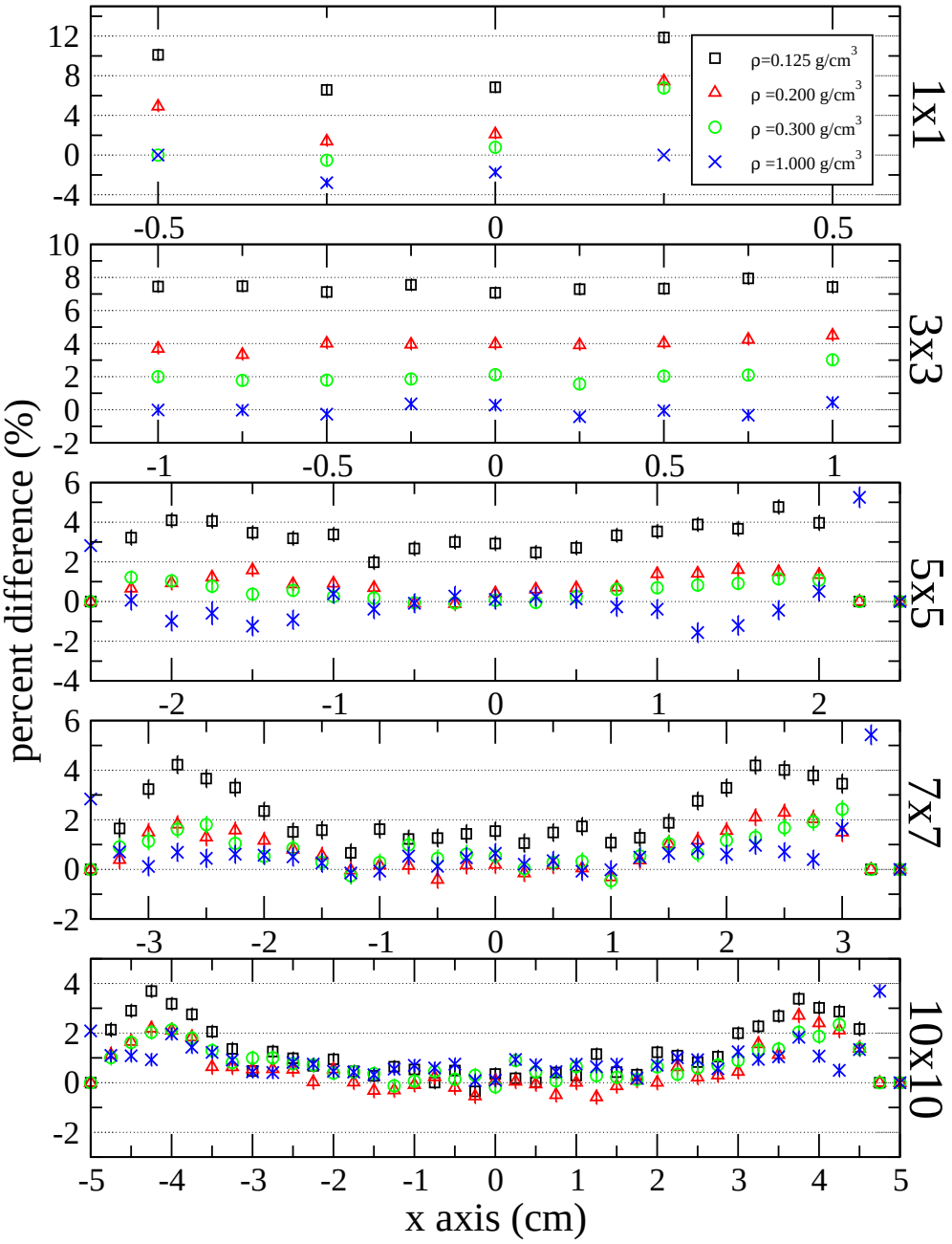

Figure 6.7: Percent difference between MC-CT and CCC crossplane profiles at a depth of 3.75 cm for the TISSUE model. The statistical precision in MC-CT dose values was roughly 0.5%. There was no assigned statistical precision in the CCC dose values.

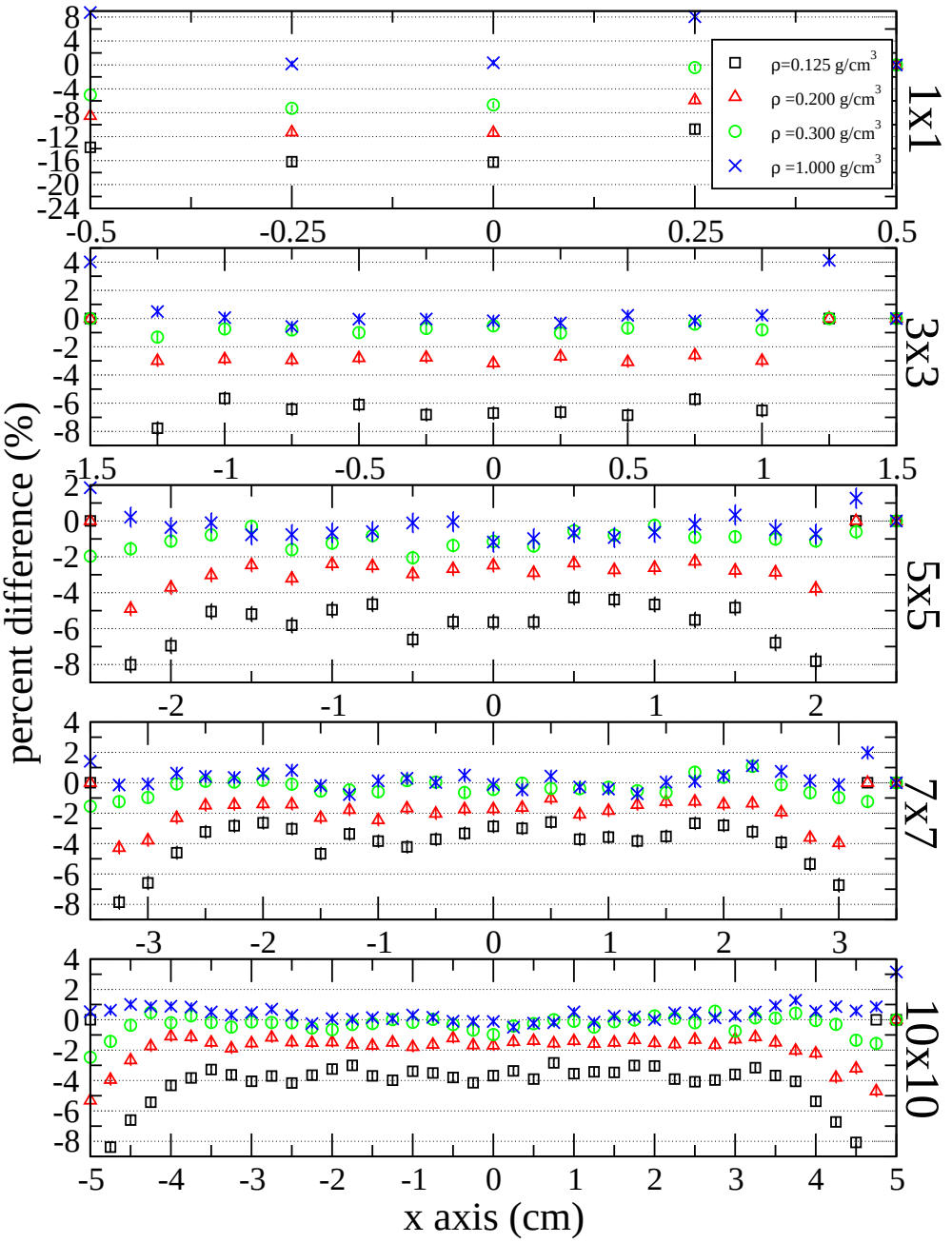

Figure 6.8: Percent difference between MC-CT and CCC crossplane profiles at a depth of 9.75 cm for the TISSUE model. The statistical precision in MC-CT dose values was roughly 0.5%. There was no assigned statistical precision in the CCC dose values.

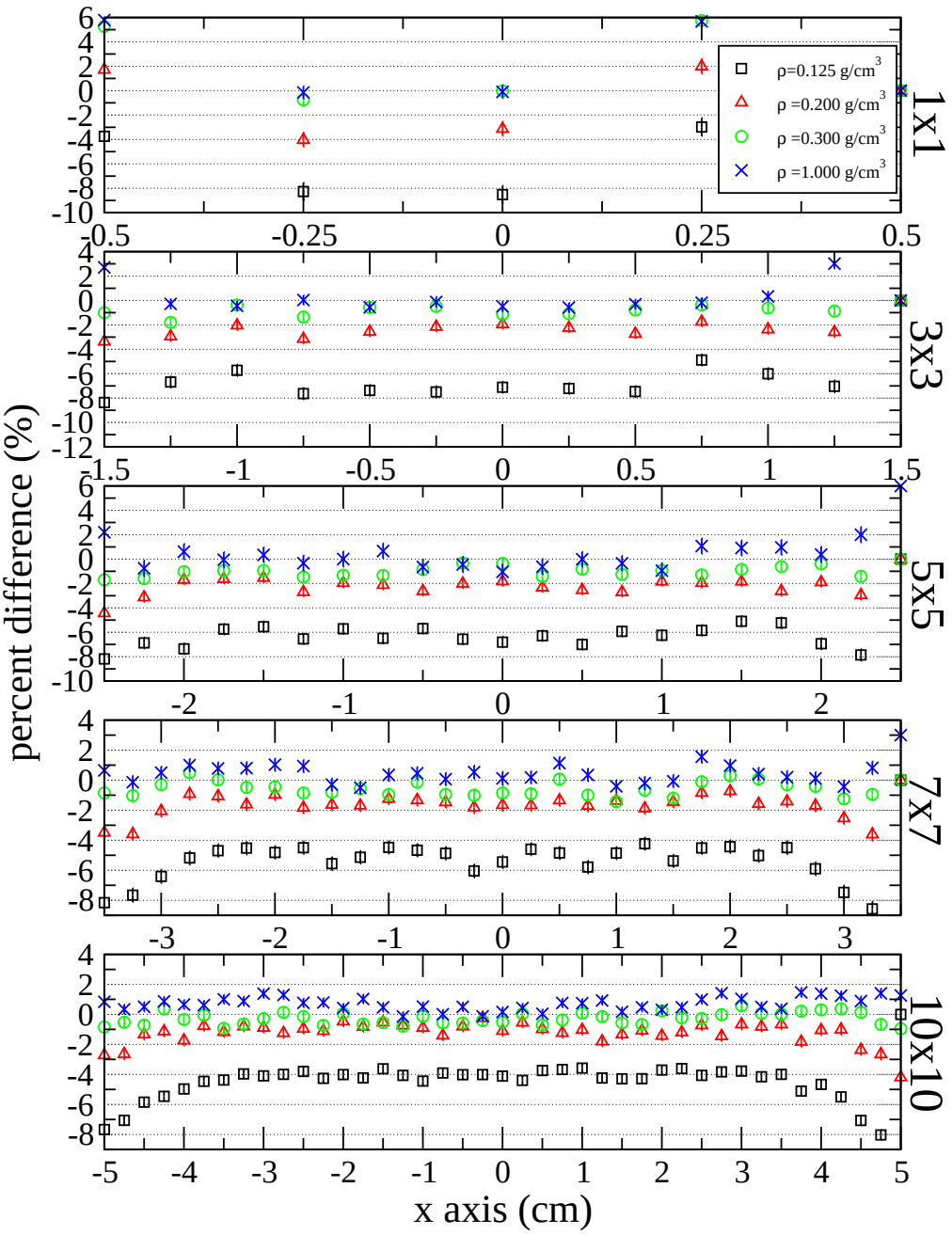

Figure 6.9: Percent difference between MC-CT and CCC crossplane profiles at a depth of 15.75 cm for the TISSUE model. The statistical precision in MC-CT dose values was roughly 0.5%. There was no assigned statistical precision in the CCC dose values.

From figures 6.6-6.9, some general conclusions can be made:

- There is a significant disagreement between MC-CT and CCC dose distributions when lung tissue density is 0.125 g/cm^3.
- Agreement between MC-CT and CCC dose distributions improves with increased field size.
- Agreement between MC-CT and CCC dose distributions improves with increased density.
- Divergence between MC-CT and CCC dose distributions begins to appear below 0.200 g/cm^3.
- The percent difference between the MC-CT and CCC distributions changes with depth.
- The percent difference between the MC-CT and CCC distributions increases with distance off the central axis.

From a clinical point of view, it is concluded that lung dose calculations using the Pinnacle^3 CCC method are most accurate for exhalation densities. From the results presented here, radiation therapy staff should strive to image and treat lung cancer patients at full exhalation lung volumes until discrepancies between MC and CCC dose distributions can be studied further. Also, emphasis should be placed on implementing the more accurate Monte Carlo for treatment planning.

6.2 The BRANCH model

BRANCH model simulations were run according to the setup described in Section 5.4.1. As with the TISSUE model, the following shorthand is used:

1. MC-M: Monte Carlo simulations using the explicit BRANCH model. MC-M simulations transport particles through a series of cylinders and spheres representing the bronchial, arterial and venous networks of the lung. The diameter of individual

branches ranges roughly from 0.2-10mm. MC-M transport in the BRANCH model is non-voxelated.

2. MC-CT: DOSXYZnrc Monte Carlo simulations using the homogeneous CT representation of the BRANCH model. Unlike the MC-M simulations, MC-CT transport is voxelated. Each voxel approximates a region of the BRANCH model as homogeneous in atomic composition and density.

3. CCC: Pinnacle^3 Collapsed Cone Convolution calculations using the CT representation of the BRANCH model. The homogeneous representation of the MC-CT simulations is converted into the Pinnacle^3 CT format and dose distributions calculated using the CCC algorithm.

As in the TISSUE comparisons, a tolerance on the agreement between dose values was set at 2% as recommended in The International Commission on Radiation Units and Measures (ICRU) Report 24 (*ICRU Report 24 : Determination of Absorbed Dose in a Patient Irradiated by Beams of X or Gamma Rays in Radiotherapy Procedures*, 1976).

6.2.1 The effects of structure below the CT/dose resolution on dose accuracy

To determine whether the explicit inclusion of the lung's branching structures below an effective CT/dose resolution of 1 mm x 1 mm x 2 mm had an effect on dose, depth dose curves for three lung densities (0.125, 0.200 and 0.300 g/cm^3), three field sizes (1x1, 3x3 and 5x5 cm^2) and two lung geometry representations (MC-CT and MC-M) were plotted. The results, given in figures 6.10-6.12, illustrate the difference between MC-CT and MC-M results. In the figures, percent difference values for each voxel were calculated according to Eq.6.1. It is clear from the figures that the explicit exclusion of structure below the CT/dose resolution had a measurable effect on the resulting depth dose curves. In particular, there were two depths on the curves where the magnitude in percent difference between MC-CT and MC-M curves increased substantially: -0.7 and 2.9 cm. To correlate BRANCH model structures to deviations in dose, Fig.6.13 provides the position

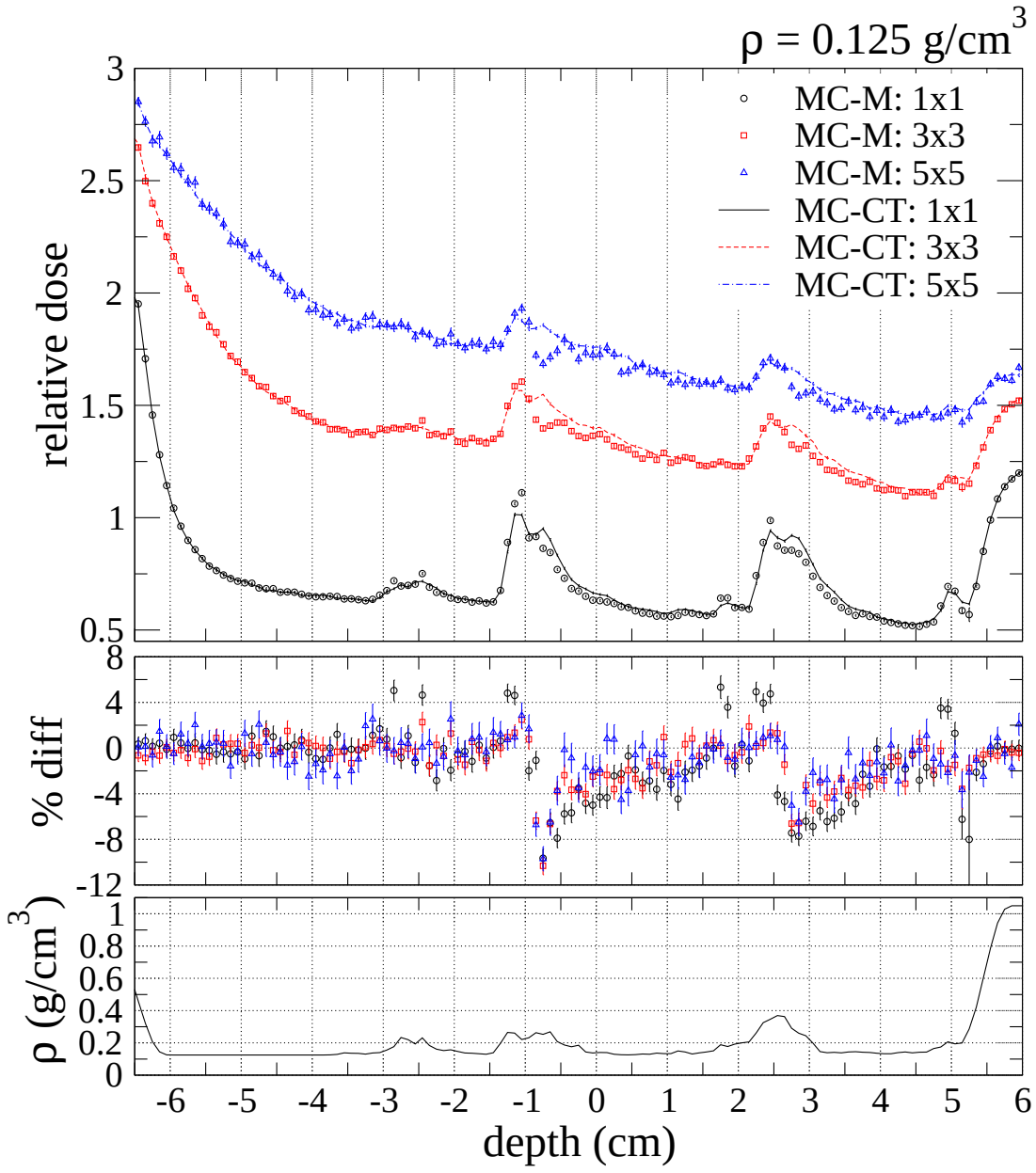

Figure 6.10: Depth dose curves for the BRANCH model (MC-CT vs. MC-M) at a density of 0.125 g/cm^3. In the figure, MC-CT, MC-M are shorthand for Monte Carlo simulation using CT model and Monte Carlo simulation using the explicit BRANCH model. The statistical precision in individual dose values is roughly 0.8%.

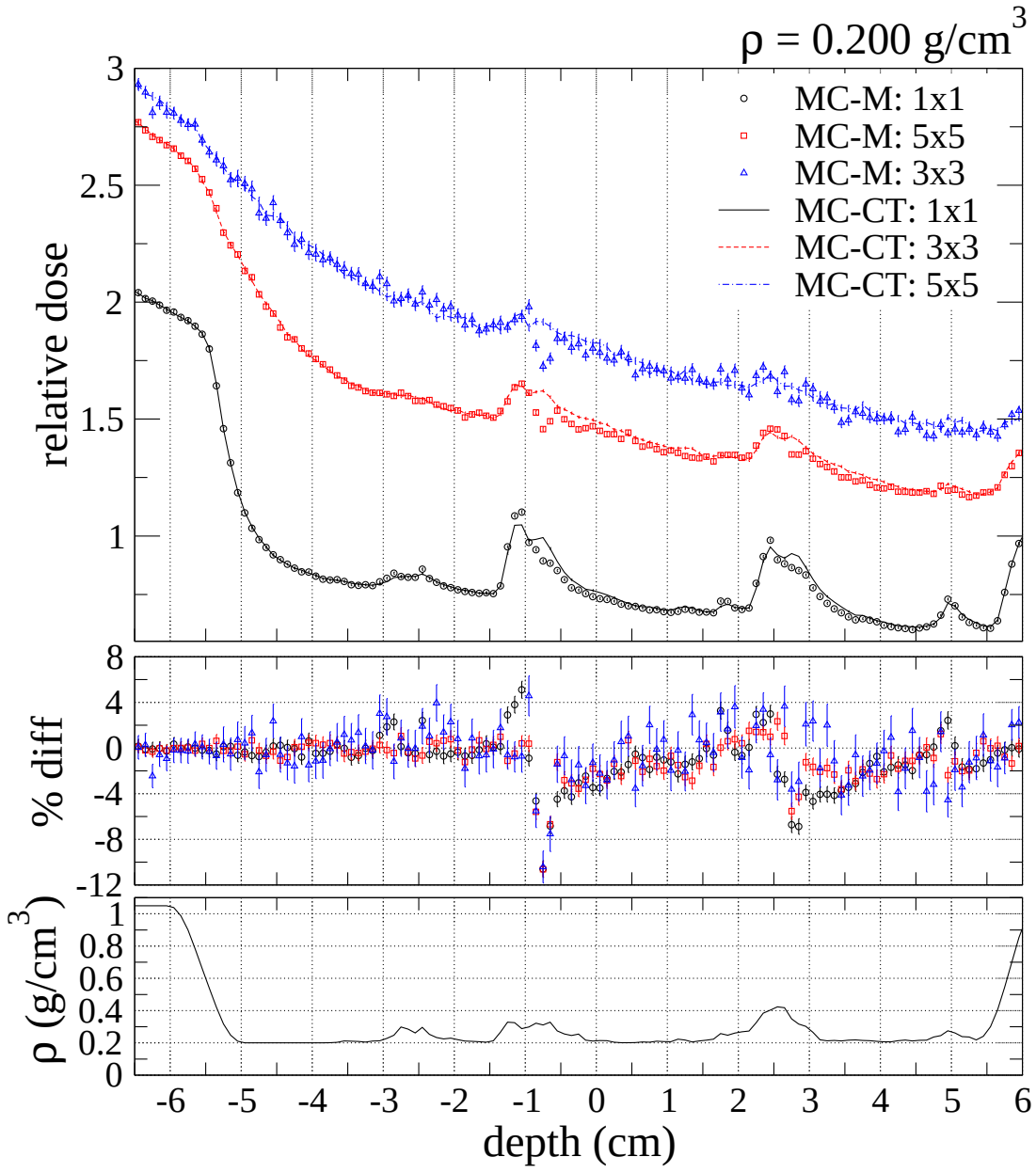

Figure 6.11: Depth dose curves for the BRANCH model (MC-CT vs. MC-M) at a density of 0.200 g/cm^3. In the figure, MC-CT, MC-M are shorthand for Monte Carlo simulation using CT model and Monte Carlo simulation using the explicit BRANCH model. The statistical precision in individual dose values is roughly 0.8%.

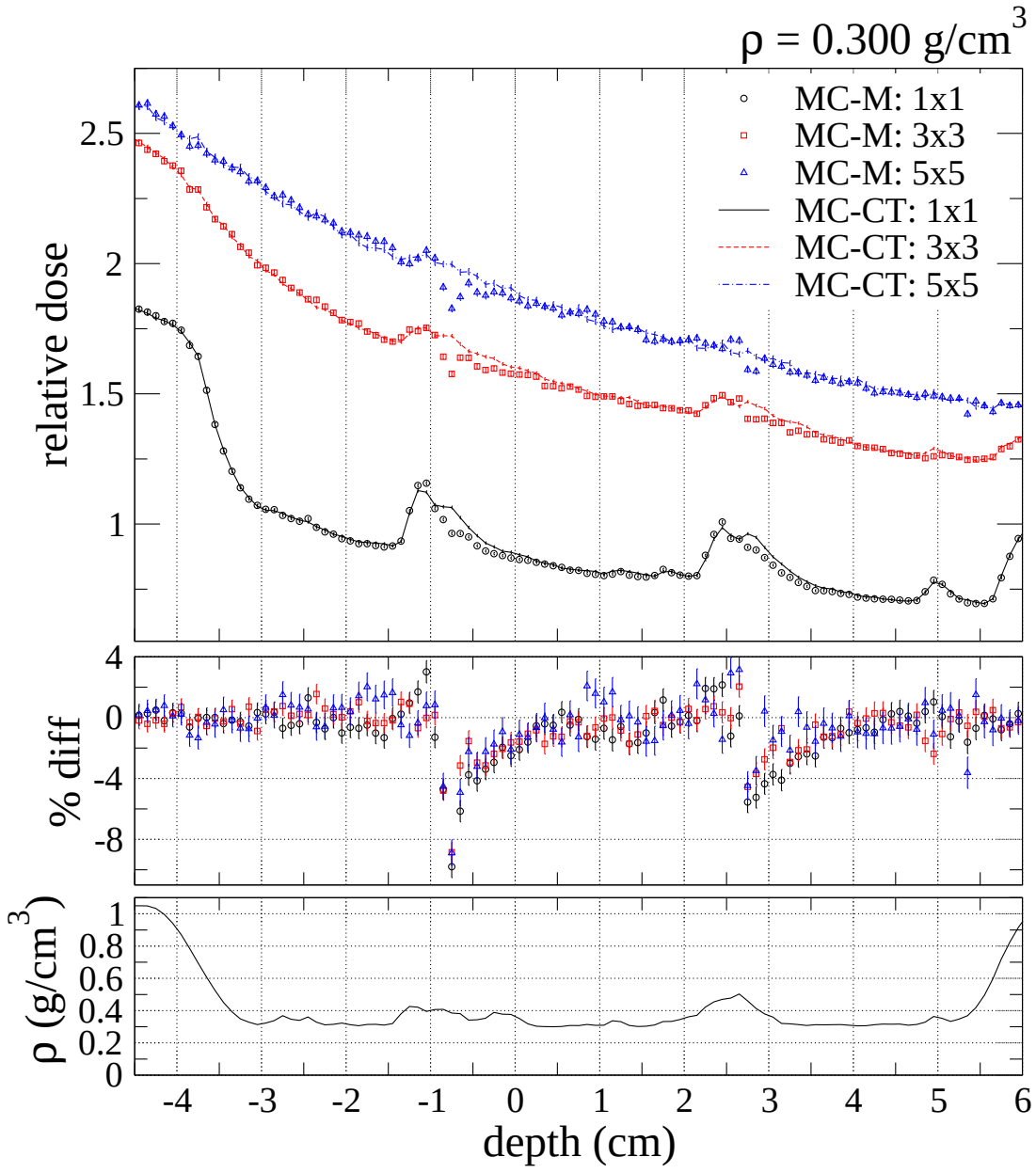

Figure 6.12: Depth dose curves for the BRANCH model (MC-CT vs. MC-M) at a density of 0.300 g/cm^3. In the figure, MC-CT, MC-M are shorthand for Monte Carlo simulation using CT model and Monte Carlo simulation using the explicit BRANCH model. The statistical precision in individual dose values is roughly 0.8%.

and radius of branches closer than 0.5 cm to the central beam axis. At depths of -0.7 and 2.9 cm, bronchial branches with radii greater than 1 mm are present. The presence of these bronchial branches provide large air paths which allow electrons to go far from the initial interaction site. Also, bronchial branches appear to effect the central axis dose when their radii are on the order of the voxel size. Smaller bronchial branches along the central axis do not seem to create large differences in dose.

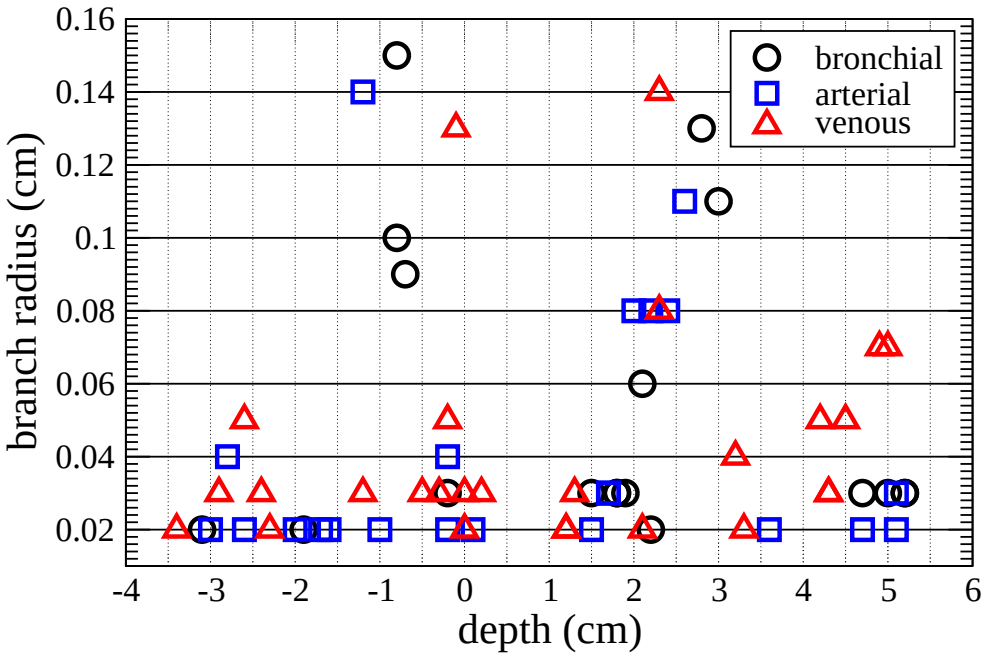

Figure 6.13: The branches along the cental beam axis of a BRANCH simulation.

In figures 6.10-6.12, MC-M dose was roughly 10% lower than that of MC-CT for all field sizes at a depth of -0.7 cm along the central axis,. At a depth of 2.9 cm, there was a small decrease in the magnitude of percent difference as a function of increasing density. For the 0.125 g/cm^3 simulations, regardless of field size, the MC-M dose was roughly 7-8% low compared to that of MC-CT. For the 0.200 g/cm^3 simulations, the underestimation in dose improved to 7%, 6% and 4% for the 1x1, 3x3 and 5x5 fields respectively. For the 0.300 g/cm^3 simulations, the underestimation for the 1x1 cm^2 field simulation improved to 6% while the 3x3 and 5x5 cm^2 MC-M dose values were both 5% low. A definitive

trend in percent difference as a function of field size was difficult to quantify due to the large uncertainty in the percent difference values (propagated from the uncertainties in dose). To decrease the uncertainty in dose, all distributions were re-scaled. The resulting distributions contained voxels 2 mm x 2 mm x 2mm in dimension. These distributions were used in the subsequent analysis.

To further explore the accuracy of the MC-CT dose distributions, crossplane and in-plane profiles at the two depths were extracted and are presented in figures 6.14 and 6.15. In the figures, it is shown that the MC-M dose values at the two depths are typically 8-14% lower than those of MC-CT. There is no particular trend in the percent difference values as a function of field size or lung tissue density. In addition, the peak in percent difference for all three field sizes and densities is located at the same point in space. This localized percent difference increase must be due to the explicit inclusion of branching structures in the MC-M representation of the BRANCH model.

There is a significant decrease in MC-CT dose accuracy proximal to branching structures at the two depths. However to explore how the MC-CT dose distributions compare to MC-M dose distributions over the lung volume, the percent difference as a function of volume was calculated and is given in Fig.6.16. The sample volume included all scoring voxels with dose values greater than 80% of the maximum dose at the same depth that were within the boundary of the BRANCH model. From the figure, it appears that the MC-CT and MC-M dose distributions are within tolerance over much of the sample volume. The peak percent difference for each comparison is centered around zero. This is confirmed in Table 6.2 which presents the mean percent difference and sample deviation for each distribution. In Table 6.2, the sample deviations are somewhat large. Also, the sample deviations appear to decrease with increasing density. However, the increase in sample deviation is likely due to a decrease in energy depositing events.

In summary:

- The presence of branching structures had a substantial effect on the resulting dose distribution.

- The perturbation in dose due to the branching structures is localized around the

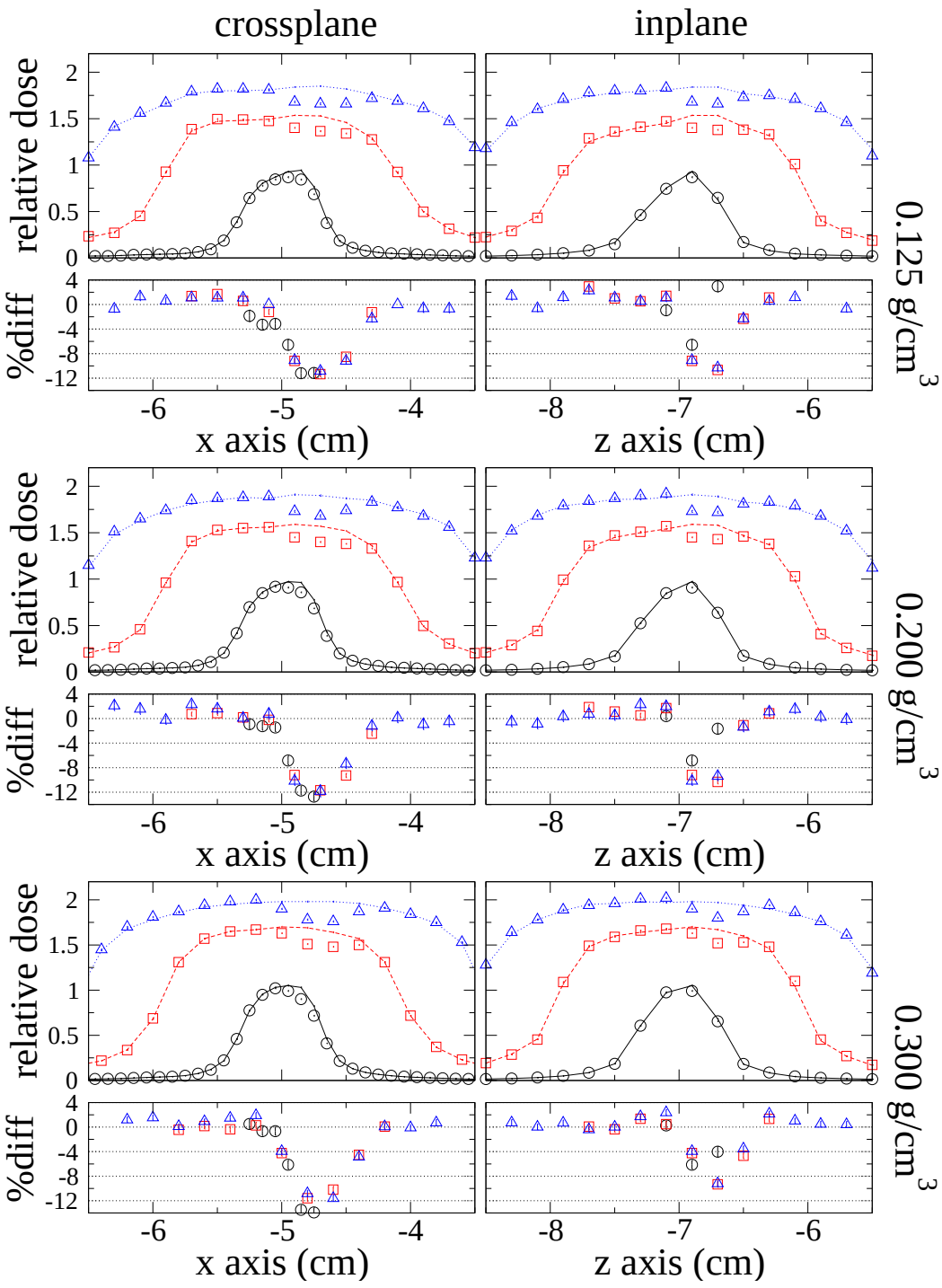

Figure 6.14: Crossplane/inplane profiles for the BRANCH model (MC-CT (lines) vs. MC-M (symbols)). Profiles are shown at depth of -0.7 cm. Refer to Fig.6.10 for legend. Crossplane profiles are along the x axis while inplane profiles are along the z axis. The statistical precision in individual dose values is roughly 0.8%.

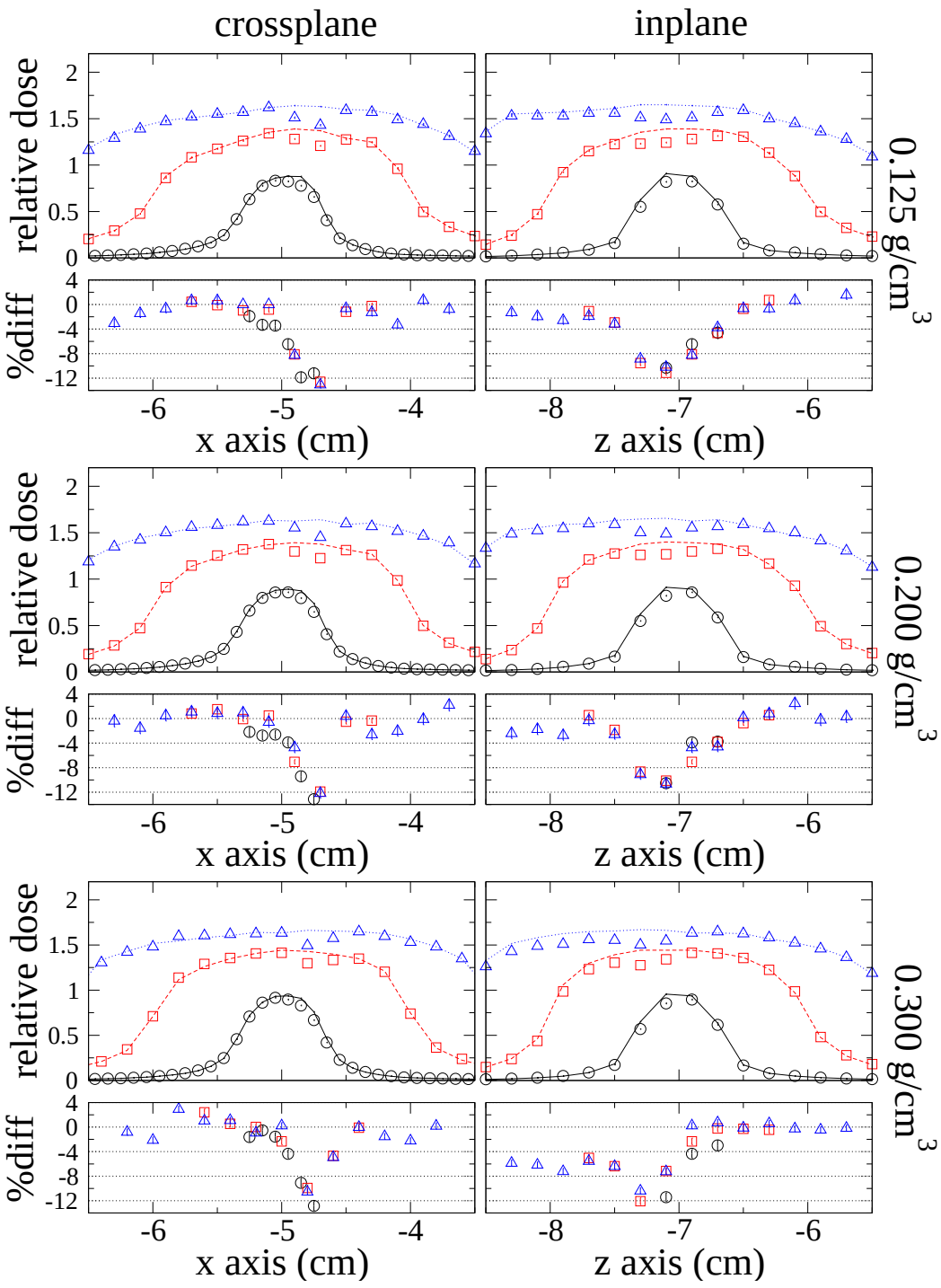

Figure 6.15: Crossplane/inplane profiles for the BRANCH model (MC-CT (lines) vs. MC-M (symbols)). Profiles are shown at depth of 2.9 cm. Refer to Fig.6.10 for legend. Crossplane profiles are along the x axis while inplane profiles are along the z axis. The statistical precision in individual dose values is roughly 0.8%.

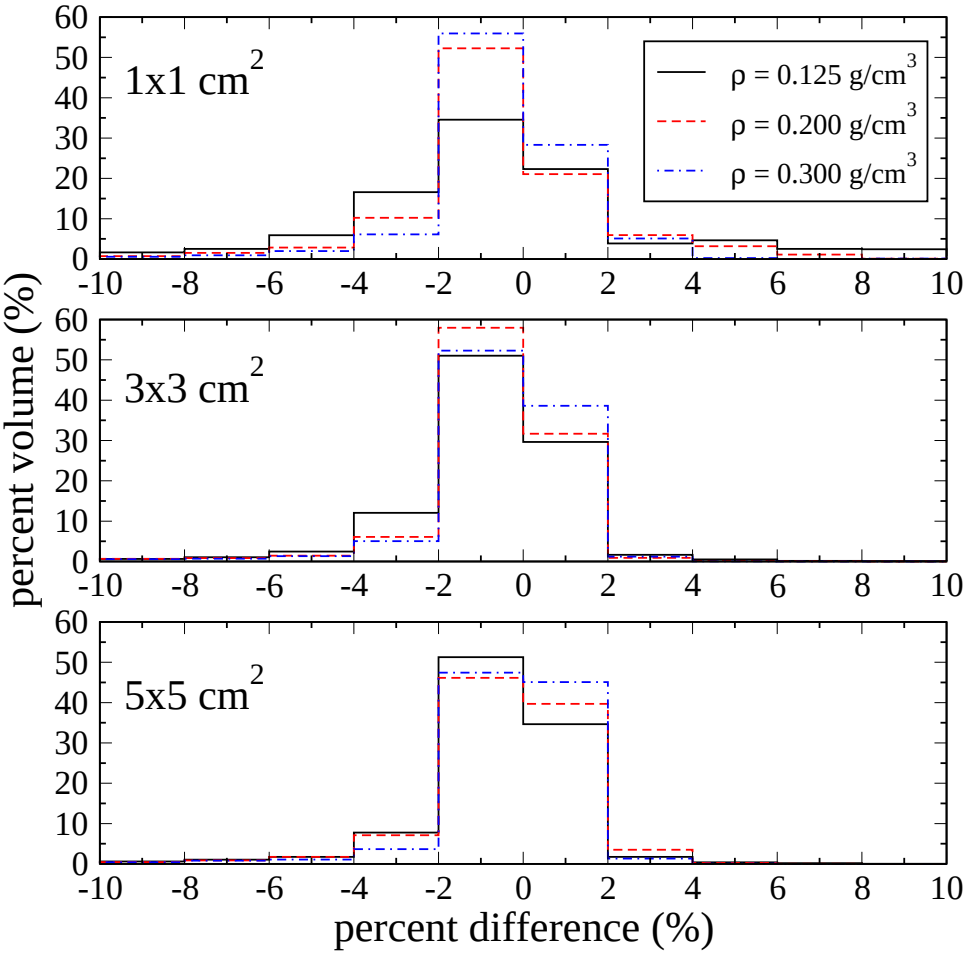

Figure 6.16: Percent difference vs. percent volume between the MC-CT and MC-M BRANCH dose distributions: The percent difference was calculated for voxel pairs with dose values greater than 80% of the central axis dose at equal depth.

Table 6.2: Mean Percent Difference between MC-CT and MC-M BRANCH simulations as a function of lung density and field size. There were approximately 1,000, 3,200 and 9,000 sample voxels for the 1x1, 3x3 and 5x5 distributions respectively. The uncertainty in the percent difference (propagated from uncertainty in dose) was roughly 0.8%. The uncertainty in the mean percent difference was less than 0.03%.

Density	Mean Percent Difference $\pm$ Sample Deviation (%)		
g/cm^3	1x1	3x3	5x5
0.125	-0.30$\pm$5.54	-0.76$\pm$2.38	-0.58$\pm$4.31
0.200	-0.51$\pm$2.74	-0.58$\pm$1.56	-0.35$\pm$2.00
0.300	-0.50$\pm$2.23	-0.43$\pm$1.52	-0.23$\pm$1.57

offending structures.

- There is an increase in the perturbation effect with decreasing density.
- The perturbation is likely the result of localized regions of electronic disequilibrium near interfaces of contrasting atomic compositions and densities (i.e air-tissue, tissue-lung).

The preceding results indicate that the MC-CT BRANCH model is not an accurate representation of the transport environment. The differences between the MC-M and MC-CT dose distributions may be caused by the assignment of a single atomic composition and density to the voxels of the MC-CT calculations. The structures of the lung yield boundaries with largely contrasting atomic compositions and densities (air-tissue, lung-tissue etc...). These contrasting boundaries produce localized regions of electronic disequilibrium. When these boundaries are averaged into a single composition and density, the low density portion of the volume that produces the disequilibrium is removed or distorted. Further, the assignment of a single atomic composition and density implies that the spread of energy within a voxel volume is the same in all directions. It will be proven in the following example that this is not the case.

A set of slab phantoms were created, each with a dimension of 3 cm x 3 cm x 3 cm.

The voxel size was 2 mm x 2 mm x 2 mm for all phantoms. Each phantom was composed of normal water (ρ=1.00 g/cm^3, H2O700ICRU) except for a single slab layer at a depth of roughly 2.0 cm. The slab layer, which was one voxel thick, was made to represent half density water (ρ=0.50 g/cm^3). The voxels of the slab layer were defined in three different ways (see Fig.6.17): (1) a solid homogeneous voxel, (2) two equivalent horizontal slabs composed of normal water and air respectively and (3) two equivalent vertical slabs composed of normal water and air respectively. For each setup, a simple, parallel, monoenergetic, 2 MeV x-ray beam was placed incident on the geometry, perpendicular to the slabs.

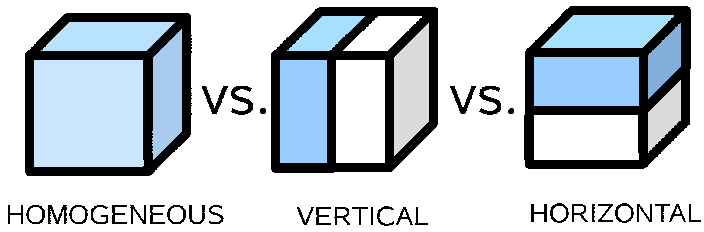

Figure 6.17: Defining the voxel layer: The voxels of the half density slab layer were defined in three different ways: (1) a solid homogeneous voxel, (2) two equivalent horizontal slabs composed of normal water and air respectively and (3) two equivalent vertical slabs composed of normal water and air respectively. Simulations were carried out for a voxel dimension of 2 mm^3.

The depth dose curves for the slab simulations are presented in Fig.6.18. In the figure, the dose within the slab is dependent on the atomic composition/density distribution within each voxel. Specifically, the horizontal and vertical dose values at the slab interface were lower than the homogeneous values by -9.4$\pm$0.5 and -6.6$\pm$0.5% respectively. This illustrates the importance of explicitly representing the distribution of density within a voxel when calculating dose.

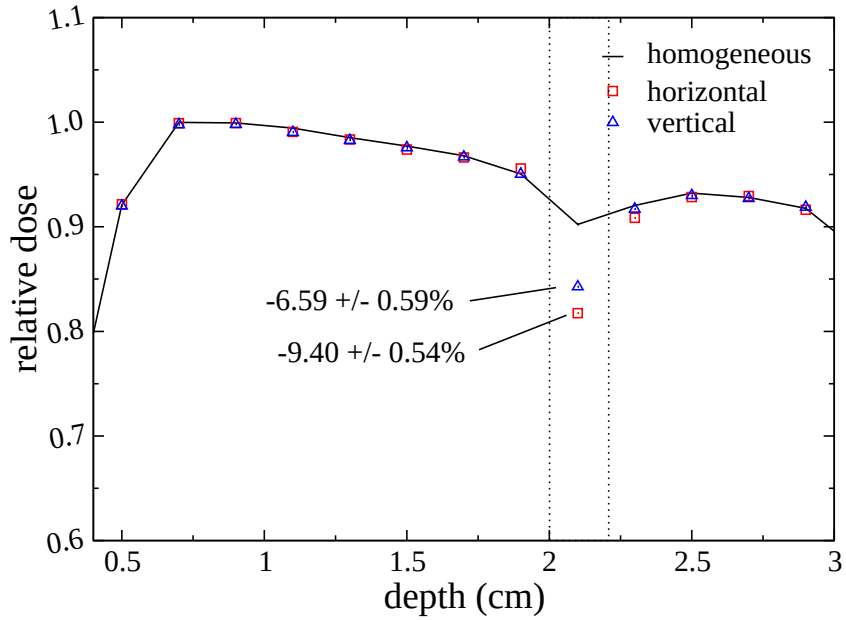

Figure 6.18: The effects atomic composition and density distribution on dose. The magnitude of dose in a 0.5 g/cm^3 slab depends on the density distribution within the voxel (homogeneous, horizontal or vertical representation).

6.2.2 The effects of structural variation due to respiration on dose accuracy

As discussed in the previous section, there is a subtle trend towards decreased dose accuracy as a function of decreasing density (increasing respiratory volume). Table 6.2 shows a gradual increase in both the mean percent difference and sample deviation as a function of decreasing density. The results indicate that the most accurate dose calculations are performed for maximal exhale CT images. It should be noted however that, the accuracy of midbreath dose calculations are not significantly worse than the maximal exhale case. Regardless, until dose calculation accuracy is improved for all phases of respiration, patient imaging should be performed at the lowest achievable lung volume.

6.2.3 The accuracy of the Pinnacle^3 CCC dose calculation for different phases of the respiration cycle

To explore the accuracy of the Pinnacle^3 CCC dose algorithm within the BRANCH model geometry, the percent depth dose curves for the MC-CT and CCC BRANCH model simulations were extracted and are presented in figures 6.19-6.21. It should be noted here that the MC-CT simulations of this section are not the same as those of Section 6.2.1. For section 6.2.1, the distance of the source from the isocenter was incorrectly set. Unfortunately this placed the beam source inside the phantom. Placing the source inside the phantom is not allowed for Pinnacle^3 calculations. Since it was not practical (due to simulation runtime) to re-run the MC-M calculations at a properr source-to-isocenter distance, MC-CT calculations were performed twice. For the MC-M/MC-CT comparison, the source was left inside the phantom for the simulations. For the MC-CT/CCC comparison, the source was placed at the surface of the phantom. This corresponded to a source-to-surface distance of 90 cm.

Included in figures 6.19-6.21 are the central axis percent difference curves which were calculated according to Eq.6.2. There is a sharp increase in the percent difference value at a depth of -1.0 cm. For all lung densities, and field sizes, the CCC algorithm underestimates

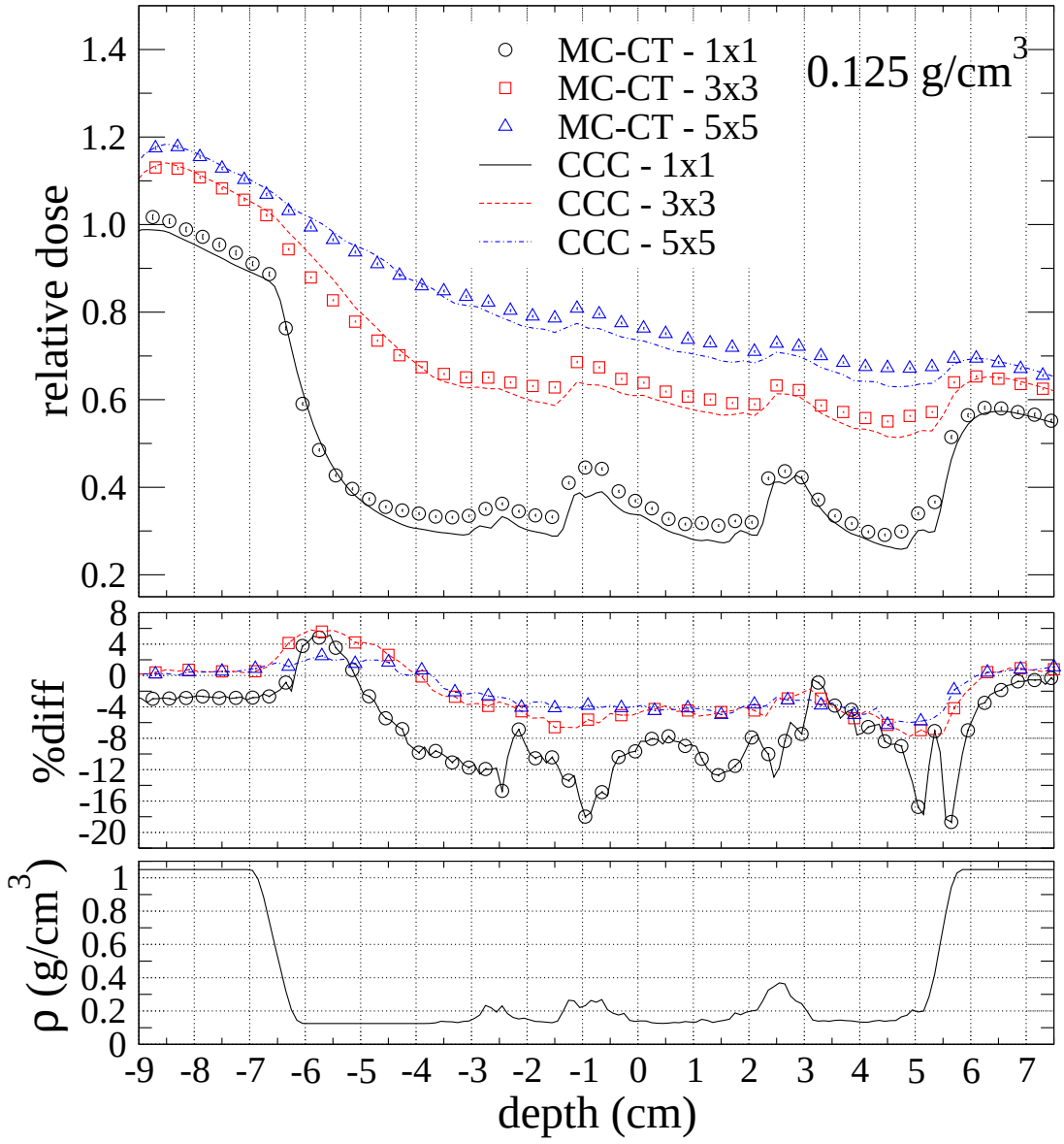

Figure 6.19: MC-CT and CCC depth dose curves for the BRANCH model at 0.125 g/cm^3. The statistical uncertainty in the MC-CT dose calculations was roughly 0.3%. There is no uncertainty assigned to the CCC dose distributions.

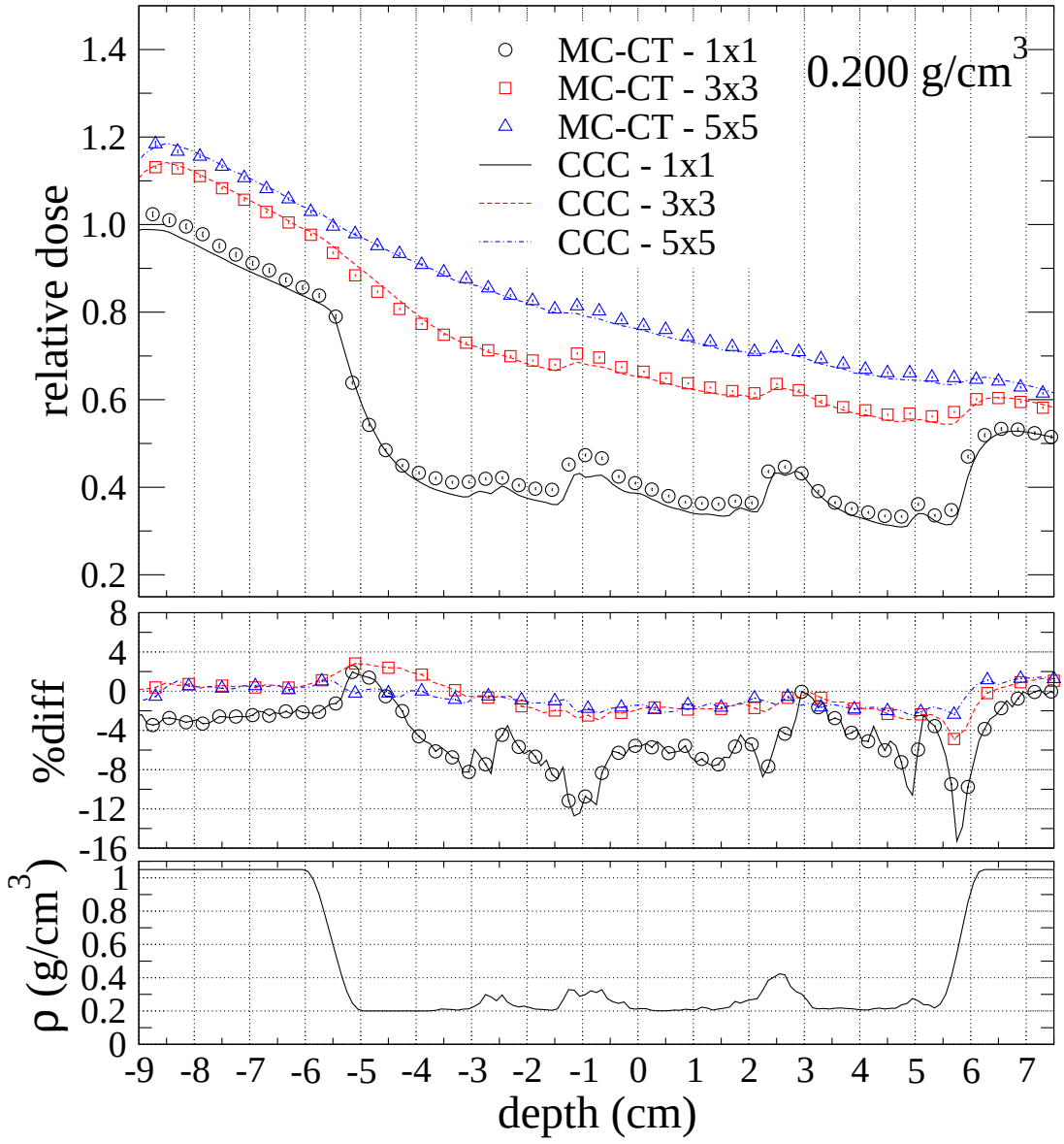

Figure 6.20: MC-CT and CCC depth dose curves for the BRANCH model at 0.200 g/cm^3. The statistical uncertainty in the MC-CT dose calculations was roughly 0.3%. There is no uncertainty assigned to the CCC dose distributions.

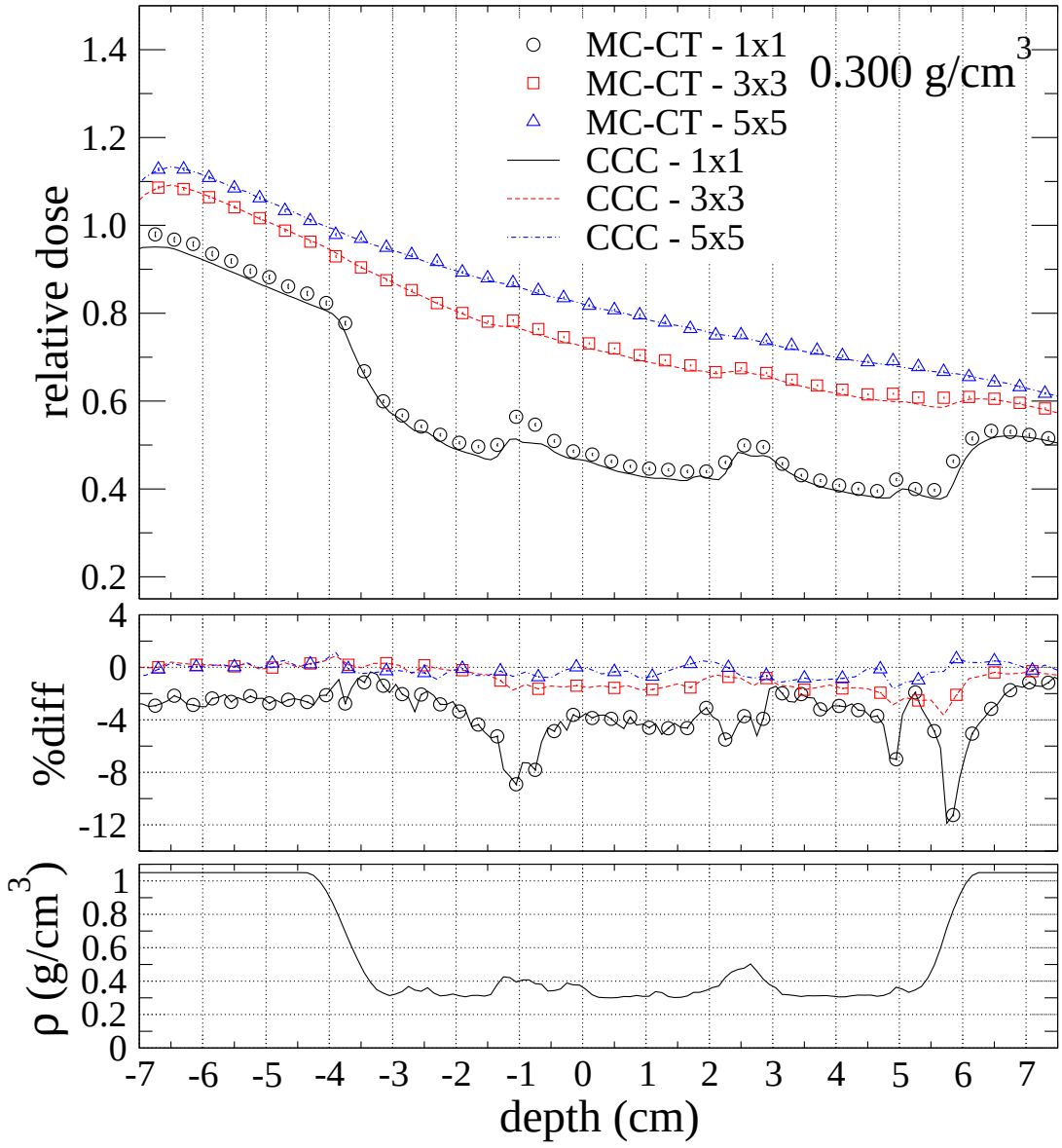

Figure 6.21: MC-CT and CCC depth dose curves for the BRANCH model at 0.300 g/cm^3. The statistical uncertainty in the MC-CT dose calculations was roughly 0.3%. There is no uncertainty assigned to the CCC dose distributions.

dose at this depth. However, the magnitude in percent difference decreases with both increasing lung density and increasing field size. At a density of 0.125 g/cm^3, the 1x1, 3x3 and 5x5 cm^2 CCC dose values underestimate the MC-CT dose values by 18, 7 and 4% respectively. At a density of 0.200 g/cm^3, the magnitude of these percent difference values are reduced to 12, 3 and 2%. At a density of 0.300 g/cm^3, the magnitude of the percent differences are reduced further to 8.5, 2 and 1%.

The crossplane and inplane profiles at a depth of -1.0 cm are presented in figures 6.22 and 6.24. The percent difference between the MC-CT and CCC profiles are given in figures 6.23 and 6.25. The percent difference calculation was restricted to voxels with a dose greater than 80% of the maximum dose at the same depth. Generally, the percent differences of the PDD curves at this depth correspond to the maximum percent difference in the crossplane/inplane profiles. It can be seen in both figures that the agreement between CCC and MC-CT profiles improves with increasing field size and increasing density.

In the same manner as the MC-CT vs MC-M comparison, the percent difference between MC-CT and CCC distributions was plotted as a function of volume (see Fig.6.26). The mean percent difference and sample deviation of each curve in the figure is presented in Table 6.3. It is clear from the table that for a density of 0.300 g/cm^3 and a field size greater than or equal to 3x3 cm^2, the MC-CT and CCC dose distributions are in good agreement. The same is true for the 0.200 g/cm^3 curves with the added observation that the sample deviation is large. Percent difference values are unacceptably high for both the smallest field size and smallest density. As was discussed in the TISSUE model section, the large dose differences for the 1x1 cm^2 field is likely due to insufficient modeling of the Monte Carlo and/or Pinnacle^3 beam. Better benchmarking procedures are needed for the creation of small field Monte Carlo and Pinnacle^3 linac source models. Fortunately, fields as small as 1x1 cm^2 are seldom used in conventional 3D-CRT treatments.

In summary, the results of the BRANCH MC-CT vs CCC comparison echo the conclusions of the TISSUE model comparison:

- There is significant disagreement between MC-CT and CCC dose distributions when lung tissue density is 0.125 g/cm^3.

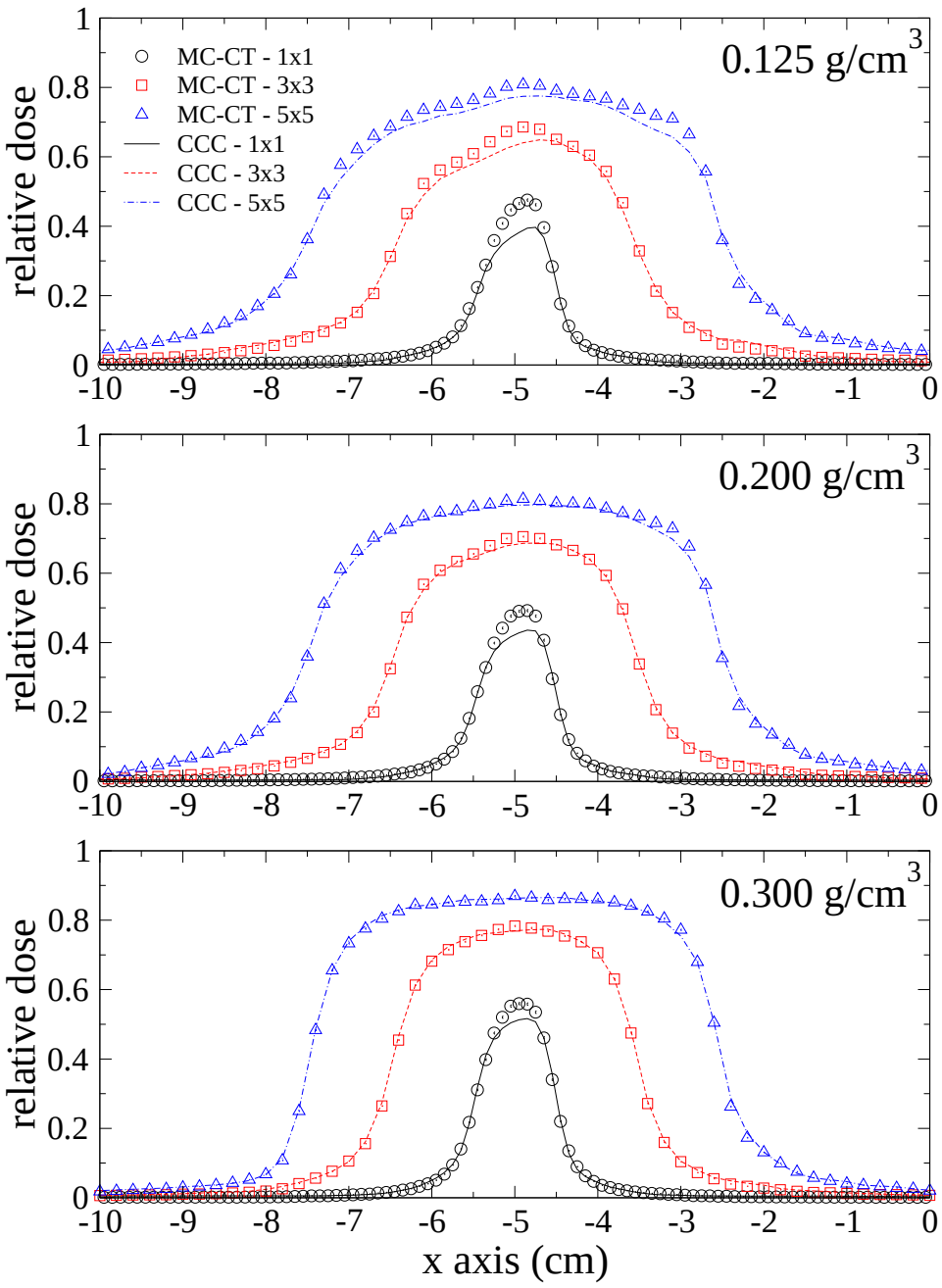

Figure 6.22: MC-CT and CCC crossplane profiles at a depth of -1.0 cm for the BRANCH model. The crossplane profiles are along the x axis. The uncertainty in the MC-CT dose values was roughly 0.3%. There is no uncertainty assigned to the CCC dose distributions.

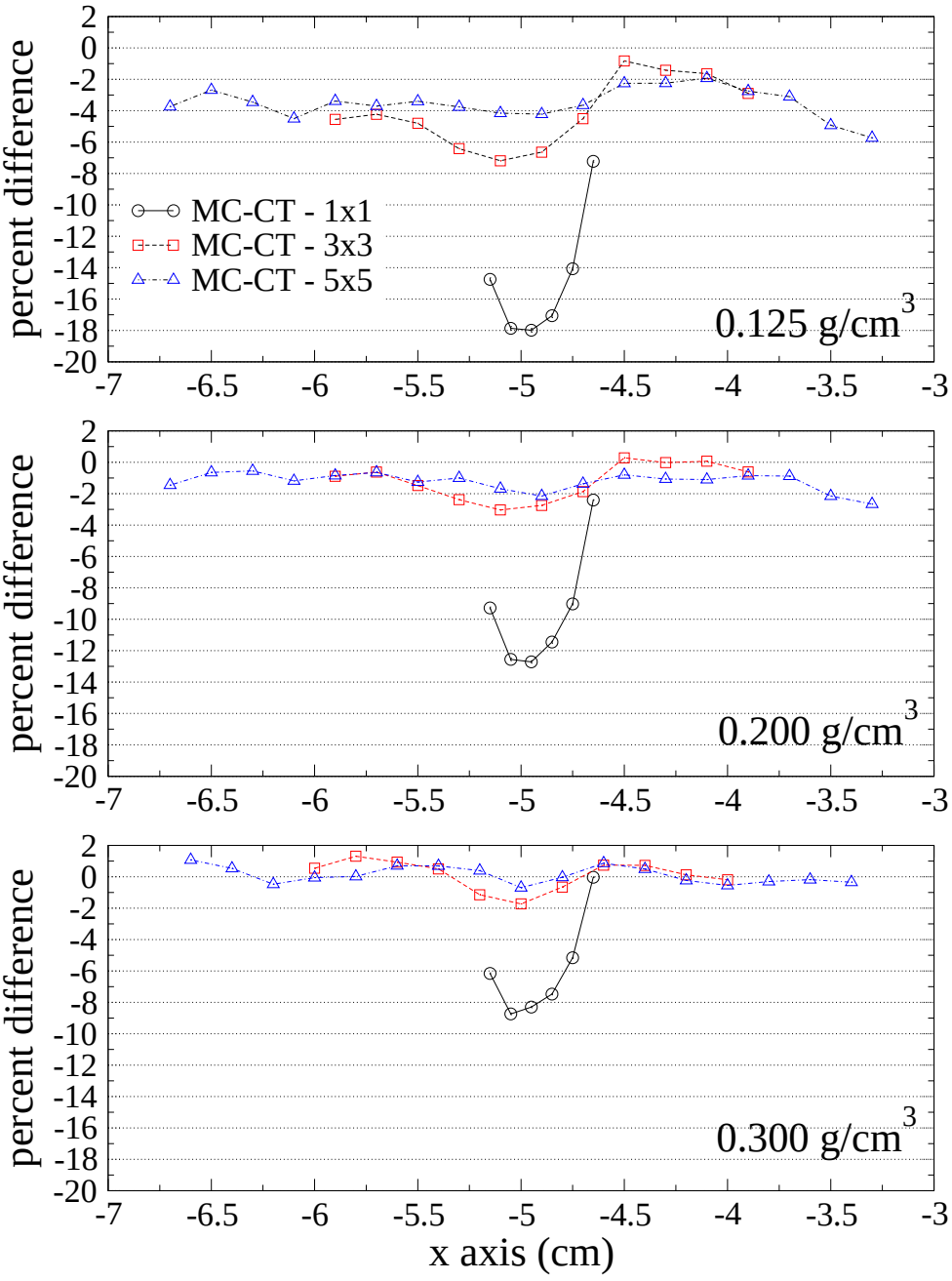

Figure 6.23: Percent difference between MC-CT and CCC crossplane profiles at a depth of -1.0 cm for the BRANCH model.

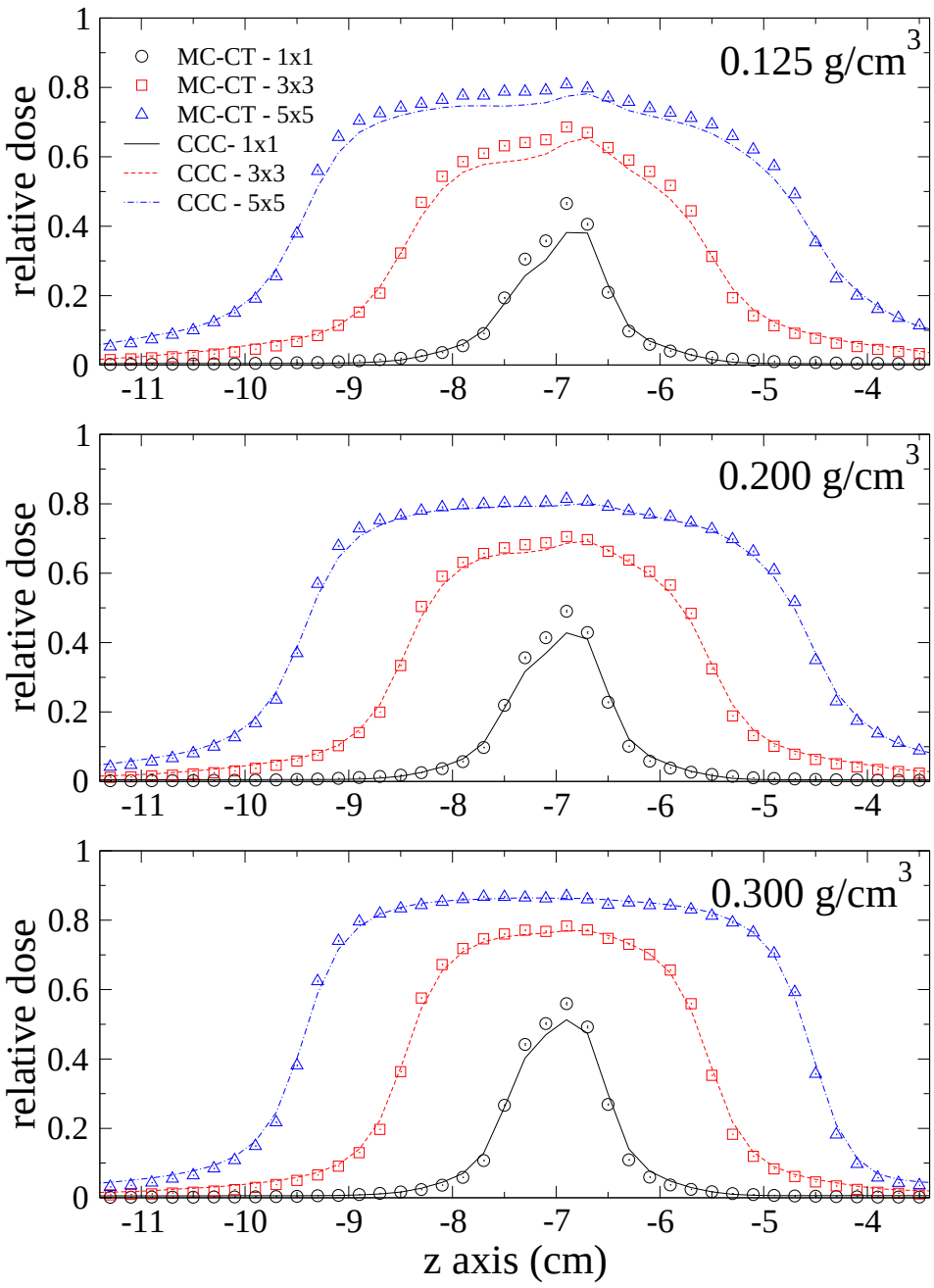

Figure 6.24: MC-CT and CCC inplane profiles at a depth of -1.0 cm for the BRANCH model. The inplane profiles are along the z axis. The uncertainty in the MC-CT dose values was roughly 0.3%. There is no uncertainty assigned to the CCC dose distributions.

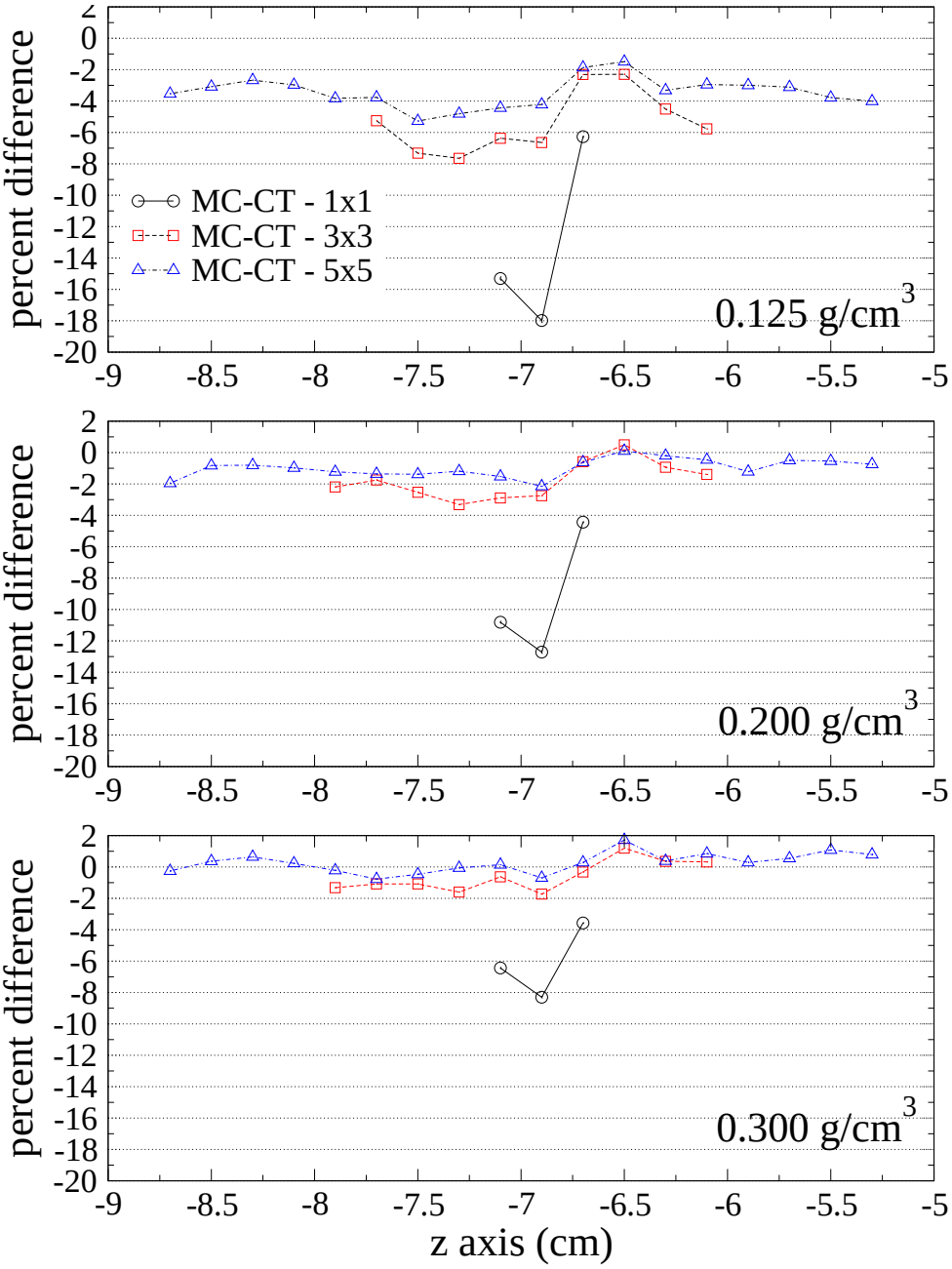

Figure 6.25: Percent difference between MC-CT and CCC inplane profiles for the BRANCH model. The uncertainty in the MC-CT calculations was roughly 0.3%. There was no uncertainty assigned to the CCC calculation.

- Agreement between MC-CT and CCC dose distributions improves with increased field size.
- Agreement between MC-CT and CCC dose distributions improves with increased density.
- Divergence between MC-CT and CCC dose distributions begins to appear below 0.200 g/cm^3.
- The Pinnacle^3 and BEAMnrc beam models must be benchmarked against small field measurements.

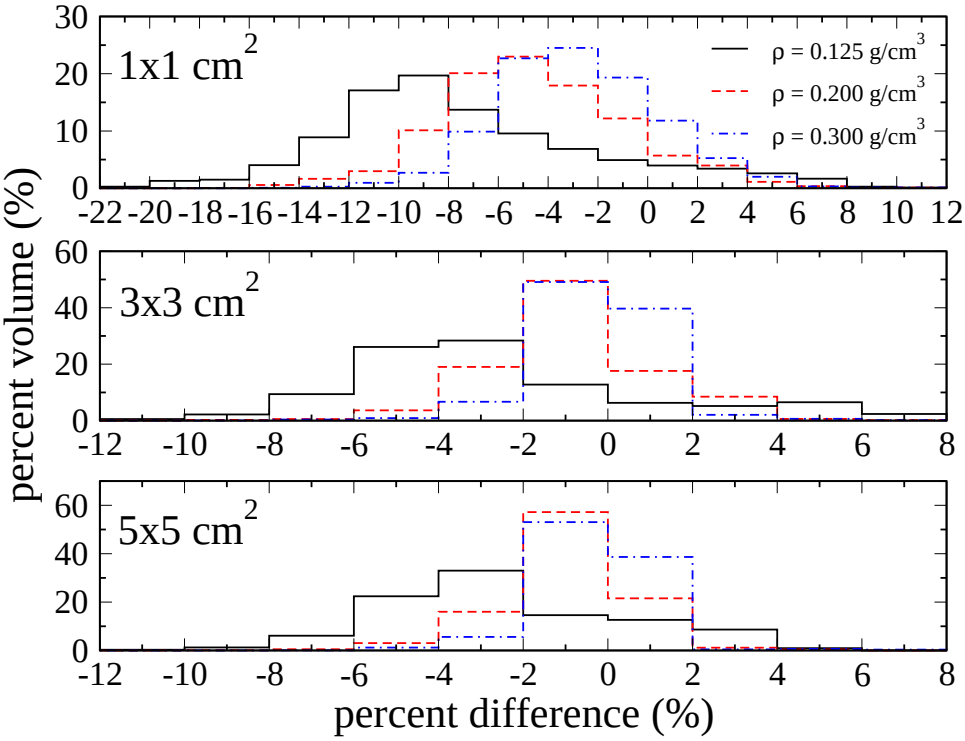

Figure 6.26: Percent difference vs. percent volume between the MC-CT and CCC dose distributions for the BRANCH model: The percent difference was calculated for voxel pairs with dose values greater than 80% of the central axis dose at equal depth.

Table 6.3: Mean Percent Difference between MC-CT and CCC BRANCH simulations as a function of lung density and field size. There were approximately 2,800, 7,500 and 24,000 sample voxels for the 1x1, 3x3 and 5x5 distributions respectively. The uncertainty in the percent difference (propagated from uncertainty in dose) was roughly 0.3%. The uncertainty in the mean percent difference was less than 0.005%.

Density	Mean Percent Difference $\pm$ Sample Deviation (%)		
g/cm^3	1x1	3x3	5x5
0.125	-7.25$\pm$5.53	-2.52$\pm$3.67	-2.41$\pm$2.89
0.200	-4.47$\pm$3.78	-0.85$\pm$1.97	-0.99$\pm$1.53
0.300	-2.74$\pm$3.26	-0.23$\pm$1.46	-0.29$\pm$1.24

CHAPTER 7

DISCUSSION

An important distinction must be made between the CT resolutions used in this thesis and the CT resolutions achievable with modern scanners. A clinical CT scanner can resolve anatomic detail to a much higher resolution than the 1mm x 1mm x 2mm used in this thesis. For example, the GE Lightspeed^{TM}RT^{16} CT scanner (GE Healthcare, Milwaukee WI USA) used at the Saskatoon Cancer Center can achieve a scan resolution of 0.100 mm x 0.100 mm x 0.625 mm. However, this resolution is only possible within a 10 cm x 10 cm field of view in the transverse plane. The limitation on the field of view is due to the finite amount of computer memory available. For treatment planning, it is usually necessary to capture the entire anatomy in the transverse plane. To do so, it is necessary to capture a field of view of 50 cm x 50 cm. Since the computer memory available is finite, the CT resolution must be reduced to 0.5mm x 0.5mm x 0.625mm. The Pinnacle^3 treatment planning system at our institution is only capable of handling half of this data in the transverse plane (32 vs 64 bit). Therefore CT resolution used for treatment planning is limited to about 1 mm x 1 mm x 0.625 mm. To achieve reasonable dose calculation times, the Pinnacle^3 dose grid at the Saskatoon Cancer Center is typically set at 3 mm x 3 mm x 3 mm. To perform the dose calculation, the CT image must be further unresolved to match the dose grid. For Monte Carlo calculations, the CT/dose resolutions used in this thesis (1 mm x 1 mm x 2 mm and 2.5 mm x 2.5 mm x 2. 5mm) yielded long dose computation times. A higher voxel resolution would have increased computation times to unrealistic lengths (weeks to months) and decreased the statistical uncertainty in the results. The CT/dose resolution used was a compromise between the smallest effective CT/dose resolution that can be input into the planning system, and the practical CT/dose resolution used to calculate Monte Carlo dose within a reasonable time.

For the TISSUE model, the explicit inclusion of the connective tissue structures of the lung did not introduce a significant change in the resulting dose distributions (less than a 1% change). This conclusion was true regardless of phase of respiration (tissue density). However it should be noted that, the TISSUE model is only an approximation of lung tissue. As outlined in Chapter 5, the alveoli walls of the TISSUE model were made thicker to match the measured attenuating properties of lung tissue. The extra thickness approximates the contribution of lung structures that were not explicitly modeled (lymphatics and neural tissues). For completeness, future work could include lower density tissues (thinner walls) to examine the effects of alveolar tissues alone on dose accuracy. However, based on the trend of decreasing percent difference between MC-M and MC-CT dose distributions as a function of decreasing density (essentially wall thickness) in Table 6.1, one would suppose that the mean percent difference would decrease for lower densities. For the TISSUE model, it is concluded that one need not resolve the connective tissue structures of the lung to obtain accurate dose distribution calculations.

For the BRANCH model, CT representations of the branching structures did not yield accurate dose calculations (up to 14% overestimation in dose). The exclusion of branching structures had a substantial perturbing effect on the resulting dose distributions. However, the perturbation was localized around the offending branching structures. An examination of the mean difference in dose showed that the MC-M and MC-CT distributions, as a whole, agreed to within 1%. The perturbation in dose is likely the result of electronic disequilibrium conditions around the branching structures. The branching geometries introduced interfaces of contrasting atomic compositions and densities (i.e air-tissue, tissue-lung). These localized regions of high-low density produce a disequilibrium in the net electron fluence. In the CT representation, these regions are assigned a single atomic composition and mean density. The mean density in many cases is high enough to maintain electronic equilibrium conditions. This ultimately perturbs the dose calculation. It is concluded that current treatments based on CT datasets result in localized perturbations in dose due to the exclusion of branching structures below the CT resolution.

The obvious solution to the inaccuracies in the CT dose distributions is to increase the CT resolution. A higher CT resolution will decrease the total volume of voxels that contain

heterogeneities. From the TISSUE results, one might assume that there is a size scale at which structure below the CT/dose resolution can be omitted. However, one must realize that the tissue structures were small relative to the voxel size and were uniformly distributed within the voxel. This produces a condition where the voxel attenuation is nearly the same from all directions. The electron range is likely the same in all directions as well. In essence, the geometry of the heterogeneous tissue structures produces homogeneous like energy deposition and transport. In contrast, the voxels of the BRANCH model do not have heterogeneities uniformly distributed. As a result, attenuation and energy spread are direction dependent. There is no CT resolution at which this is not true. A decrease in CT/dose voxel size will only decrease the volume over which dose inaccuracies occur. However if one calculates dose on a very fine CT/dose grid, then re-scales the resulting dose distribution to a coarser dose grid, the magnitude of the inaccurate dose relative to the total voxel dose will be decreased. This should improve dose accuracy provided that the surrounding voxels do not contain heterogeneities/inaccuracies as well. An exploration of this topic will be the goal of future work. Dose distributions will be calculated from the explicit and CT representations of the BRANCH model over a range of voxel resolutions. Each pair of BRANCH and CT dose distributions will be re-scaled to a typical clinical voxel dimension. The resolution at which the rescaled BRANCH and CT distributions agree with each other (within a desired uncertainty) will be determined. This CT/dose resolution will be required to accurately calculate dose on the dimensions of the rescaled voxel grid.

It should be noted that a true CT dataset is constructed from measurements of x-ray attenuation over multiple directions. For regions of non-uniform heterogeneity, attenuation is dependent on incident direction. As a result, the density calculated from a CT Hounsfield dataset does not reflect the true density of a voxel region. Rather, it reflects an effective density. This is a limitation of the technology. In my work, the constructed CT data sets used the true density of the voxel. Future work is needed to establish whether the effective density improves or worsens dose accuracy.

For the BRANCH model simulations, dose accuracy was found to decrease with decreasing density (increasing lung volume). The relationship between density and dose

accuracy is likely due to a decrease in electronic equilibrium as a function of decreasing density. As the lung tissue density is lowered, the density difference between the the branching structures and the surrounding lung tissue increases. This increased density difference further increases the state of electronic disequilibrium at the branch-tissue boundaries. This results in an increase in the magnitude of the dose discrepancy. Regardless, the results indicate that the most accurate dose calculations are performed for maximal exhale CT images. It should be noted, however, that the accuracy of midbreath dose calculations are not significantly worse than the maximal exhale case.

It is pointed out to the reader that the bronchial, arterial and venous branches of the BRANCH model remained the same for the three respiratory phase models. In the model, structural variation was confined to motion of the lung boundary and reflected in the lung tissue density. To improve upon the work presented here, a future BRANCH model may include the motion of the branching networks as a function of respiratory volume. Currently, there is little data on the dynamics of bronchial, arterial and venous motion. However, as 4D imaging becomes more commonplace and CT resolutions continue to improve, it may be possible to create a model from anatomic measurement.

From both the TISSUE and BRANCH results, it is clear that CCC dose distributions diverge from those of Monte Carlo for densities below 0.200 g/cm^3 (up to 15% for the smallest field and density). This observation possibly stems from a known limitation of the CCC algorithm. It is documented (Ahnesjö, 1989; Francescon et al., 2000) that the CCC algorithm is less reliable when used within regions of electronic disequilibrium. As lung tissue density is lowered, the depth beyond the buildup slab at which electronic equilibrium is re-established increases. In turn, the volume of lung tissue that is under disequilibrium conditions also increases. For this reason, the CCC algorithm may be deficient for the lower range of lung densities. Another potential deficiency in the CCC approach results from the collapsed cone approximation. In the collapsed cone approximation, dose within a spatial cone is collapsed onto a single axis. The further away from the cone vertex, the larger the volume that is collapsed onto the axis. This results in a decrease in spatial accuracy with increased electron range. To test the hypothesis that the collapsed cone approximation is the source of the observed dose discrepancy, an examina-

tion of solid angle size on dose accuracy is needed. Another potential explanation for the observed dose discrepancy is the method of kernel scaling used in the CCC approach. To simplify the calculation, kernels are calculated for solid water and density scaled to match the density of the transport material. There may be a deficiency in the scaling method that becomes apparent with low densities. To test whether this is true, it would be instructive to calculate a kernel in 0.125 g/cm^3 water and compare it to the scaled kernel.

There is one recent article that address the accuracy of the Pinnacle^3 CCC algorithm over a range of lung densities. The article, published by Fogliata et al. (Fogliata et al., 2008), examines the accuracy of the Pinnacle^3 CCC algorithm at two densities (0.27 and 0.16 g/cm^3). In their work, the CCC algorithm is benchmarked against the Voxel Monte Carlo (VMC++) code (Kawrakow & Fippel, 2000). They show that the CCC dose distributions are 6-8% different from the VMC++ distributions at full inhalation breath hold (FIBH). Compared to the current work, the benchmarking of their Monte Carlo code was less rigorous. Specifically, the VMC++ code was benchmarked at one field size and depth (10x10 cm^2 at 10 cm depth). This field size was not indicative of the field used in their study which was a multileaf collimator shaped to the contour of a tumour. Further, their work was a planning study for breast treatments. The results of a planning study can be dependent on the treatment setup (specifically beam orientation and shape). Although the results are insightful, it is more useful to benchmark the CCC algorithm in very simple and controlled conditions (fixed SSD, regular field size, single beam). Unlike the work of Fogliata et al., my work shows the relationship between CCC accuracy and field size and density.

For the 1x1 cm^2 field, disagreement between CCC and MC dose distributions was substantial. Recent film measurements at the Saskatoon Cancer Center suggest that the Monte Carlo beam model produces accurate dose profiles for fields down to 0.5 x 0.5 cm^2. Most authors benchmark their models for field sizes 10x10 cm^2 and larger. My work was more rigorous as I benchmarked my model down to a field size of 4x4 cm^2. However, this does not guarantee that the Monte Carlo model is accurate down to a field size of 1x1 cm^2. Future work will include the formal benchmarking of the Monte Carlo beam model for small fields (1x1 cm^2 and smaller). Until this is done, it is difficult to make any definitive

statements about the 1x1 cm^2 results. However, taking the preliminary film measurements into account, one would suspect that the Pinnacle^3 calculation is the source of the larger dose discrepancy for the 1x1 cm^2 field. As discussed in the previous paragraph, the CCC algorithm is limited in regions of electronic disequilibrium. The nature of the 1x1 cm^2 field lends itself to disequilibrium conditions. Specifically, the 1x1 cm^2 field lacks a flat, low dose gradient plateau. Essentially, the 1x1 cm^2 field is all high dose gradient penumbra. At the edge of the field, disequilibrium results from the net outflow of electrons. For larger fields, the average dose accuracy is higher due to the contribution of accurate calculations in the low gradient region. As the field size is decreased, the volume of the field with a low dose gradient also decreases. For the 1x1 cm^2 field, the contribution from a low dose gradient region to average dose accuracy is small compared to the contribution from the high dose gradient penumbra. This results in a substantial decrease in dose accuracy. For small fields (1x1 cm^2 and smaller), the CCC dose calculation accuracy in regions of electronic equilibrium must be improved. Currently, a 1x1 cm^2 field is seldom used for conventional 3D-CRT treatment. However, novel therapies such as stereotactic radiation therapy may require fields this size. The CCC algorithm appears to be inadequate for these therapies.

The CCC algorithm generally underestimated dose when compared to Monte Carlo dose calculations. Clinically, this means that lung cancer patients are receiving higher doses than is being prescribed by the oncologist. Fortunately, the magnitude of the over-dosage appears to be small (less than 2%) for the highest lung density at all field sizes except the 1x1 cm^2. For lower lung densities, the discrepancy between CCC and MC dose distributions needs to be studied further.

CHAPTER 8

CONCLUSION

The goal of this thesis was to explore the effects of anatomic resolution, respiratory variation and dose calculation method on dose accuracy for the lung. To achieve this goal, two geometric models of the lung anatomy were created. The first model, called TISSUE, represented the alveolar and connective tissues of the lung. The second model, called BRANCH represented the bronchial, arterial and venous branching networks. Both models were varied to represent different phases of the respiration cycle from maximum exhale to maximum inhale. These models were written into a Monte Carlo code and benchmarked to verify that both proper particle transport and dose scoring occurred. To create a clinically realistic radiation source, the Varian iX linac, was modeled and benchmarked against water phantom measurements.

The effects of dose resolution on dose accuracy was explored by comparing dose distributions derived from an explicit model of the lung anatomy to dose distributions derived from a CT representation of the same anatomy. It was shown that the exclusion of connective tissue structures of the TISSUE model did not significantly effect the accuracy of dose calculations. However, it was also concluded that the exclusion of the BRANCH model branching structures created significant localized perturbations in dose accuracy. It was shown that the magnitude of the perturbation was dependent on voxel size. To ensure accurate dose distribution calculations, it is necessary to improve the CT representation of the lung anatomy for dose calculations. This may be done by increasing the resolution of the dose calculation/CT grid and de-resolving the results or potentially by applying a correction factor to voxel density which accounts for missing anatomic detail.

The effects of respiratory variation was examined by comparing dose distributions from explicit and CT representations of the lung models at three phases of respiration :

maximum exhale, midbreath and maximum inhale. It was concluded that, the variation in the alveolar/connective tissues as a function of respiratory phase did not have a significant effect on dose accuracy. It was also concluded that respiratory variation in density around the branching structures of the lung had a small effect on dose accuracy. Specifically, as lung density decreased (increasing respiratory volume), dose accuracy also decreased. However, the decrease in accuracy was small. Ultimately, the effects of respiratory variation on dose accuracy is small compared to the effects of dose resolution.

The effects of dose calculation method on dose accuracy was examined by comparing dose distributions of the Pinnacle^3 CCC algorithm to Monte Carlo. Comparisons were performed using the CT representations of both the TISSUE and BRANCH models at the three phases of respiration discussed in the previous paragraph. It was concluded that, for both the TISSUE and BRANCH model comparisons, the dose calculation accuracy of the CCC algorithm decreased with decreasing density. Further, the Pinnacle^3 CCC calculation does not produce accurate dose distributions at full inhalation lung density. This observation held true for both the TISSUE and BRANCH model comparisons. The dose inaccuracy of the CCC algorithm exceeded the 5-10% range beyond which positive patient outcome is decreased. Although the Pinnacle^3 algorithm did not produce accurate results at low lung densities, it is yet unclear whether the source of the inaccuracy is due to a state of increased electronic equilibrium which limits the applicability of the CCC approach, the method of kernel scaling or small differences between the MC and CCC source models. Further work is needed to explore the source of the Pinnacle^3 dose discrepancy at low densites and to resolve the issue.

APPENDIX A

DISTANCE TO INTERCEPT FOR POLYNOMIAL SURFACES

A.1 Introduction

To accurately calculate the distance-to-intercept to a surface along a particle trajectory, one needs a mathematical representation of the surface that will efficiently yield an analytical solution. Polynomial surfaces meet this criteria. The procedure for determining the DTI to a polynomial surface is described as follows:

1. Start with a particle trajectory which is defined as:

$$\vec{x} = \vec{p} + s\hat{u} \tag{A.1}$$

   where $\vec{p} = \{p_1, p_2, p_3\}$ is the starting position of the particle, $\vec{x} = \{x_1, x_2, x_3\}$ is the final position after transport, $\hat{u} = \{u_1, u_2, u_3\}$ is the unit direction vector and s is the distance to intercept. Each component of the vector may then be written as:

$$\begin{aligned} x_1 &= p_1 + su_1 \\ x_2 &= p_2 + su_2 \\ x_3 &= p_3 + su_3 \end{aligned} \tag{A.2}$$

2. Substitute Eq.(A.2) into the surface equation and solve for s.

3. Identify any solution that is both real and positive.

4. If more than one physical solution exists, return the smallest value, which corresponds to the nearest surface hit.

The exact solution to this problem can range from very simple to impossible depending on the mathematical form of the polynomial. The following sections outline the specific solution of the intercept problem for the various polynomial surfaces used in this thesis.

A.1.1 Planar Surfaces

A planar surface is represented by the equation:

$$\sum_{i=1}^{3} n_i \left(x_i - P_i^P \right) = 0 \tag{A.3}$$

where $\vec{x} = \{x_1, x_2, x_3\}$ is a point in three dimensional cartesian space, $\vec{P}^P = \{P_1^P, P_2^P, P_3^P\}$ is a point on the planar surface, and $\hat{n} = \{n_1, n_2, n_3\}$ is the unit vector normal to the planar surface. By substituting the components of equation (A.2) into (A.3), a solution for intercept distance, s, is found:

$$s = -\frac{\hat{n} \cdot \left(\vec{p} - \vec{P}^P \right)}{\hat{n} \cdot \hat{u}} \tag{A.4}$$

To make use of the above solution, the code requires prior knowledge of the particle position relative to the planar surface. The convention is to identify a particle as "above" the plane if it is on the side that the unit vector $\hat{n}$, is pointing into. Otherwise, the particle is designated "below". For the solution to have any physical meaning, it must be positive or the particle will be transported backwards. Fig.A.1 outlines the procedure for interpreting the physical validity of Eq.(A.4).

A.1.2 Quadric Surfaces

A general quadric surface may be written as:

$$\sum_{i=0}^{3} \sum_{j=0}^{3} n_{ij} (x_i - \delta x_i)(x_j - \delta x_j) = 0 \tag{A.5}$$

By substituting Eq.(A.2) into Eq.(A.5) and grouping powers of s, one finds a simple quadratic equation of the form:

$$A_q s^2 + 2B_q s + C_q = 0 \tag{A.6}$$

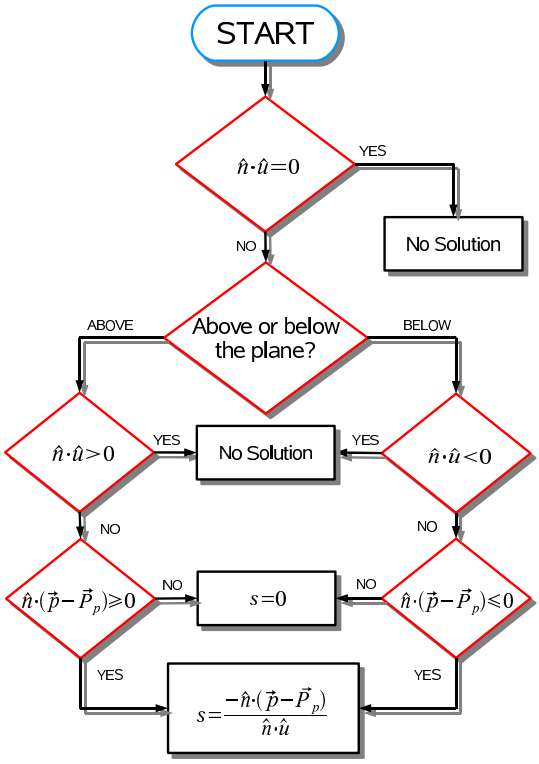

Figure A.1: The distance to intercept algorithm for a planar surface.

where A_q, B_q, and C_q are constants. The solution to Eq.(A.6) is the well known quadratic formula:

$$s = \left(-B_q \pm \sqrt{B_q^2 - 4A_qC_q}\right)/2A_q \tag{A.7}$$

The real, non-negative solution (if any) to this equation is the trajectory intercept distance to the quadric surface. As it was in the planar case, one requires prior knowledge as to whether a particle is above or below (or equivalently, outside or inside) the quadric surface. For closed surfaces like a sphere, the distinction between inside and outside is quite clear. For other surfaces, like a cone or paraboloid, the distinction becomes a little more difficult. As a general rule, values of $\vec{x}$ that leave the left hand side of equation (A.5) less than zero are inside the surface while values that generate a greater than zero solution are outside.

Fig.A.2 outlines the quadric criteria for a physical solution of s.

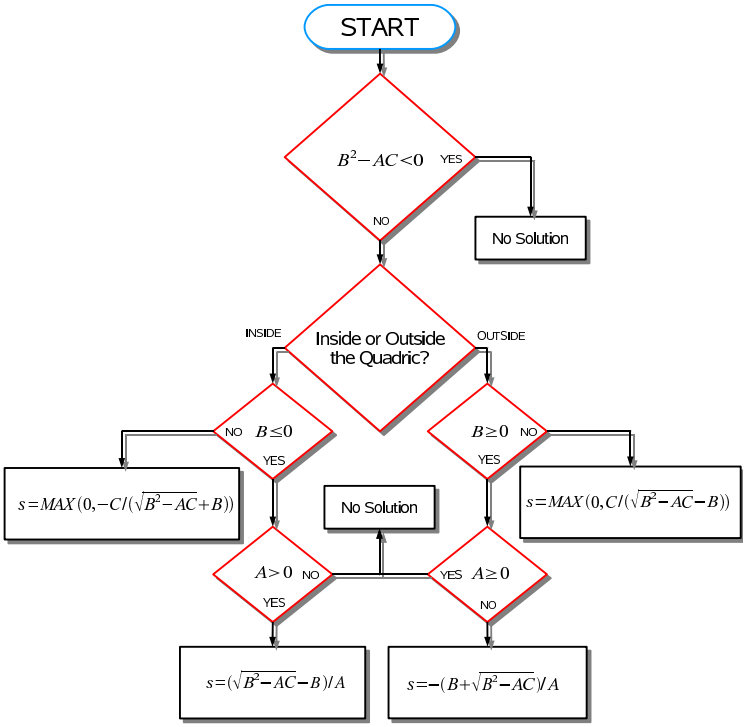

Figure A.2: The distance to intercept algorithm for a quadric surface.

A.1.2.1 Sphere

The equation of a sphere is :

$$\left(\vec{x}-\vec{P}_s\right)^2-R_s^2=0 \tag{A.8}$$

where $\vec{P}_s$ is the cartesian coordinates of the center of the sphere and R_s is the sphere radius. Using the method outlined in section A.1.2, Eq.(A.1) is inserted into Eq.(A.8) to give a quadratic of the form seen in Eq.(A.6). The quadratic constants are of the following form:

$$\begin{aligned} A_{SPH} &= 1.0 \\ B_{SPH} &= \left(\vec{p}-\vec{P}_s\right)\cdot\vec{u} \\ C_{SPH} &= \left(\vec{p}-\vec{P}_s\right)^2-R_s^2 \end{aligned} \tag{A.9}$$

A.1.2.2 Cylinder

The general equation of a cylinder is :

$$\left(\vec{x}-\vec{P}_c\right)-\left(\left(\vec{x}-\vec{P}_c\right)\cdot\vec{U}_c\right)^2=0 \tag{A.10}$$

where $\vec{P}_c$ is a point on the cylinder axis and $\vec{U}_c$ is a unit vector that defines the axis itself. This quadric surface also reduces to a quadratic equation with constants:

$$\begin{aligned} A_{CYL} &= 1-\left(\vec{u}\cdot\vec{U}_c\right)^2 \\ B_{CYL} &= \vec{u}\cdot\left(\vec{p}-\vec{P}_c\right)-\left(\vec{u}\cdot\vec{U}_c\right)\left(\left(\vec{p}-\vec{P}_c\right)\cdot\vec{U}_c\right) \\ C_{CYL} &= \left(\vec{p}-\vec{P}_c\right)^2-\left(\left(\vec{p}-\vec{P}_c\right)\cdot\vec{U}_c\right)^2-R_c^2 \end{aligned} \tag{A.11}$$

APPENDIX B

POLYNOMIAL EQUATIONS OF THE BRANCH MODEL BOUNDARY

Table B.1: Surface equations defining the lung boundary of the BRANCH model.

Feature	Surface Equation
Ribcage	$\frac{2}{1000}(z-\delta z_Q)^4 + 25(x-\delta x_Q)^2 + Q_1(y-\delta y_Q)^2 + 6.5(z-\delta z_Q)^2 + 0.3(y-\delta y_Q)^2(z-\delta z_Q)^2 - 8(y-\delta y_Q)(z-\delta z_Q) + Q_2 = 0$
Diaphragm	$D_1(y-\delta y_D)^2 - D_2(y-\delta y_D) - 11(x-1)^2 - 134(x-1) - 3.97(x-1)(y-\delta y_D) - 128.17(z-\delta z_D) - 3691.8 = 0$
Heart	$9(x-4.8)^2 + 20(y-2)^2 + 18(z+20)^2 - 4(x-4.8)(y-2) - 5(y-2)(z+20) - 600 = 0$
Spine	$80x^2(y-12.5)^2 + 4(y-12.5)^4 - 0.5(y-12.5)^2(z+26)^2 - 60(y-12.5)^2 - 1000 = 0$

Continued on next page

Table B.1 – continued from previous page

Feature	**Surface Equation**
Mediastinum	$0.3 + (V - 100)/77 = 0$
Substitutions	**Value**
x , y , z	$(x - 0.5)$, $(y + 4.5)$, $(z - 7.7)$
Q_1 , Q_2	$(22.727 + 0.1305 \cdot V)$, $(-1283.2 - 19 \cdot V)$
δx_Q , δy_Q , δz_Q	$(-2.5965 - 0.0052638 \cdot V)$, $(4.3954 - 0.018567 \cdot V)$, $(-25.45 - 0.045494 \cdot V)$
D_1 , D_2	$(-14.381 + 0.052147 \cdot V)$, $(-13.593 + 0.13171 \cdot V)$
δy_D , δz_D	$(4.2877 - 0.061582 \cdot V)$, $(2.3 - 0.1245 \cdot V)$

APPENDIX C

THE BRANCH ALGORITHMS

C.1 The BOUNDARY algorithm

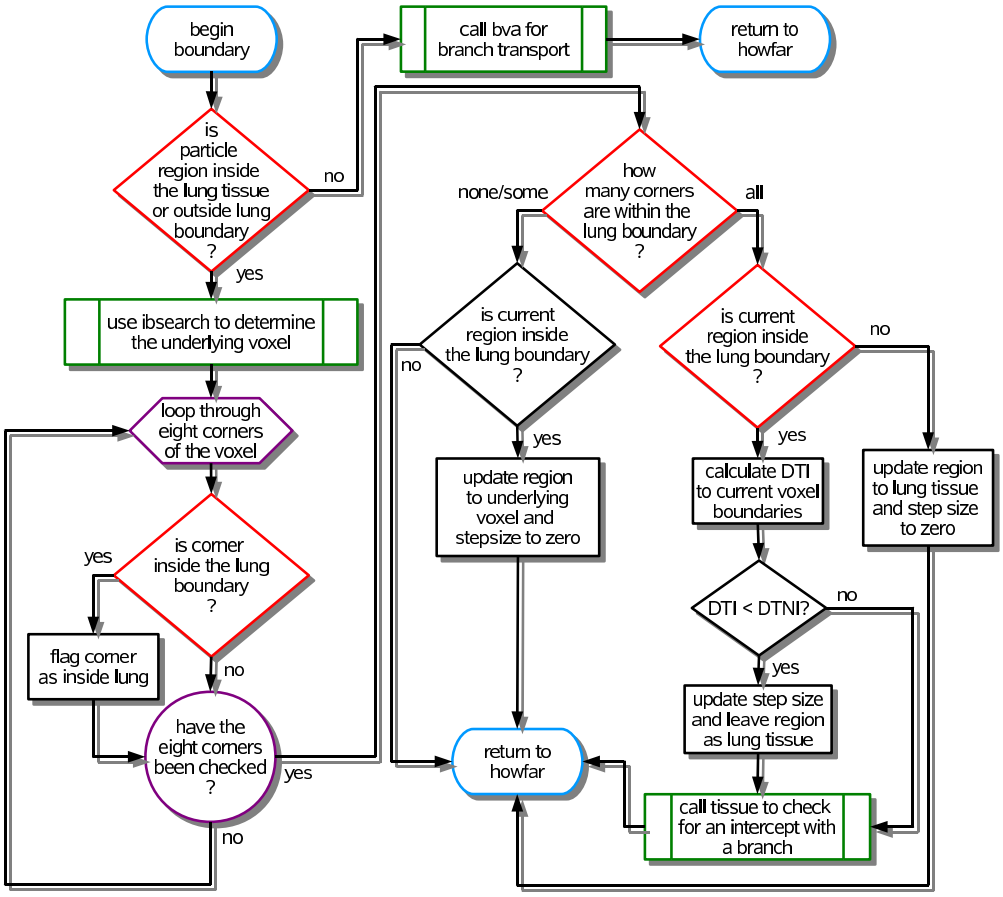

Figure C.1: The BOUNDARY algorithm of the BRANCH model.

C.2 The TISSUE algorithm

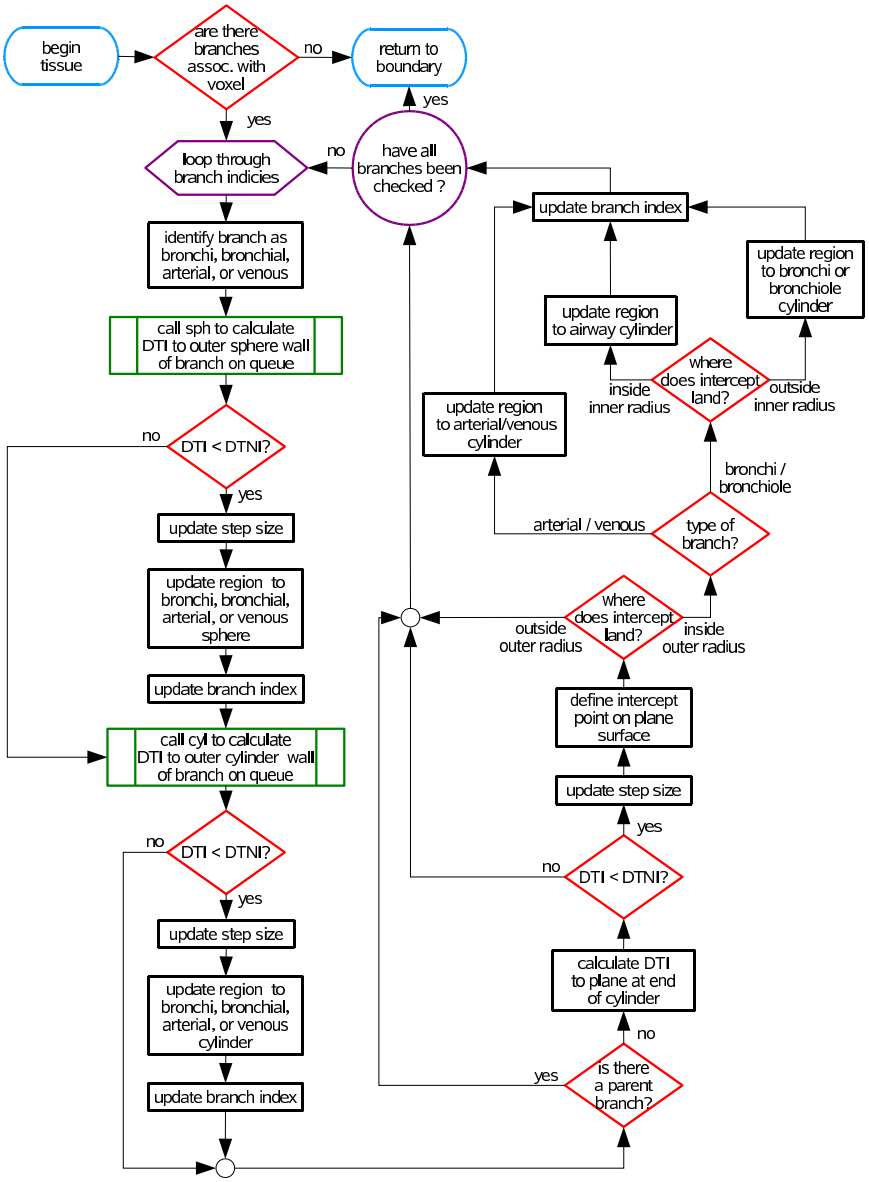

Figure C.2: The TISSUE algorithm of the BRANCH model.

C.3 The BVA algorithm

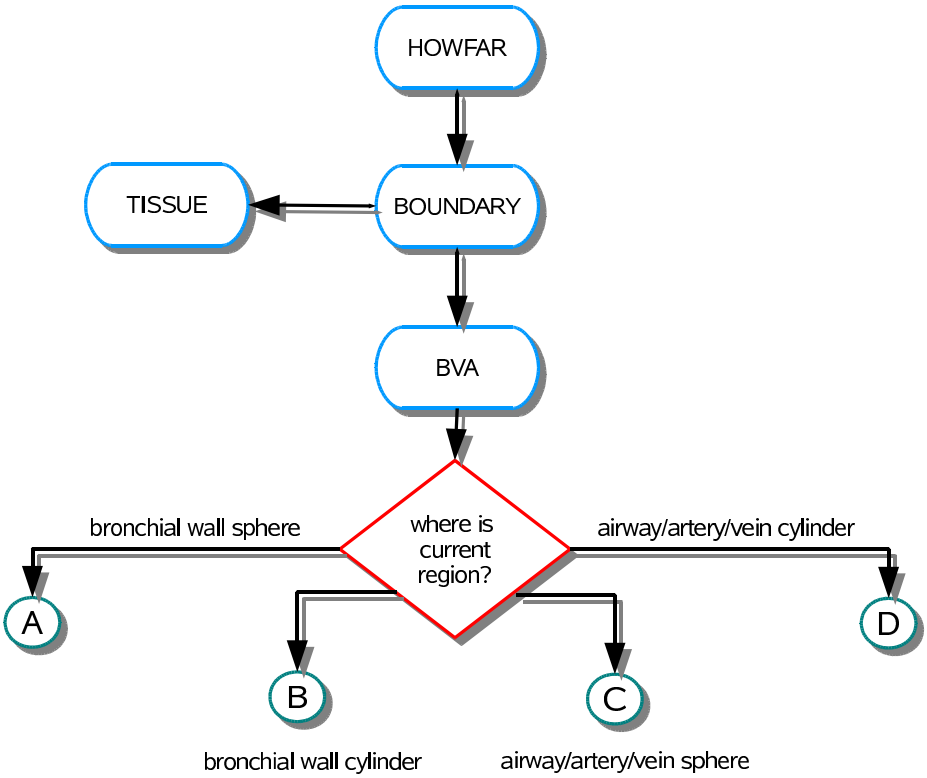

Figure C.3: The BVA algorithm of the BRANCH model.

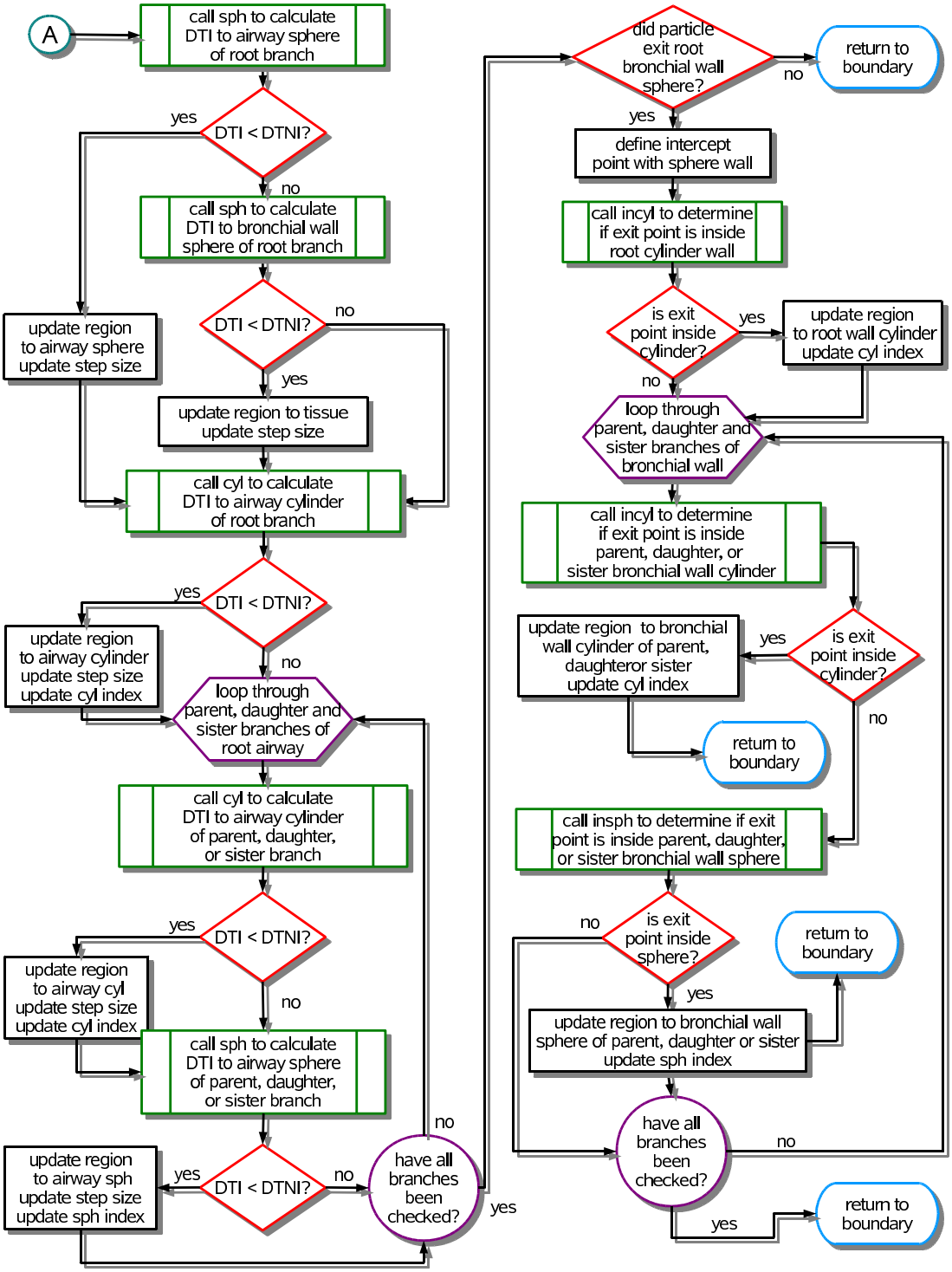

Figure C.4: The bronchial wall sphere algorithm of BVA.

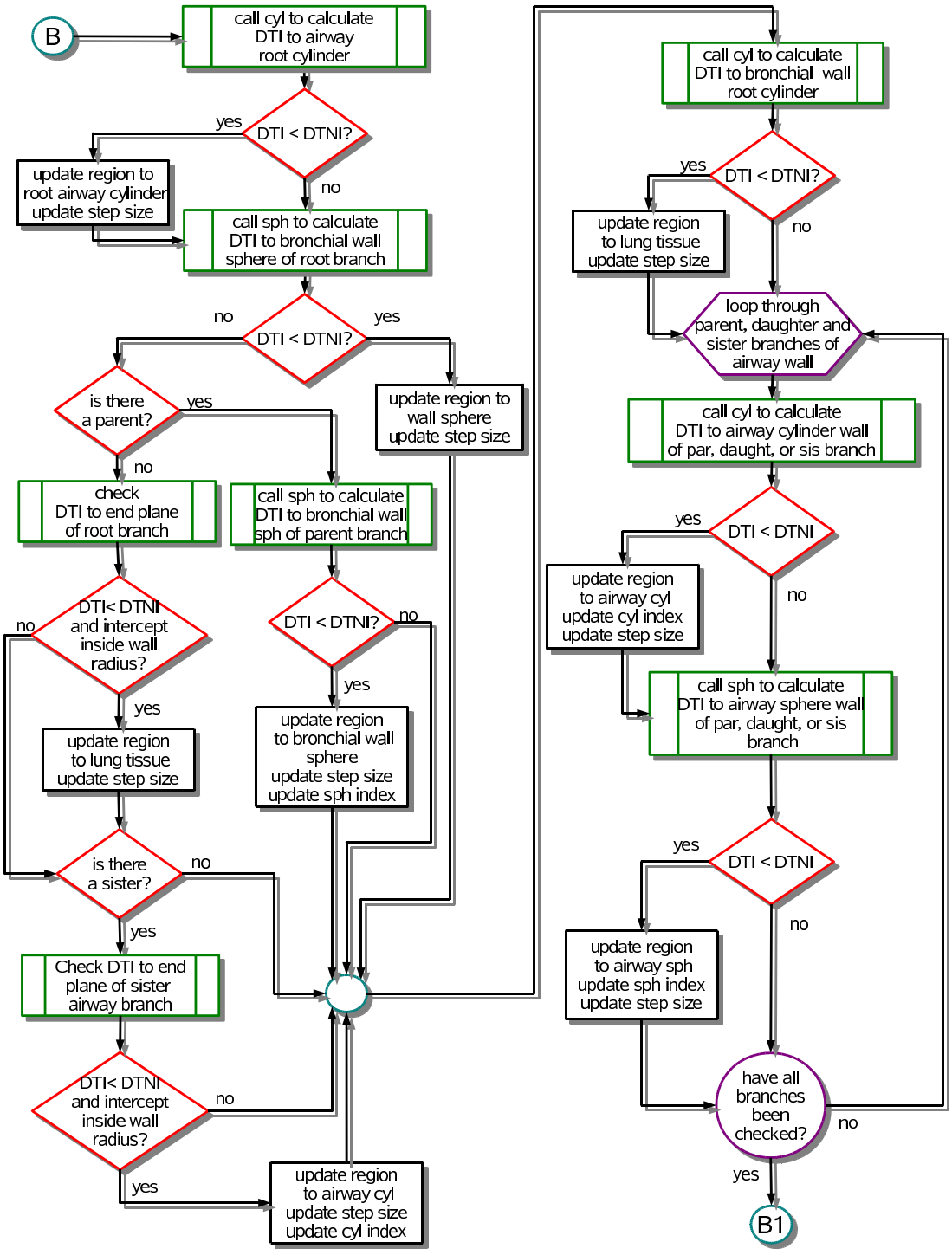

Figure C.5: The bronchial wall cylinder algorithm of BVA.

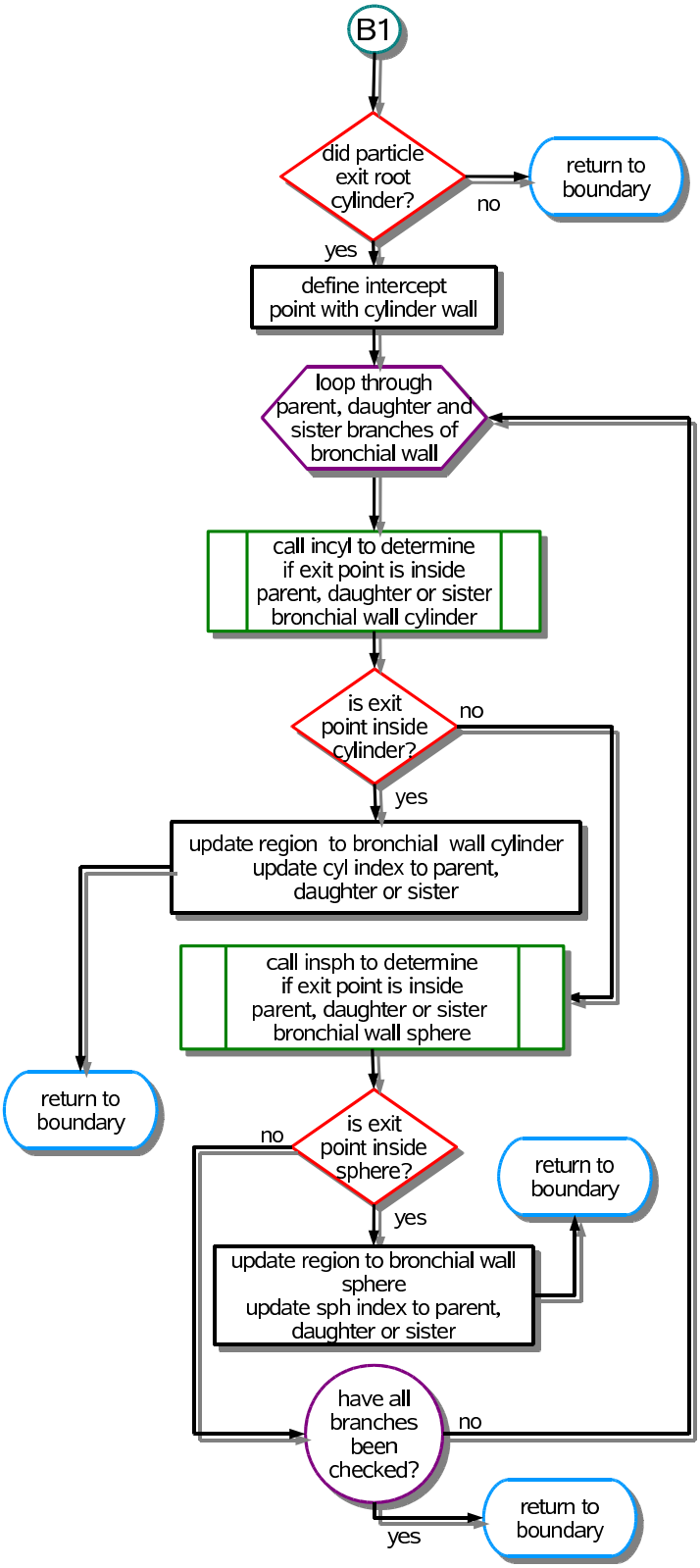

Figure C.6: The bronchial wall cylinder algorithm of BVA cont'd.

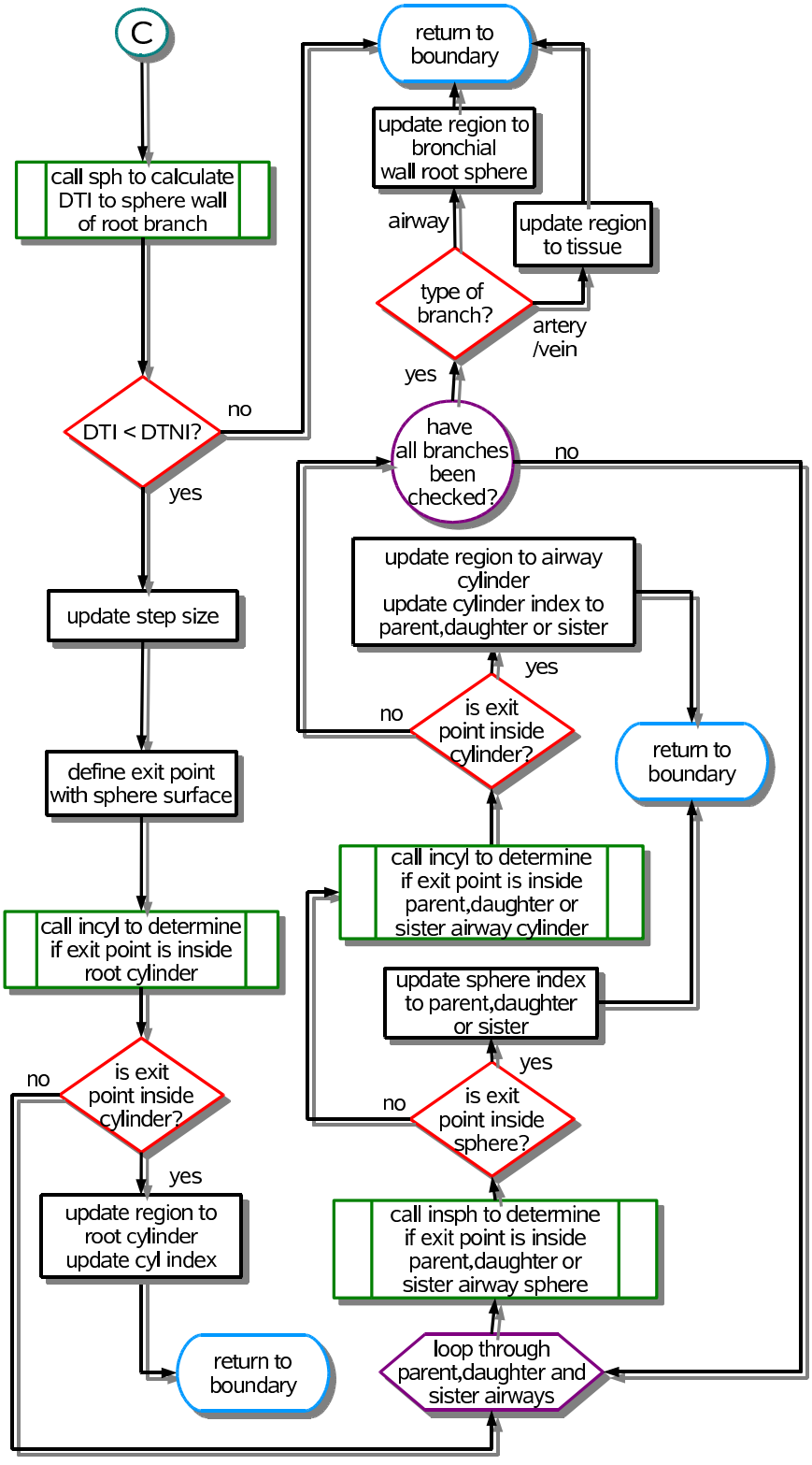

Figure C.7: The airway/artery/vein sphere algorithm of BVA.

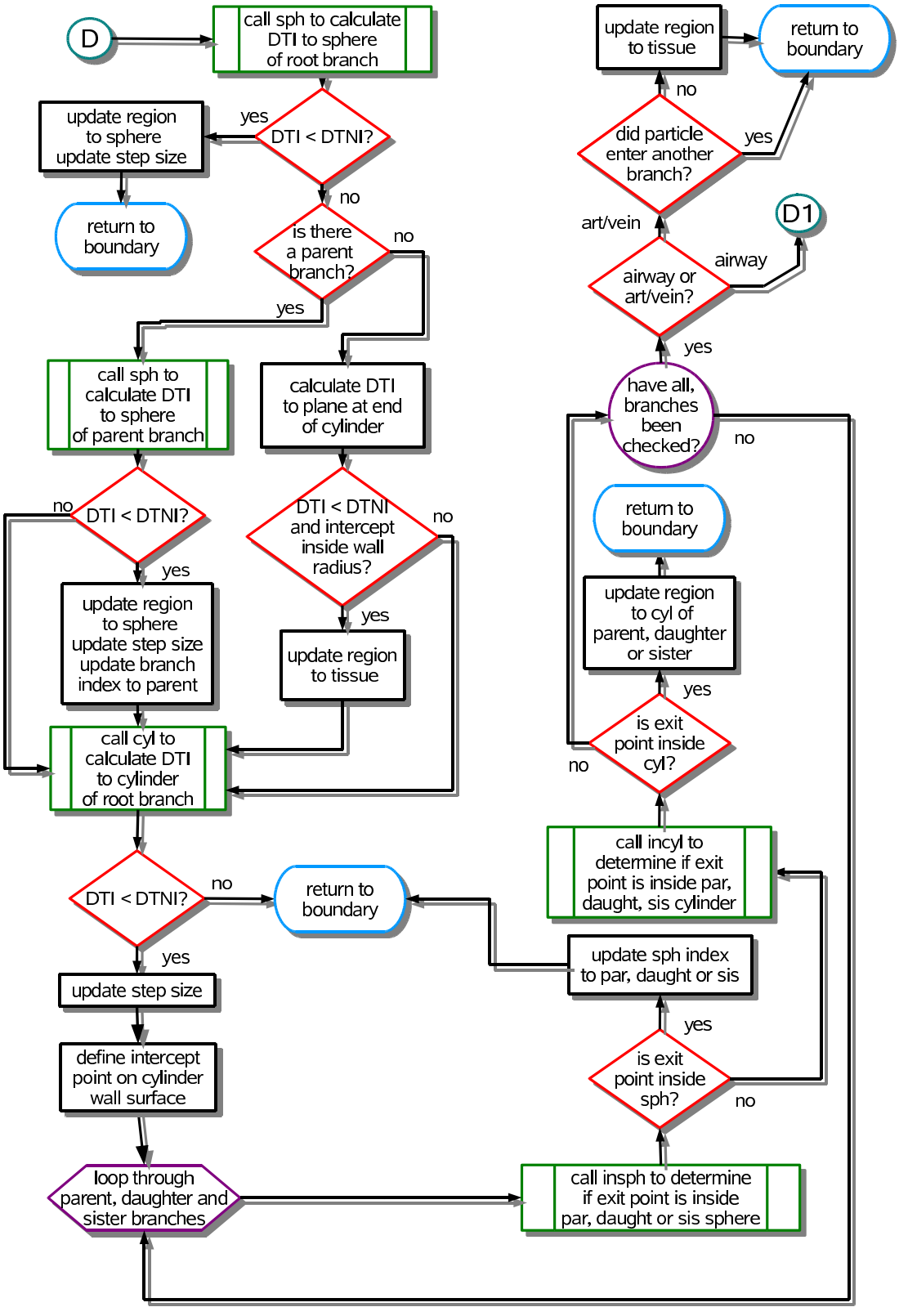

Figure C.8: The airway/artery/vein cylinder algorithm of BVA.

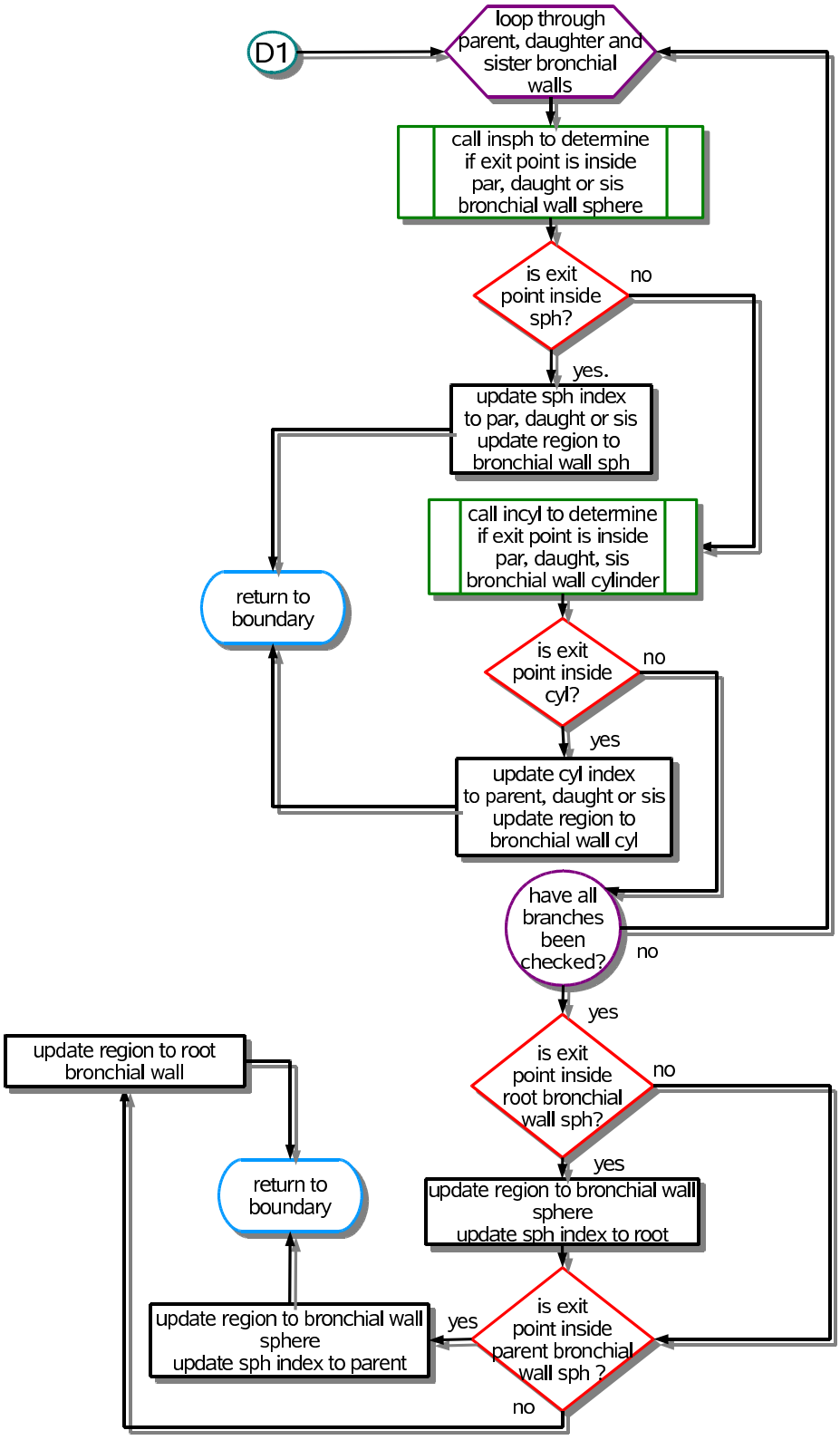

Figure C.9: The airway/artery/vein cylinder algorithm of BVA cont'd.

BIBLIOGRAPHY

Ahnesjö, A. (1989). Collapsed cone convolution of radiant energy for photon dose calculation in heterogeneous media. *Med. Phys.*, *16*(4), 577-592.

Aljarrah, K., Sharp, G. C., Neicu, T., & Jiang, S. B. (2006, April). Determination of the initial beam parameters in Monte Carlo linac simulation. *Med. Phys.*, *33*(4), 850-858.

American Thoracic Society. (1991). Lung function testing: selection of reference values and interpretive strategies. *Am. Rev. Respir. Dis.*, *144*, 1202-1218.

Armstrong, J. G. (1998). Target volume definition for three-dimensional conformal therapy of lung cancer. *Br. J. Radiol.*, *71*, 587-594.

Arnfield, M. R., Siantar, C. H., Siebers, J., & Garmon, P. (2000). The impact of electron transport on the accuracy of computed dose. *Med. Phys.*, *27*(6), 1266-1274.

Aste, T., & Weaire, D. (2000). *The pursuit of perfect packing*. Institute of Physics Publishing.

Babcock, K., Cranmer-Sargison, G., & Sidhu, N. (2008). Increasing the speed of DOSXYZnrc Monte Carlo simulations through the introduction of nonvoxlated geometries. *Med. Phys.*, *35*(2).

Babcock, K., & Sidhu, N. (2010a). The effects of dose calculation resolution on dose accuracy for radiation therapy treatments of the lung. part I: A Monte Carlo model of the lung. *Med. Phys.*, *37*(2).

Babcock, K., & Sidhu, N. (2010b). The effects of dose calculation resolution on dose accuracy for radiation therapy treatments of the lung. part II: A comparison of dose distributions from an explicit lung model to dose distributions derived from a CT representation. *Med. Phys.*, *37*(2).

Bedford, J. L., Childs, P. J., Nordmark Hansen, V., Mosleh-Shirazi, M. A., Verhaegen, F., & Warrington, A. P. (2003). Commissioning and quality assurance of the Pinnacle^3 radiotherapy treatment planning system for external beam photons. *Br. J. Radiol.*, *76*, 163-176.

Berger, M. J. (1963). Methods in Computational Physics. : Monte Carlo calculations of the penetration and diffusion of fast charged particles. In B. Alder, S. Fernbach, & M. Rotenberg (Eds.), (Vol. 1, p. 135-215). Academic, New York.

Bielajew, A. (1995). PIRS-0341 HOWFAR and HOWNEAR : Geometry modeling for Monte Carlo transport [Computer software manual].

Boyer, A. L., & Schultheiss, T. (1988). Effects of dosimetric and clinical uncertainty on complication free local tumor control. *Radiother. Oncol.*, *11*(1), 65-71.

Butson, M. J. (2000). Verification of lung dose in an anthropomorphic phantom calculated by the collapsed cone convolution method. *Phys. Med. Biol.*, *45*, N143.

Carlsson, A., & Ahnesjö, A. (2000). The collapsed cone superposition algorithm applied to scatter dose calculations in brachytherapy. *Med. Phys.*, *27*(10), 2320-2332.

Chow, J. C. L. (2003). Comparison of dose calculation algorithms with monte carlo methods for photon arcs. *Med. Phys.*, *30*(10), 2686-2694.

Cranmer-Sargison, G., Beckham, W., & Popescu, I. (2004). Modeling an extreme water lung interface using a single pencil beam algorithm and the Monte Carlo method. *Phys. Med. Biol.*, *49*(8), 1557-1567.

Crystal, R. G., & West, J. B. (Eds.). (1991). *The lung, scientific foundations*. Raven Press.

Deng, J., Jiang, S. B., Kapur, A., Li, J., Pawlicki, T., & Ma, C. (2000). Photon beam characterization and modeling for Monte Carlo treatment planning. *Phys. Med. Biol.*, *45*, 411-427.

De Smedt, B., Reynaert, N., Nerve, W. de, & Thierens, H. (2004). DOSSCORE: an accelerated DOSXYZnrc code with an efficient stepping algorithm and scoring grid. *Phys. Med. Biol.*, *49*, 4623-4635.

Ding, G. X. (2002). Energy spectra, angular spread, fluence profiles and dose distributions of 6 and 18 mv photon beams: results of Monte Carlo simulations for a Varian 2100EX accelerator. *Phys. Med. Biol.*, *47*, 1025-1046.

Dutreix, A. (1984). When and how we can improve precision in radiotherapy. *Radiother. Oncol.*, *2*(4), 275-292.

Ekstrand, K. E., & Barnes, W. H. (1990). Pitfalls in the use of high energy x rays to treat tumors in the lung. *Int. J. Rad. Oncol. Biol. Phys.*, *18*(1), 249-252.

El-Khatib, E., & Battista, J. J. (1986). Accuracy of lung dose calculations for large-field irradiation with 6-mv xrays. *Med. Phys.*, *13*(1), 111-116.

Fogliata, A., Nicolini, G., Vanetti, E., Clivio, A., Winkler, P., & Cozzi, L. (2008). The impact of photon dose calculation algorithms on expected dose distributions in lungs under different respiratory phases. *Phys. Med. Biol.*, *53*, 2375-2390.

Fraas, B., Doppke, K., Hunt, M., Kutcher, G., Starkschall, G., Stern, R., et al. (1998). American association of physicists in medicine radiation therapy committee task group 53: Quality assurance for clinical radiotherapy treatment planning. *Med. Phys.*, *25*(10), 1773-1829.

Francescon, P., Cavedon, C., Reccanello, S., & Cora, S. (2000). Photon dose calculation of a three-dimensional treatment planning system compared to the Monte Carlo code BEAM. *Med. Phys.*, *27*(10), 1579-1587.

Gauthier, A. P. (1994). three-dimensional reconstruction of the in vivo human diaphragm shape at different lung volumes. *J. Appl. Physiol.*, *76*(2), 495-506.

Giraud, P., De Rycke, Y., Dubray, B., Helfre, S., Voican, D., Guo, L., et al. (2001). Conformal radiotherapy (CRT) planning for lung cancer: analysis of intrathoracic organ motion during extreme phases of breathing. *Int. J. Rad. Oncol. Biol. Phys.*, *51*(4), 1081-1092.

Hansen, J. E., & Ampaya, E. (1975). Human air space shapes, sizes,areas and volumes. *J. App. Physiol.*, *38*(6), 990-995.

Hasenbalg, F., Neuenschwander, H., Mini, R., & Born, E. J. (2007). Collapsed cone convolution and analytical anisotropic algorithm calculations compared to VMC++ Monte Carlo simulations in clinical cases. *Phys. Med. Biol.*, *52*, 3679-3691.

Haung, W., Yen, R. T., McLaurine, M., & Bledsoe, G. (1996). Morphometry of the human pulmonary vasculature. *J. Appl. Physiol.*, *81*, 2123-2133.

Horsfield, K. (1978). Morphometry of the small pulmonary arteries in man. *Circ. Res.*,

42, 593-597.

Horsfield, K., & Cumming, G. (1967). Angles of branching and diameters of branches in the human bronchial tree. *Bull. Math. Biophys.*, *29*, 245-259.

Horsfield, K., Dart, G., Olson, D. E., Filley, G. F., & Cumming, G. (1971). Models of the human bronchial tree. *J. Appl. Physiol.*, *31*, 207-217.

Horsfield, K., Fernando, R. G., & Cumming, G. (1976). Diameter, length and branching ratios in the bronchial tree. *Resp. Physiol.*, *26*, 351-356.

Horsfield, K., & Gordon, W. I. (1981). Morphometry of pulmonary veins in man. *Lung*, *159*, 211-218.

Horsfield, K., & Thurlbeck, A. (1981a). Relationship between diameter and flow in branches of the bronchial tree. *Bull. Math. Biol.*, *43*, 681-691.

Horsfield, K., & Thurlbeck, A. (1981b). Volume of the conducting airways calculated from morphometric parameters. *Bull. Math. Biophys.*, *43*, 101-109.

Hunt, M., Desobry, G., Fowble, B., & Coia, L. (1997). Effect of low-density lateral interfaces on soft-tissue doses. *Int. J. Rad. Oncol. Biol. Phys.*, *37*(2), 475-482.

ICRU Report 24 : Determination of absorbed dose in a patient irradiated by beams of x or gamma rays in radiotherapy procedures. (1976). International Commission on Radiation Units and Measurements.

ICRU Report 44 : Tissue substitutes in radiation dosimetry and measurement. (1989). International Commission on Radiation Units and Measurements.

Kamiya, A., Togawa, T., & Yamamoto, A. (1974). Theoretical relationship between the optimal models of the vascular tree. *Bull. Math. Biol.*, *36*, 311-323.

Kawrakow, I. (2000a). Accurate condensed history Monte Carlo simulation of electron transport I. EGSnrc, the new EGS4 version. *Med. Phys.*, *27*(3), 485-498.

Kawrakow, I. (2000b). Accurate condensed history Monte Carlo simulation of electron transport II. Application to ion chamber response simulations. *Med. Phys.*, *27*(3), 499-513.

Kawrakow, I., & Fippel, M. (2000). VMC++ a MC algorithm optimized for electron and photon beam dose calculations. In W. Schlegel & T. Bortfeld (Eds.), *The use of computers in radiotherapy, XIIIth International Conference* (p. 126 -128). Springer-Verlag, Heidelberg.

Kawrakow, I., Mainegra-Hing, E., Rogers, D. W. O., Tessier, F., & Walters, B. R. B. (2009). Report PIRS-701 : The egsnrc code system: Monte Carlo simulation of electron and photon transport [Computer software manual]. NRC, Ottawa Ont, K1A OR6.

Kawrakow, I., & Rogers, D. W. O. (2000, October). The EGSnrc system, a status report : Advanced Monte Carlo for radiation physics, particle transport simulation and applications. In *Proceedings of the Monte Carlo 2000 conference, lisbon* (p. 135-140).

Keall, P. J., Siebers, J. V., Libby, B., & Mohan, R. (2003, April). Determining the incident electron fluence for Monte Carlo-based photon treatment planning using a standard measured data set. *Med. Phys.*, *30*(4), 574-582.

Kitaoka, H., Takaki, R., & Suki, B. (1999). A three-dimensional model of the human airway tree. *J. Appl. Physiol.*, *87*(6), 2207-2217.

Kitaoka, H., Tamura, S., & Takaki, R. (2002). Human air space shapes, sizes,areas and volumes. *J. App. Physiol.*, *88*, 2260-2268.

Krause, E., Bandt, C., Schulz, A., & Shulz, H. (1995, February). Fractal exponents for the upper airways of mammalian lungs. *The Statistical Software Newsletter*, 583-590.

Loevinger, R., & Loftus, T. P. (1977). Ionizing radiation metrology, international course. In E. Casnati (Ed.), (p. 459-473). Bologna, Editrice Compositore.

Low, D. A., Harms, W. B., Mutic, S., & Purdy, J. A. (1998). A technique for quantitative evaluation of dose distrubutions. *Med. Phys.*, *25*(5), 656-661.

Mackie, T. R., Bielajew, A. F., Rogers, D. W. O., & Battista, J. J. (1988). Generation of photon energy deposition kernels using the EGS Monte Carlo code. *Phys. Med. Biol.*, *33*(1), 1-20.

Mackie, T. R., El-Khatib, E., Battista, J. J., Scrimger, J., Van Dyk, J., & Cunningham, J. (1985). Lung dose corrections for 6 and 15 MV xrays. *Med. Phys.*, *12*(3), 327-332.

Mathieu, R., Martin, E., Gschwind, R., Makovicka, L., Contassot-Vivier, S., & Bahi, J. (2005). Calculations of dose distributions using a neural network model. *Phys. Med. Biol.*, *50*(5), 1019-1028.

Mayer, R., Williams, A., Frankel, T., Cong, Y., Simons, S., Yang, N., et al. (1997). Two-dimensional film dosimetry application in heterogeneous materials exposed to megavoltage photon beams. *Med. Phys.*, *24*(3), 455-460.

Merryn, M. H., H. Tawhai, Hunter, P., Tschirren, J., Reinhardt, J., McLennan, G., & Hoffman, E. A. (2004). CT-based geometry analysis and finite element models of the human and ovine bronchial tree. *J. Appl. Physiol.*, *97*, 2310-2321.

Metcalfe, P., Kron, T., & Hoban, P. (1997). The physics of radiotherapy x-rays from linear accelerators. In (chap. 7). Medical Physics Publishing.

Murray, C. D. (1926). The physiological principal of minimum work. the vascular system and the cost of blood flow. *Proc. Natl. Acad. Sci. USA*, *12*, 207-214.

Papanikolaou, N., Mackie, T. R., Meger-Wells, C., & Gehring, M. (1993). Investigation of the convolution method for polyenergetic spectra. *Med. Phys.*, *20*(5), 1327-1336.

Phillips, C. G., & Kaye, S. R. (1995). Diameter-based analysis of the branching geometry of four mammalian bronchial trees. *Resp. Physiol.*, *102*, 303-316.

Pinnacle^3 physics guide : External beam and brachytherapy (P/N 9201-5067A-ENG Rev. A ed.) [Computer software manual]. (2001, May).

Rogers, D. W. O., Walters, B. R. B., & Kawrakow, I. (2009). Report PIRS-0 509(A) revK : BEAMnrc users manual [Computer software manual]. NRC, Ottawa Ont, K1A OR6.

Saithoh, H., Fujisaki, T., Saskai, R., & Kunieda, E. (2002). Dose distribution of narrow beam irradiation for small lung tumor. *Int. J. Rad. Oncol. Biol. Phys.*, *53*(5), 1380-1387.

Sauret, V., Halson, P. M., Brown, I. W., Fleming, J. S., & Bailey, A. G. (2002). Study of the three dimensional geometry of the central conducting airways in man using computed tomographic (CT) images. *J. Anat.*, *200*, 123-134.

Sheikh-Bagheri, D., & Rogers, D. W. O. (2002, March). Sensitivity of megavoltage photon beam Monte Carlo simulations to electron beam and other parameters. *Med. Phys.*, *29*(3), 379-390.

Singhal, S., Henderson, R., Horsfield, K., Harding, K., & Cumming, G. (1973). Morphometry of the human pulmonary arterial tree. *Circ. Res.*, *33*, 190-197.

Spitzer, V. M., & Whitlock, D. G. (1998). *Atlas of the visible human male*. Jones and Bartlett.

Stocks, J., & Quanjer, P. H. (1995). Reference values for residual volume, functional residual capacity and total lung capacity. *Eur. Respir. J.*, *8*, 492-506.

Textbook of respiratory medicine. (2000). In J. F. Murray & J. A. Nadel (Eds.), (3rd ed.). U.K.: W.B. Saunders.

Tzedakis, A., Damilakis, J. E., Mazonakis, M., Stratakis, J., Varveris, H., & Gourtsoyiannis, N. (2004, April). Influence of initial electron beam parameters on Monte Carlo calculated absorbed dose distributions for radiotherapy photon beams. *Med. Phys.*, *31*(4), 907-913.

Walters, B., & Kawrakow, I. (2007). A "HOWFARLESS" option to increase efficiency of homogeneous phantom calculations with DOSXYZnrc. *Med. Phys.*, *34*, 3794-3807.

Walters, B. R. B., Kawrakow, I., & Rogers, D. W. O. (2007). Report PIRS-794 revB : DOSXYZnrc users manual [Computer software manual]. NRC, Ottawa Ont, K1A OR6.

Ward, M. E., Ward, J. E., & Macklem, P. T. (1992). Analysis of human chest wall motion using a two-compartment rib cage model. *J. Appl. Physiol.*, *72*(4), 1338-1347.

Weibel, E. R. (1963). *Morphometry of the human lung*. Berlin:Springer-Verlag.

Weisstein, E. W. (2009). *"Dodecahedron." From Mathworld–a Wolfram web resource.* Available from `http://mathworld.wolfram.com/Dodecahedron.html`

Wilson, E. M. (2003). Three-dimensional conformal radiotherapy in the radical treatment of non-small cell lung cancer. *Clinical Oncology*, *15*(7), 412-419.